CHEMISTRY AND MODELING OF LOWER ATMOSPHERE OF MARS

A THESIS

Submitted for the Award of Ph.D. Degree of

PACIFIC ACADEMY OF HIGHER EDUCATION
AND RESEARCH UNIVERSITY

By

SHAH SIDDHI YOGESHKUMAR

Under the Supervision of

Prof. S. A. HAIDER **Dr. RAKSHIT AMETA**

DEPARTMENT OF CHEMISTRY
FACULTY OF SCIENCE

PACIFIC ACADEMY OF HIGHER EDUCATION AND RESEARCH UNIVERSITY
UDAIPUR

Dedicated to my

Family

DEPARTMENT OF CHEMISTRY

PAHER UNIVERSITY, UDAIPUR

Prof. S. A. HAIDER
Senior Professor

CERTIFICATE

It gives me immense pleasure in certifying that the thesis entitled **"CHEMISTRY AND MODELING OF THE LOWER ATMOSPHERE OF MARS"** submitted by **SHAH SIDDHI YOGESHKUMAR** is based on the research work carried out under my guidance. She has completed the following requirements as per Ph.D. regulations of the University.

(i) Course work as per University rules.

(ii) Residential requirements of the University.

(iii) Regularly submitted Half Yearly Progress Report.

(iv) Published/accepted minimum of two research paper in a refereed research journal.

I recommend the submission of thesis.

Date:

(Prof. S. A. HAIDER)
Ph.D Supervisor
Faculty of Science,
PAHER University
Udaipur

Senior Professor
Physical Research Laboratory
Ahmedabad

DEPARTMENT OF CHEMISTRY

PAHER UNIVERSITY, UDAIPUR

Dr. RAKSHIT AMETA
Associate Professor

CERTIFICATE

It gives me immense pleasure in certifying that the thesis entitled **"CHEMISTRY AND MODELING OF THE LOWER ATMOSPHERE OF MARS"** submitted by **SHAH SIDDHI YOGESHKUMAR** is based on the research work carried out under my guidance. She has completed the following requirements as per Ph.D. regulations of the University.

(i) Course work as per University rules.

(ii) Residential requirements of the University.

(iii) Regularly submitted Half Yearly Progress Report.

(iv) Published/accepted minimum of two research paper in a refereed research journal.

I recommend the submission of thesis.

Date:

(Dr. RAKSHIT AMETA)
Co-Supervisor

DECLARATION

I, **SHAH SIDDHI YOGESHKUMAR** D/o **Shri YOGESHKUMAR SHAH** resident of Ahmedabad, Gujarat (India) hereby declare that the research work incorporated in the present thesis entitled **" CHEMISTRY AND MODELING OF THE LOWER ATMOSPHERE OF MARS”** is my own work and is original. This work (in part or in full) has not been submitted to any University for the award of a Degree or a Diploma. I have properly acknowledged the material collected from secondary sources, wherever required. I solely own the responsibility for the originality of the entire content.

Date: **(SHAH SIDDHI YOGESHKUMAR)**
Place: Udaipur Research Scholar

COPYRIGHT

ACKNOWLEDGEMENTS

There are a number of people who deserve to be acknowledged and thanked for their help during my Ph.D. tenure. First of all, I would like to express my sincere and deepest gratitude to my supervisor, **PROF. S. A. HAIDER**, for his meticulous guidance, continued encouragement and moral support all through the pursuance of the research work. I consider myself very fortunate to be associated with **PROF. S. A. HAIDER**. His enthusiasm and integral view on research have made a deep impression on me. He has spent voluminous amount of time with me and helped me in understanding the research issues and improving my presentation skills. He has helped me set milestones and guided me to make steady progress. I have been greatly benefitted from his discussions, remarks and suggestions. His positive attitude towards solving scientific problems teaches me a lot. His supervision helped me throughout my research and writing of this thesis.

I gratefully acknowledge the support of J.C. Bose grant to carry out my thesis work.

I am very much indebted to **DR. RAKSHIT AMETA** my co-supervisor. His suggestions, valuable advices and guidance helped me in many ways.

The inspiration, support and cooperation that I have received from my friends and seniors are beyond the scope of any acknowledgement. Yet, I would like to express my heartfelt gratitude to them. I am very fortunate to have colleagues like **BHAVIN BHAI, THIRU BHAIYA, DEEPAK BHAIYA, ASHIM BHAIYA, TIKU BHAIYA, DISHA DIDI, SHEFALI** and **MASOOM.** I thank them for their moral support, and for creating a fun-loving working atmosphere. When in need, instant help and support was provided by my colleagues. I am truly indebted to them for their positive support and concerns for me.

I would like to thank the Computer Centre staffs, namely **JIGAR SIR, TEJAS SIR, MISHRA SIR** and **VAIBHAV** for their help regarding computational problems. I am also thankful to staff members of the library for their continuous support.

I would also like to thank **PROF. ANIL BHARADWAJ**, Director, Physical Research Laboratory (PRL), and **PROF. P. JANARDHAN**, Dean, PRL to allow me to avail the facilities of PRL to complete my thesis work.

I am lifelong grateful to my beloved parents, **SHRI YOGESHKUMAR SHAH** and **SMT. VISHAKHABEN SHAH**, who worked hard to educate me. Their hard work inspired me to do hard in my studies. I ever express my immense sense of gratitude to them for their love, care, encouragement and support right from my birth. I will be deeply beholden to them. It is my pleasant duty to recall with gratitude the everlasting affection, encouragement and all support which I have been receiving from my sister. I also dedicate this thesis to my lovely sister **RIDDHI PARIKH** for her constant motivation and love. I also gathered courage from the warm wishes coming from my lovely and cute nieces, **JIYA** and **JUHI**. I am thankful to my jiju **NAINESH PARIKH** for his encouragement. I am also thankful to all my cousins and family members for their love and support. I thank the God for giving me such supportive and lovable family.

Last but not the least, the most important people in my life, my loving husband **BHAVAN SHAH** and our wonderful daughter **YASHVI**, deserve a special appreciation for their love, care, patience and unconditional support. They never complained about anything even though they missed my presence a lot.

(SHAH SIDDHI YOGESHKUMAR)

PREFACE

The understanding of the complex behavior of the atmosphere and ionosphere of various planets requires a balanced effort in theoretical modeling, experiments and analysis of the observations. The ability to combine observations with numerical models is critical in predicting atmospheric phenomena. Theoretical models based on fundamental principles in conjunction with data from recent satellites are important to improve our understanding of the physical, chemical and dynamical processes in the atmosphere. Given such importance, modeling of planetary atmospheres has been a major thrust area in India. To help in strengthening this area of research, we have developed various models to study the complex behavior of Martian atmosphere/ionosphere and dust storms. The Martian ionosphere can be divided into D, E, and F region. The Mars ionospheric F- region is formed by EUV radiation with wavelength 90 – 1026 Å at altitude ~125-135 km. Mars ionospheric E-region is produced by X-ray radiation with wavelength of 10-90 Å at altitude ~100-112 km. At night the E-region of Mars disappear because of absence of the primary source of ionization. Most of the radio occultation experiments used radio frequency wave to infer the ionosphere of Mars. The lower ionosphere is made of D region. The D peak of electron density occurs at altitude range from 25 to 35 km. In D layer electron density is less than the positive ion density from which the existence of negative ions can be inferred. The primary sources of ionization of D region are galactic cosmic rays.

The Solar flare response is a key problem in the planetary ionosphere. The solar flares are sudden increases in solar radiation associated with sunspots. The occurrence of solar flares directly depends on sunspot number which in turn depends on solar activity.

The sunspot number increases as the sun progresses in its activity during 11-years solar cycle. The solar flares are broadly classified as X, M, C and B-classes according to their X-ray brightness in the wavelength range 1 to 70 Å. The GOES, which operate in geostationary orbit above the earth track the solar flares reaching the earth by measuring the X-ray, flux at shorter wavelengths (0.5-3 Å and 1-8 Å) because these shorter wavelength X-ray fluxes are more sensitive to the solar flares. Among various Mars' missions, the MGS was the only mission, which measured a large number of electron density profiles (5600) in the ionosphere of Mars during solar maximum conditions so far. It observed the responses of about 32 solar flare events in the electron density profiles of Martian ionosphere. Therefore, the electron density data of MGS is very useful to understand the implications of solar flares on Mars. We have also carried out modelling of D and E region ionosphere of Mars due to impact of soft X-rays, hard X-rays and GCR radiations during solar flare and non-flare conditions. We have reported hard X-rays as a new source of ionization, which also produced D region ionosphere of Mars. We have studied response of all 32 Solar flare in the E region ionosphere of Mars. The effect of ozone, dust, and Schuman resonance frequencies in D region ionosphere of Mars are also studied. In absence of measurements, our model results will provide a benchmark values that may help to guide the design of future atmospheric/ionospheric payloads of Mars.

In the present thesis, we have described eight chapters. In chapter 1, we have introduced Martian atmosphere and ionosphere. In the second chapter, we have described three theoretical models, (1) Energy loss method, (2) Analytical yield spectrum, and (3) Continuity equation. In the third chapter, we have studied effect of solar flares in D region ionosphere of Mars.

In the fourth chapter, we have discussed the response to solar X-ray flares in the E region ionosphere of Mars. In the fifth chapter, we have studied seasonal variability of the ozone in lower ionosphere of Mars. In the sixth chapter, we have described the electrical conductivity and SR frequencies in the lower ionosphere of Mars. In the seventh Chapter, we have discussed the summary and conclusions on the work carried out in the present investigation. Finally, in eighth Chapter, we described the future work.

❑❑❑

Contents

List of Figures

CHAPTER - 1

INTRODUCTION

CONTENTS

The study of Martian atmosphere is of great interest for the study of comparative meteorology, in order to better understanding of the Earth's atmosphere. The study of Martian atmosphere requires a combination of modelling and observations. In this Chapter, we have given the brief introduction of lower and upper ionosphere of Mars. We have described the chemistry of the lower and upper ionosphere of Mars. We have used ion dust chemical reactions in the ion-neutral model of Martian lower ionosphere. We have also discussed the neutral atmosphere of Mars. The each chapters of the present thesis are described in brief in section 1.3.

1.1 INTRODUCTION

Our solar system has eight planets namely Mercury, Venus, Earth, Mars, Jupiter, Saturn, Uranus, and Neptune. The Mercury, Venus, Earth, and Mars are terrestrial planets. They are also called inner planets because they orbiting closed to Sun. Other planets are gas giant planets and known as outer planets. There have been found many evidences that the physical and chemical processes operating on Mars and Earth are nearly same. Both the planets have seasons and polar caps. Mars has been considered the best candidate for harboring extraterrestrial life. This is notably due to its atmosphere, which has shaped its surface and has created climate conditions which were suitable for sustaining liquid water and life in the past. We have studied the atmosphere and ionosphere of Mars to understand their physical and chemical processes.

The theoretical models have been developed by several investigators for lower and upper ionosphere of Mars. (Whitten et al., 1971; Shinagawa and Cravens, 1988; Haider et al., 2009a, 2016; Fox, 1996; Molina-Cuberos et al., 2002; Nagy et al., 2004; Forget et al, 2013). The ability to combine the chemistry of lower and upper ionosphere requires a balanced effort in the theoretical modelling. The present thesis focuses on the studies of D and E regions of Mars' ionosphere due to effects of solar flares and dust storms.

1.1.1 Ionosphere of Mars

The ionosphere of Mars is mainly produced by Galactic Cosmic Rays (GCR), X-rays and solar EUV radiation incident on the top of the atmosphere. The Martian ionosphere can be divided into upper and lower ionosphere. The schematic diagram of ionospheric electron density is given in figure 1.1. The D region is produced at about 25 km in the Mars' lower ionosphere due to impact of GCR and hard X-rays (0.5-3 Å). The E and F regions are produced in the upper ionosphere at about 110 km and 130 km due to impact of soft X-rays (10-100 Å) and solar EUV radiation (100-1026 Å) respectively. The chemistry in the lower and upper ionosphere of Mars is described below:

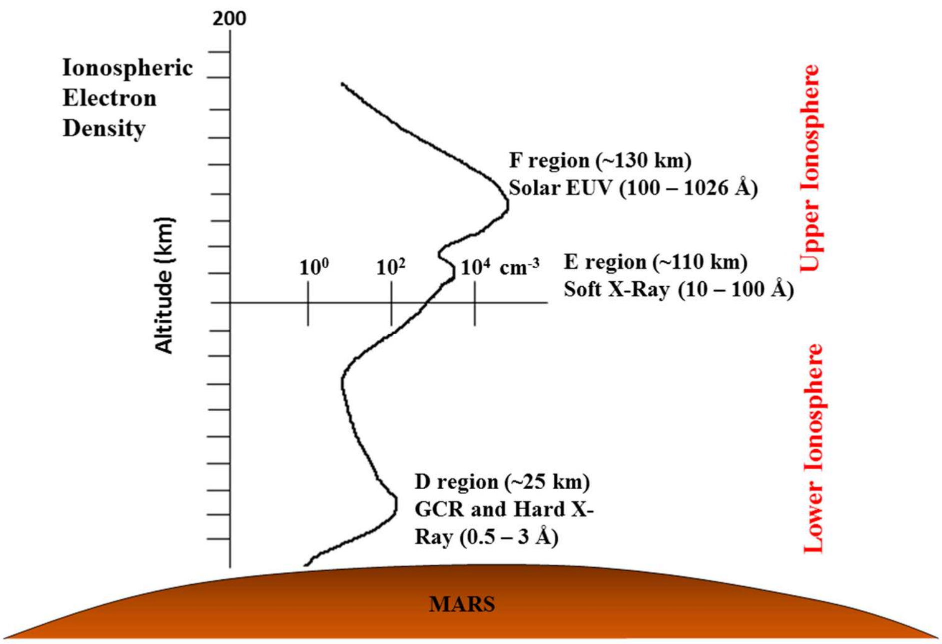

Figure 1.1 Schematic representation of D, E, and F region ionosphere of Mars

1.1.2 Chemistry of the lower ionosphere

The figure 1.2 represents the schematic diagram of ion-aerosol and ion-neutral reactions in the lower ionosphere of Mars. It should be noted that the rate coefficients of ion-neutral reactions, photodissociation of positive and negative ions, electron attachment to neutrals and photodetachment of negative ions do not depend on temperature. Only ion-ion recombination coefficients depend on the temperature as given below (Haider et al., 2007):

$$\alpha_{ii} = 6.010^{-8} \text{ x } (300/T)^{0.5} + 1.25 \text{ x } 10^{-25} \text{ x M x } (300/T)^{4} \quad (1.1)$$

where T is the temperature and M is the neutral density. The neutral temperature is given by Fox (1993). The neutral densities of 12 gases viz. CO_2, N_2, O_2, O, CO, Ar, O_3, H_2, H_2O, NO, NO_2, and HNO_3 in the lower atmosphere of Mars are given by Molina-Cuberos et al. (2002). Three body reactions are very important in the lower atmosphere.

The photodissociation and electron photodetachment rate coefficients are divided by 2.25 to take into account of the lower solar radiation at Mars in comparison to that on Earth. In figure 1.2 we have also included charged aerosol-charged aerosol (α), positive ion-negative charged aerosol (α_1), electron – positive charged aerosol (βe), ion-aerosol attachment (β), and negative ion-positive charged aerosol (α_2) reactions which occur in presence of aerosols in the Martian atmosphere. The flux of incident GCR is exponentially attenuated in the lower atmosphere and is calculated between values 10^3-10^{-5} particles m^{-2} s^{-1} GeV^{-1} $ster^{-1}$ at energy range of 1-1000 GeV (Molina-Cuberos et al., 2002; Haider et al., 2009a). It should be noted that the flux of GCR depends on the solar activity which decelerates it in the interplanetary medium. Therefore, we do not know what fraction of GCR is actually precipitating in the Martian atmosphere. This flux has been used by several investigators for average condition to study the lower ionosphere of Mars (Whitten et al., 1971; Molina-Cuberos et al., 2002; Haider et al., 2007, 2009a, 2016).

Recently Sheel and Haider (2016) have calculated nine positive ions ($H_3O^+(H_2O)_4$, $H_3O^+(H_2O)_3$, $H_3O^+(H_2O)_2$, $H_3O^+H_2O$, H_3O^+, CO_2^+, $O_2^+CO_2$, NO^+, and O_2^+) and eight negative ions ($CO_3^-(H_2O)_2$, $CO_3^-H_2O$, CO_3^-, CO_4^-, $NO_2^-H_2O$, $NO_2^-(H_2O)_2$, $NO_3^-H_2O$, and $NO_3^-(H_2O)_2$) in the lower ionosphere of Mars. In the positive ion chemistry 100% ions of O_2^+ and CO_2^+ are produced initially due to impact of GCR. These ions are fully destroyed by H_2O in the formation of H_3O^+. Once H_3O^+ has been produced water vapour molecules are attached with it. The ion H_3O^+ is then lost by three body reaction in the formation of cluster hydrated ions $H_3O^+(H_2O)_n$ for n = 1, 2, 3, and 4.

In the negative ion chemistry O^- and O_2^- ions are produced initially due to electron capture process. Later in presence of three body reactions CO_3^- and CO_4^-were produced due to loss of O^- and O_2^- with CO_2, respectively. The ion CO_3^- is destroyed by NO forming NO_2^-. When CO_3^- and NO_2^- ions are formed, H_2O is attached with them. The production and loss reactions in the formation of positive and negative cluster ions are given below:

$$H_2O^+(H_2O)_n + H_2O + M \leftrightarrow H_3O^+(H_2O)_{n+1} + M \qquad (1.2)$$

$$CO_3^-(H_2O)_n + H_2O + M \leftrightarrow CO_3^-(H_2O)_{n+1} + M \qquad (1.3)$$

$$NO_2^-(H_2O)_n + H_2O + M \leftrightarrow NO_2^-(H_2O)_{n+1} + M \qquad (1.4)$$

The chemical reactions (1.2), (1.3) and (1.4) are reversible. The hydrated ions are the dominant in lower ionosphere of Mars. These ions are producing the D layer in the lower ionosphere of Mars. The densities of these major ions decreases by 1-2 orders of magnitude near the surface during the major dust storm as compared to that estimated for absence of dust storm period (Haider at al., 2010; 2015; Sheel and Haider, 2012, 2016). In absence of dust storm the chemistry of dust reactions are not considered in the chemical model (Sheel and Haider, 2016). The dust reactions are playing very important role in the sink process of ion-dust model (Haider et al., 2010). This model is used in Chapter 3 and 6.

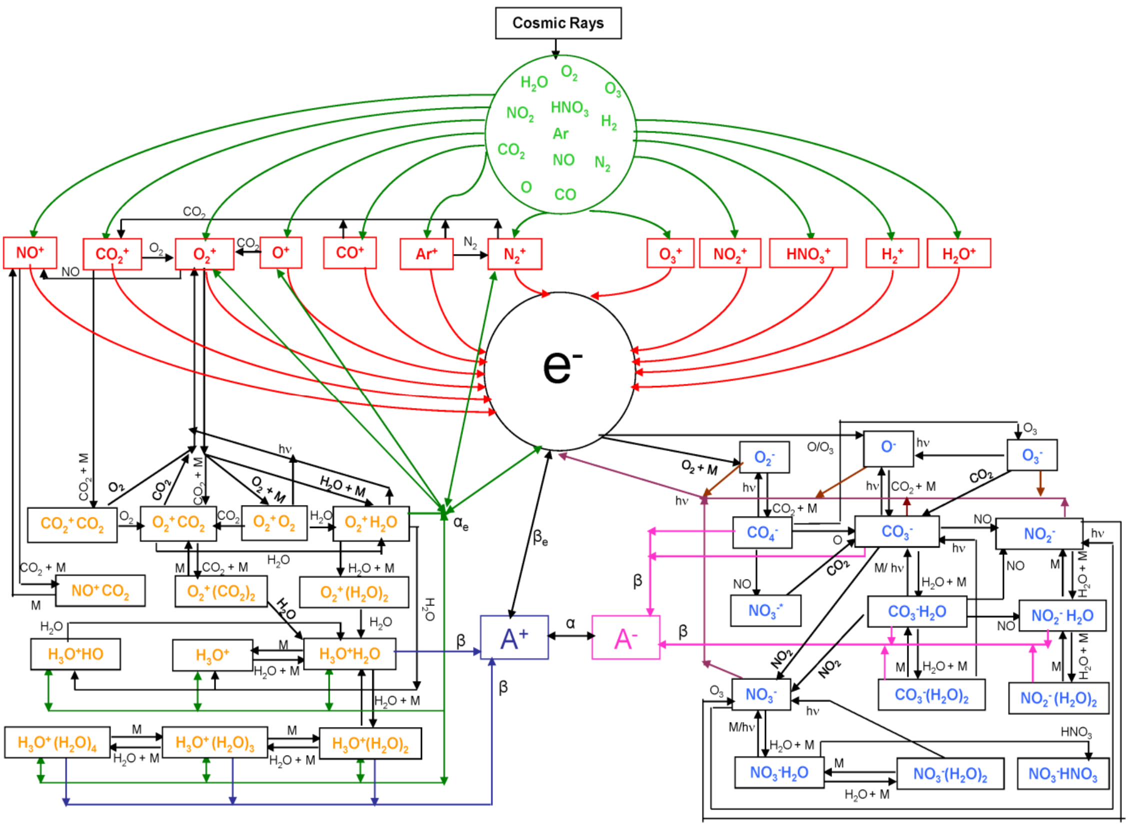

Figure 1.2 Schematic representations of ion-aerosol and ion-neutral chemistry in the lower atmosphere of Mars.

1.1.3 Chemistry of the upper ionosphere

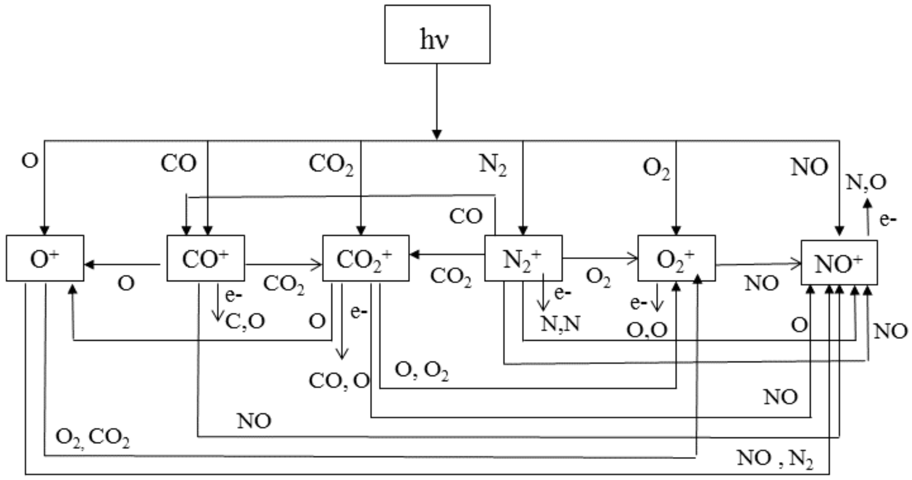

Figure 1.3 Schematic representation of the chemistry in the upper ionosphere of Mars

Solar X-ray radiation ionize the neutral species in the E region ionosphere of Mars producing CO_2^+, O_2^+, O^+, CO^+, NO^+ and N_2^+ ions. The production and loss reactions in the chemistry of the upper ionosphere are shown in figure 1.3 (Haider et al., 2016). The photoionization rate of CO_2^+ is a dominant process in the upper ionosphere of Mars. This ion is mainly destroyed by atomic oxygen and produces a dominant ion O_2^+. The ion O_2^+ is later destroyed by dissociative recombination process. The ion NO^+ is produced in the E region due to impact of O_2^+ with N and NO (Haider et al., 2009a) and it is fully destroyed by dissociative recombination reaction.

The ion CO^+ is lost due to charge exchange reaction with CO_2. This process destroyed all CO^+ ions in the Martian ionosphere (Haider et al., 2007). Fox (2009) found that the charge exchange reaction between CO_2^+ and O is the dominant source of O^+, at heights below 190 km. Above this altitude solar EUV radiation is an important production mechanism for O^+. This chemical model is used in Chapter 4. The simplified photochemistry in the upper ionosphere of Mars for the formation of major ion O_2^+ and electron density is given below (Haider et al., 2016):

$$CO_2 + hv \rightarrow CO_2^+ + e$$

$$CO_2^+ + O \rightarrow O_2^+ + CO$$

$$CO + O_2^+ \rightarrow O^+ + CO_2$$

$$O^+ + CO_2 \rightarrow O_2^+ + CO$$

$$O_2^+ + e \rightarrow O + O$$

1.2 NEUTRAL ATMOSPHERE OF MARS

The atmosphere of Mars is about 100 times thinner than Earth's atmosphere. Martian' atmosphere has been observed by many spacecrafts such as Mariner 6, 7, 9; Mars 2, 3 and 6; Mars Global Surveyor (MGS) and Mars Express (MEX). First detection and measurement of neutral species were made by neutral mass spectrometers on board Viking Landers 1 and 2 (Nier and McElroy,1977). They obtained a mass spectra from 1 to 49 amu. Later, an accelerometer and radio occultation experiment on MGS provided large datasets of atmospheric density at various locations in the upper and lower atmosphere of Mars, respectively. These observations indicated that the atmosphere of Mars contains CO_2, N_2, Ar, CO, O_2, and NO with contribution to the total air density of about 95.5%, 2:7%, 1.5%, 0.4-1.4%, 0.17%, 0.008% respectively. The Viking landers also carried a retarded potential analyzer (RPA) (Hanson et al., 1977), which provided information on the major ion densities and plasma temperatures in the ionosphere up to an altitude of about 300 km. The atmospheric pressure and temperature of Mars on the surface is around 6 mbar (600 Pascal's) and 220K. The atmosphere of Mars is quite dusty, giving the Martian sky a light brown or orange color when seen from the surface. Data from the Mars Exploration Rovers indicated that suspended dust particles within the atmosphere are roughly 1.5 μm. The atmosphere of Mars can be broadly divided into upper and lower atmosphere.

1.2.1 Lower atmosphere of Mars

The lower atmosphere of Mars exists below 100 km where gases are mixed and eddy diffusion is dominant. The lower atmosphere of Mars is characterized by strong coupling between pressure, temperature, neutral density and winds. MGS and MEX have observed temperature, pressure and total density in the lower atmosphere of Mars with radio occultation experiment (Bougher et al., 2001; Hinson et al., 1999; Patzold et al., 2005). Photochemical models have predicted concentrations of O_2, O_3, CO_2, CO and other neutral species in the lower atmosphere of Mars (Belton and Hunten, 1966; Parkinson and Hunten, 1972; Rodrigo et al., 1990; Krasnopolsky, 2003). Molina-Cuberos et al. (2002) have reported neutral model atmosphere of 12 gases (CO_2, N_2, Ar, O_2, CO, H_2, H_2O, O, O_3, NO, NO_2 and HNO_3) in the lower atmosphere of Mars. We have plotted these density profiles in figure 1.4 which we have used in our study.

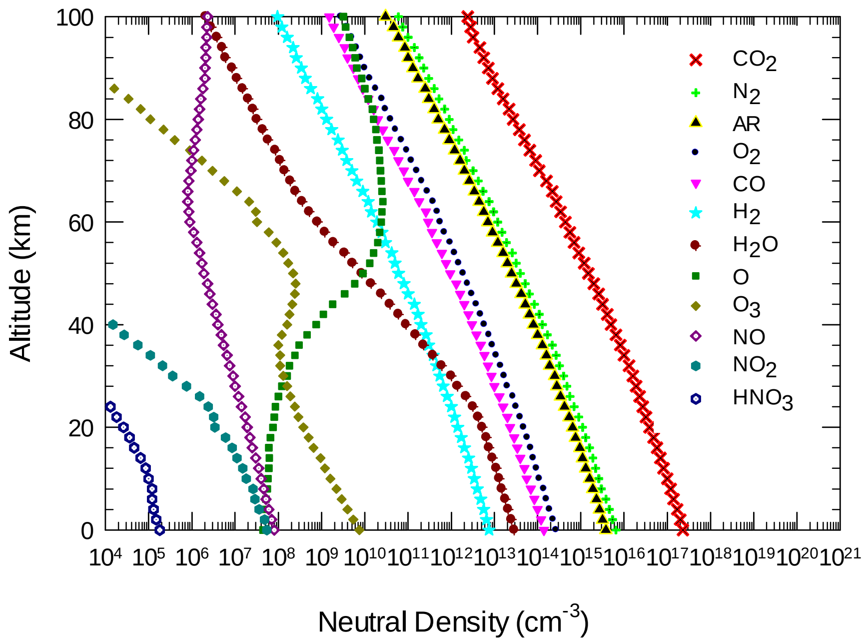

Figure 1.4 Neutral model atmosphere in the lower atmosphere of Mars (taken from Molina-Cuberos et al, 2002)

1.2.2 Upper atmosphere of Mars

The upper atmosphere exists above 100 km where molecular diffusion dominates and the constituents are separated according to their molecular mass. The first direct measurement of the upper atmosphere of Mars was performed by neutral mass spectrometer on board Viking 1 and 2 Landers (Nier and McElroy, 1977). Carbon dioxide was found to be the major constituent at all altitudes below 180 km. Viking Landers observed neutral compositions of CO_2, N_2, CO, O_2, and NO. The atomic oxygen density could not be measured by mass spectrometer on Viking 1 and 2. However, it was inferred from O_2^+ and CO_2^+ densities measured by Retarding Potential Analyzer (RPA) experiment on Viking 1 and 2 (Hanson et al., 1977).

The altitude profiles of air density, mixing ratios of CO_2, O_2, O, CO, O_3, H, H_2, N_2, Ar and H_2O, neutral temperature, pressure and winds are given by Mars Climate Database (MCD; Millour et al., 2014, https://hal.archives-ouvertes.fr/hal-01139592) at different seasons, latitude and longitude in the dayside and nightside atmosphere above the surface of Mars for different scenarios of dust climatology (Millour et al., 2014). We have obtained neutral density profiles of few gases from MCD (by multiplying their mixing ratios with the air density) for observing conditions of MGS and MEX as required for modeling purposes in Chapters 3 to 6. The altitude profiles of the neutral densities of CO_2, N_2, O_2, O and CO are shown in figure 1.5 between 100 km and 200 km during the dayside atmosphere of Mars.

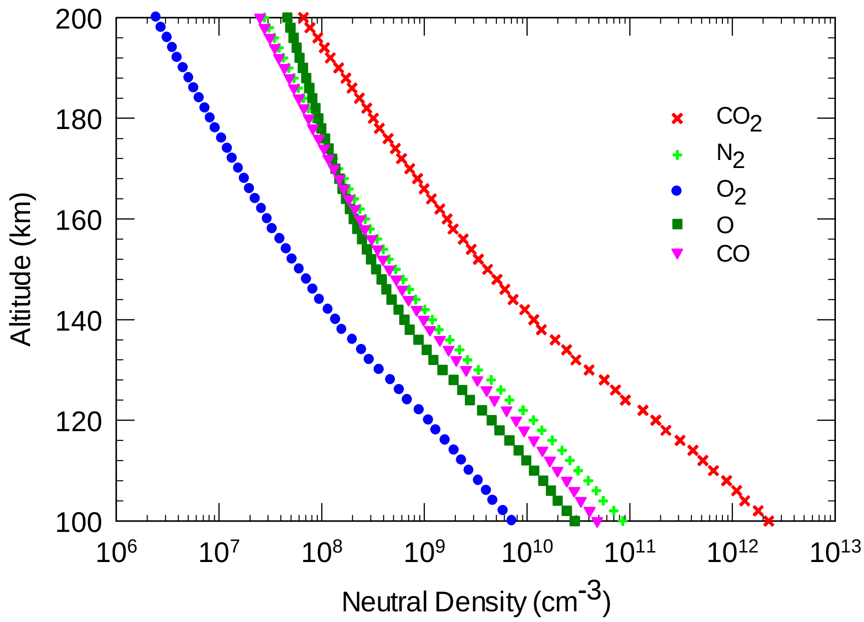

Figure 1.5 Neutral model atmosphere in the upper atmosphere of Mars (taken from Millour et al, 2014)

1.3 CHAPTERIZATION

The present thesis contains eight Chapters, in which we have described ion and neutral chemistry, dusty ionosphere, seasonal variability of atmospheric gases and response to X-ray flares in the lower atmosphere of Mars.

The first Chapter describes a brief introduction of the research work carried out in the present thesis. In this Chapter we have also introduced atmosphere and chemistry of the lower and upper ionosphere of Mars. The dust plays an important role in the lower ionosphere of Mars. We have also included ion-dust reactions in the chemical model of the lower ionosphere of Mars.

In the second chapter, we have described three theoretical models, which have been used in the present thesis. These methods are (1) Energy loss method, (2) Analytical Yield Spectrum (AYS), and (3) Continuity equation.

In the third chapter, we have studied the responses of solar X-ray flares in the D region ionosphere of Mars. The ion-neutral chemistry model developed by us is used to calculate ion production rate, ion and electron densities in the D region ionosphere of Mars.

In the fourth chapter, we have studied the effect of solar X-ray flares in the E region of Mars' ionosphere. We have analyzed the responses of 32 solar X-ray flares that were observed by MGS. We have also calculated biological dose of 32 solar X-ray flares. The ion and electron densities were also calculated in the E region ionosphere of Mars. The estimated electron densities are compared with MGS observation.

In the fifth chapter, we have studied seasonal variability of column ozone in lower ionosphere of Mars and compared with the Spectroscopy for Investigation of the

Characteristics of the Atmosphere of Mars (SPICAM) instrument onboard MEX. In this Chapter the condensation and sublimation processes of ozone gas is understood. We have calculated the ion production rate of ozone, at low, mid and high latitudes between altitudes 0 to 60 km in presence and absence of dust storm.

In the sixth chapter, we have studied electrical conductivity and Schumann Resonance (SR) frequency in the lower ionosphere of Mars in presence of a major dust storm that occurred in Martian Year (MY) 25 at low latitude region (25°–35°S).

Finally in the seventh Chapter, we have summarized the work carried out in the present thesis.

Chapter eight is devoted to the future directions of our proposed work.

❒❒❒

REFERENCES

Belton, M. J., and Hunten, D. M. (1966), The Abundance and Temperature of CO_2 in the Martian Atmosphere, Astrophys. J., **145**, 454-467.

Bougher, S. W., Engel, S., Hinson, D. P., and Forbes, J. M (2001), Mars Global Surveyor radio science electron density profiles: Neutral atmosphere implications, Geophys. Res., Lett.,**28**, 3091-3094.

Forget, F., Wordsworth, R., Millour, E., Madeleine, J. B., Kerber, L., Leconte, J, et al. (2013), 3D modelling of the early Martian climate under a denser CO_2 atmosphere: Temperatures and CO_2 ice clouds, Icarus, **222**, 81-99.

Fox, J. L. (1993), The production and escape of nitrogen atoms on Mars, J. Geophys. Res., **98**, 3297–3310.

Fox, J. L. (2009), Morphology of the dayside ionosphere of Mars: Implications for ion outflows, J. Geophys. Res., **114**, 1-18.

Fox,J. L., Zhou, P., Bougher, S. W (1996), The Martian thermosphere/ionosphere at high and low solar activities. Adv. Space Res., **17**, 203-218.

Haider, S. A., Batista, I. S., Abdu, M. A., Santos, A. M., Shah, S. Y, et al.(2016), Flare X-ray photochemistry of the E region ionosphere of Mars. J. Geophys. Res., Space Physics, **121**, 6870-6888.

Haider, S. A., Batista, I. S., Abdu, M. A., Muralikrishna, P., Shah, S. Y., and Kuroda, T (2015), Dust storm and electron density in the equatorial D region ionosphere of Mars: Comparison with Earth's ionosphere from rocket measurements in Brazil. J. Geophys. Res., **120**, 8968-8977.

Haider, S. A., Abdu, M. A., Batista, I. S., Sobral, J. H., Kallio, E., Maguire, W. C, et al. (2009a), On the responses to solar X-ray flare and coronal mass ejection in the ionosphere of Mars and Earth, Geophys. Res. Lett., **36**, 1-5.

Haider, S. A., Sheel, V., Smith, M. D., Maguire, W. C., and Molina-Cuberos, G. J(2010), Effect of dust storm on the D region of the Martian ionosphere: Atmospheric electricity, J. Geophys. Res., **115**, 1-10.

Haider, S. A., Singh, V., Choksi, V. R., Maguire, W. C., and Verigin, M. I. (2007), Calculated densities of $H_3O^+(H_2O)_n$, $NO_2^-(H_2O)_n$, $CO_3^-(H_2O)_n$ and electron in the night time ionosphere of Mars: Impact of solar wind electron and galactic cosmic rays, J. Geophys, Res., **112**, 1-9.

Hanson, W. B., Sanatani, S., and Zuccaro, D. R (1977), The Martian ionosphere as observed by the Viking retarding potential analyzers, J. Geophys, Res., **82,** 4351-4363.

Hinson, D. P., Simpson, R. A.,Twicken, J. D., Tyler, G. L., and Flasar, F. M. (1999), Initial results from radio occultation measurements with mars global surveyor, J. Geophys, Res., Planets, **104**, 26,997-27,012.

Krasnopolsky, V. A (2003), Spectroscopic mapping of Mars CO mixing ratio: Detection of north-south asymmetry, J. Geophys, Res., Planets, **108**, (4)1-(4)13.

Millour, E., Forget, F., Spiga, A., Navarro, T., Madeleine, J. B., Pottier, A, et al. (2014), A new Mars climate database v5.1, paper 1301 presented at The Fifth International Workshop on Mars Atmosphere: Modeling and Observations, Oxford, U. K., Jan. 2014.

Molina-Cuberos, G. J., Lichtenegger, H., Schwingenschuh, K., López-Moreno, J. J., and Rodrigo, R..(2002), Ion- neutral chemistry model of lower ionosphere of Mars. J. Geophys, Res., **105**, (3)1-(3)7.

Nagy, A. F., Winterhalter, D., Sauer, K., Cravens, T. E., Brecht, S., Mazelle, C, et al. (2004), The plasma environment of Mars, Space Sci. Rev., **111**, 33–114.

Nier, A. O., and McElroy, M. B (1977), Composition and structure of Mars' upper atmosphere: Results from the neutral mass spectrometers on Viking 1 and 2, J. Geophys, Res., **82**, 4341-4349.

Parkinson, T. D., and Hunten, D. M (1972), Spectroscopy and Acronomy of O_2 on mars, J Atmos Sci., **29**, 1380-1390.

Pätzold, M., Tellmann, S., Häusler, B., Hinson, D., Schaa, R., and Tyler, G. L (2005), A sporadic third layer in the ionosphere of Mars, Science, **310**, 837– 839.

Rodrigo, R., Garcia-Alvarez, E., Lopez-Gonzalez, M. J., and Lopez-Moreno, J. J (1990), A non steady one-dimensional theoretical model of Mars' neutral atmospheric composition between 30 and 200 km, J. Geophys, Res: Solid Earth, **95**, 14,795-14,810.

Sheel, V., and Haider, S. A (2012), Calculated production and loss rates of ions due to impact of galactic cosmic rays in the lower atmosphere of Mars. Planet. Space Sci., **63**, 94-104.

Sheel, V., and Haider, S. A (2016), Long-term variability of dust optical depths on Mars during MY24–MY32 and their impact on subtropical lower ionosphere: Climatology, modeling, and observations, J. Geophys. Res., **121**, 8038-8054.

Shinagawa, H., and Cravens, T. E (1988), A one-dimensional multispecies magneto hydrodynamic model of the dayside ionosphere of Venus. J. Geophys. Res: Space Physics, **93**, 11263-11277.

Whitten, R. C., Poppoff, I. G., and Sims, J. S. (1971), The ionosphere of Mars below 80 km altitude, I, Planet. Space Sci., **17**, 243-250.

❒❒❒

CHAPTER - 2

A LITERATURE SURVEY AND METHODOLOGY USED

CONTENTS

The modeling is an important tool to understand various physical and chemical processes involved in the formation of Martian ionosphere. In this Chapter we have described energy loss method, AYS, and coupled continuity equation to calculate the production rates and densities of ions and electrons in the Martian ionosphere. The energy loss and AYS methods have been used to calculate the production rates in the lower and upper ionosphere of Mars respectively. In the energy loss method the particle losses its kinetic energy or it is deflected from its original path due to elastic and inelastic collisions. The AYS model is based on the Monte Carlo method. The coupled continuity equation calculates production rate, loss rate, and ion and electron densities in the Martian ionosphere.

2.1 INTRODUCTION

There have been developed several theoretical models in the planetary ionospheres. These include diffusion transport (Swartz, 1972), two stream method (Banks and Nagy, 1970; Haider et al., 1992), Boltzmann transport equations (Mantas and Hanson, 1979), Continuous slowing down approximation (Green and Barth, 1965; Singhal et al., 1992), AYS approach (Green et al., 1977; Haider and Singhal, 1983; Seth et al., 2002; Haider et al., 2002), Magneto Hydrodynamics Model (Shinagawa and Cravens, 1992, Tanaka,1998); and Mars Thermosphere General Circulation Model (MTGCM) (Bougher et al., 2000).

In the present thesis we have used three models viz. (1) Energy loss model, (2) Coupled continuity equations, and (3) AYS approach as given below:

2.1.1 Energy Loss method

In the energy loss method, a charge particle losses its kinetic energy or it is deflected from its original path involving four principal type of interactions: (1) Inelastic collision with bound atomic electrons are usually the predominant mechanism by which a charged particle losses kinetic energy in an absorber. As a result of such collision, one or more atomic electrons experience a transition to an excited state or to an ionization state, (2) Inelastic collision with a nucleus experiences a deflection. In some but not all such deflections, a quantum of radiation is emitted (bremsstrahlung) and a corresponding amount of kinetic energy is lost by the colliding particles, (3) In inelastic scattering the incident particle is deflected but does not radiate, nor does it excite the nucleus. The incident particle losses kinetic energy required for conservation of momentum between the two particles. (4) An incident charge particle may be elastically deflected in the field of the atomic electron of struck atom. Energy and momentum are conserved, and energy transfer is generally less than the lowest excitation potential of the electrons, so that the interaction is really with the atom as a whole. Such collisions are significant for the case of very low energy (< 100 eV) incident electrons. In the absorbing material, a moving particle is slowed down and finally brought to at rest by the combined action of all four of these elastic and inelastic collisions processes. From collision theory, one can obtain the probabilities of any particular change of the direction of motion of incident particle. After the first collision, these probabilities can be applied a second collision, then to a third etc. The basic formula for energy loss per cm path into the material media by a particle traveling with the velocity 'v' and undergoing inelastic collisions is written as given by Evans (1995) and Haider et al. (2007).

$$\left(\frac{dE}{dh}\right) = 2\pi \frac{e^4}{m_o \mathrm{v}^2} NZ \left\{ \ln\left(\frac{m_o \mathrm{v}^2 E}{I^2 (1-\beta^2)}\right) - \beta^2 \right\} \qquad (2.1)$$

In equation (2.1), by substituting $m_o v^2 = \beta^2 m_o c^2$ and $E + m_o c^2 = m_o c^2 (1 - \beta^2)^{-0.5}$, we get

$$\left(\frac{dE}{dh}\right) = 4\pi r_o^2 \frac{m_o c^2}{\beta^2} NZ \left\{ \ln \beta \left(\frac{E + m_o c^2}{I}\right) \left(\frac{E}{m_o c^2}\right)^{\frac{1}{2}} - \frac{1}{2}\beta^2 \right\} \tag{2.2}$$

where I is mean ionization potential, N is the neutral density, r_o is the classical electron radius with $4\pi\, r_o^2 = 1.0 \times 10^{-24}$ cm^2/electron, $\beta^2 = (v/c)^2 = 1 - [(E/m_o c^2) + 1]^{-2}$, $m_o c^2 = 0.51$ MeV, Z is the mean atomic number, and c is the velocity of light. Using equation (2.2) the ion production rate due to impact of GCR at height h and solar Zenith angle χ is given below:

$$J(h, \chi) = \frac{2\pi}{Q} \int_E^\infty \left(\frac{dE}{dh}\right) F(\chi, E)\, dE \tag{2.3}$$

where Q = 35 eV is the energy required for the formation of an electron ion pair, χ is Solar Zenith Angle (SZA), F is the total differential flux of GCR being expressed in cm^{-2} s^{-1} GeV^{-1} ster^{-1} at height h.

2.1.2 Coupled continuity equations

This model considers the variation in one direction which is usually taken as vertical height 'h' in the present thesis. The time dependent continuity and momentum equations are given below:

$$\frac{\partial n_i}{\partial t} = p_i - n_i\, l_i - \frac{\partial \phi}{\partial h} \tag{2.4}$$

$$\varphi_i = n_i v_h = D_i n_i \left[\frac{1}{n_i}\frac{\partial n_i}{\partial h} + \frac{m_i g}{K T_i} + \frac{T_e/T_i}{n_e}\frac{\partial n_e}{\partial h} + \frac{1}{T_i}\frac{\partial}{\partial h}\left(T_e + T_i\right) + \frac{\alpha_i}{T_i}\frac{\partial T_i}{\partial h} \right] \qquad (2.5)$$

where n_i is the number density of ith ion at altitude h; t is time; p_i is the production of ion; $\varphi_i$is the vertical diffusive flux of ion; D_i is diffusion coefficient of ion; m_i is the mass of ion; g is the gravitational acceleration at Mars; K is the Boltzmann constant; T_i is the ion temperature; T_e is electron temperature; n_e is electron density and α_i is the thermal diffusion coefficient of ion. The flux divergence term in equation (2.4) includes second order derivatives of n_i with respect to h. The differential equations can be solved by finite difference method using lower and upper boundary conditions. At lower boundary chemistry plays major role and we can take initially minimum value of electron density for iteration at lower height. At upper boundary plasma is under diffusive equilibrium and diffusion flux is nearly constant with height. In the Martian ionosphere, the chemical life time $\tau_c = l^{-1}$, is much less up to 200 km than the molecular diffusion time constant $\tau_m = H_i^2 / D_i$. Thus, the vertical diffusion can be neglected below this altitude. Now we get the chemical equilibrium equation as given by

$$\frac{\partial n_i}{\partial t} = p_i - n_i l_i \qquad (2.6)$$

For the steady state condition, $\frac{\partial n_i}{\partial t} = 0$, then $p_i = n_i l_i$

For the above equation it is clear that under photochemical equilibrium steady state condition the production and loss reaction are equal. By using the continuity equation we have developed ion neutral model which calculates the densities of positive ions, negative ions and electrons in lower ionosphere of Mars. In the upper ionosphere negative ions are absent. Thus, sum of the positive ion densities is equal to the electron density ($\Sigma n_i = n_e$). The negative and positive ions are both present in the lower ionosphere. Therefore, sum of the positive ion densities is equal to the electron density and sum of the negative ion densities ($\Sigma n_i = \Sigma n^- + n_e$). In the ion-neutral model we have used GCR for the ionization of the neutral gases in the lower atmosphere of Mars. More than 100 chemical reactions have been used in this model to calculate the positive and negative ions in the lower atmosphere of Mars (see figure 1.2). In the upper ionosphere we have used about 23 chemical reactions (see figure 1.3). The solar EUV radiations mainly ionize the neutral gases in the upper ionosphere.

2.1.3 AYS method

The AYS model was initially generated by Singhal et al. (1980) and Singhal and Green (1981) using a Monte Carlo method. These authors have fitted yield spectra analytically. Later AYS model has been used and extended by several investigators (Haider and Singhal, 1983; Singhal and Haider, 1984; Haider and Bhardwaj, 2005; Haider et al., 2011; Haider and Mahajan, 2014; Pandya and Haider, 2014; Thirupathaiah et al., 2019; Siddhi et al., 2019; Haider and Masoom, 2019). In the Monte Carlo model a real number between 0 and 1.0 called from a random generator is determined whether a collision took place or not. If not, the amount of energy lost through Coulomb losses to the ambient electrons was calculated from Butler-Buckingham formula (Dalgarno et al., 1963) and was added to the accumulated energy loss. If the collision with atmospheric gases occurred, a further decision was to take whether the collision was elastic or inelastic. For the elastic collision the scattering angle calculation was carried out by Porter and Jump (1978). If the scattering event is inelastic, then the states which are excited and ionized were calculated from Jackman et al. (1977). In AYS model the monoenergetic electrons of energy range from 25 eV to 10 keV were introduced in a gas medium. Using this method, the energy of secondary or tertiary electrons and their positions were calculated at that time when primary electrons ionize the atmospheric constituents. In this way two, three, four and five dimensional yield spectrum functions U (E, E_o), U (E, z, E_o), U (E, r, z, E_o) and U (E, r, z, E_o, θ) were generated respectively for the calculation of the yield of any state in the mixture of gases (Green et al., 1977; Singhal et al., 1980; Singhal and Green, 1981; Haider et al., 2011; Haider and Mahajan, 2014). These functions depend on incident energy E_o, secondary energy E, radial distance r, height z and polar angle θ. The yield spectrum function represents the energy spectrum of all the electrons in the medium. The function for $Z < 0$ and $Z > 0$ represents the backscattered and forward electrons respectively.

2.2 YIELD SPECTRA

In Section 2.1.3 the Yield Spectra is presented in terms of two, three, four and five dimensional functions. The two dimensional yield spectra U (E, E_o) is used where the magnetic field is uniform and horizontal in direction (Pandya and Haider, 2014; Haider et al., 2009a, 2016; Thirupathaiah et al., 2019; Siddhi et al., 2019). In this case vertical transport of the electron is inhibited. Thus the electrons lose their energy at the same height where they are produced. The three dimensional yield spectra U (E, z, E_o) is used where the magnetic field is uniform and vertical in direction (Haider et al., 2010; Haider et al., 2013). In this case the vertical transport of the electron is included. The four dimensional yield spectra U (E, r, Z, E_o) is applied for auroral studies on Earth, Comets and Mars where both the longitudinal and radial distances of the electrons should be considered (Bhardwaj et al., 1990; 1995; Haider and Masoom, 2019). In some aeronomical problems such as backscattering of the electrons and bremsstrahlung generation by auroral electrons, the polar angle distribution associated with the electron spectrum plays an important physical role. For such studies, the five dimensional yield spectrum U (E, r, z, E_o, θ) was generated by introducing the polar angle (θ) in four dimensional yield spectra (Green et al., 1977; Singhal et al., 1980; Singhal and Green, 1981). In this thesis we have not used three, four and five dimensional yield spectra. Therefore, these spectra are not described in detail.

2.2.1 Two dimensional Yield Spectra

In Chapters 3 and 4, we have used two dimensional yield spectra to study the electron energy degradation processes in the dayside Martian ionosphere. The two dimensional yield spectra U (E, E_o) in unit $(eV)^{-1}$ is defined as,

$$U(E,\ E_o) = \sigma_T(E) f(E, E_0) = N(E)/\Delta E \tag{2.7}$$

where σ_T (E) is the total inelastic cross section and N (E) is the number of electrons in the bin centered at E after one bin has emptied and before the next lower non empty bin of width ΔE centered at E is considered, f (E, E_o) is the equilibrium flux or degradation spectrum of Spencer and Fano (1954). The analytic form of the equation (2.7) is given below (Haider et al., 2016):

$$U(E,\ E_o) = U_a(E, E_0) H(E_m - E - E_0) + \delta(E - E_0) \tag{2.8}$$

where H is the Heavy side function with E_m the minimum threshold of the states considered, δ (E-E_o) is the Dirac delta function, E is the energy of secondary electrons, E_o is the energy of incident electrons in eV. $U_a(E,E_o)$ can be represented by

$$U_a(E,\ E_o) = C_0 + C_1 X + C_2 X^2 \tag{2.9}$$

$$\mathrm{X} = \frac{\left(E_o/1000\right)^{0.585}}{E+1} \tag{2.10}$$

where C_o, C_1 and C_2 are adjustable parameters. For mixtures of gases, the composite yield spectra U^c (E, E_o) are obtained by weighting the component of the yield spectrum (Singhal and green, 1981; Haider and Singhal, 1983; Singhal and Haider, 1984) as

$$U^c(E, E_o) = \sum_i f_i U_i(E, E_o) \qquad (2.11)$$

In this equation, f_i is the fractional composition of gas i and is given by:

$$f_i = \frac{S_i\, n_i(h)}{\sum_j S_j\, n_j(h)} \qquad (2.12)$$

where S_i/S_j is the average value of $\sigma_{Ti}(E)/\sigma_{Tj}(E)$ between E_{min} = 2 eV to E_o, $\sigma_{Ti}(E)$ is the total (elastic + inelastic) cross sections, and $n_i(h)$ is the neutral density at altitude h.

2.2.2 Generalized Yield Spectra

The AYS approach and its analytical fitting parameters are given for N_2 and O only (Singhal and Green, 1981). The analytical parameters for other gases are also obtained which are not much different from these gases. For a mixture of gases in the planetary atmospheres generalized/composite yield spectra are obtained by weighting the component of the yield spectra as given below:

$$U^c(E, E_o) = \Sigma\, f_i U_i(E, E_o) \qquad (2.13)$$

$$U^c(E, z, E_o) = \Sigma\, f_i\, U_i(E, z, E_o) \qquad (2.14)$$

$$U^c(E, r, z, E_o) = \Sigma\, f_i U_i(E, r, z, E_o) \qquad (2.15)$$

$$U^c(E, r, z, E_o, \theta) = \Sigma\, f_i U_i(E, r, z, E_o, \theta) \qquad (2.16)$$

where f_i is given by equation (2.12), $U_i(E,E_o)$, $U_i(E, z, E_o)$, $U_i(E, r, z, E_o)$ and $U_i(E, r, z, E_o, \theta)$ are two, three, four and five dimensional yield spectra of i^{th} gases respectively. The yield spectra depend on elastic and inelastic cross-sections of the atmospheric gases. These cross-sections are very important for the studies of aurora, airglow and ionosphere. We have calculated inelastic cross-sections of electron impact on CO_2, N_2, O_2, O and CO using semi-empirical formula of A.E.S. Green and his collaborators (Sawada et al., 1972a, b; Jackman et al, 1977; Jackman and Green, 1979; Green and Sawada, 1972). The total elastic cross-sections due to electron impact on CO_2, N_2, O_2, O and CO are also calculated using semi-empirical formula given by Porter and Jump (1978). The elastic cross-sections are larger than the inelastic-cross sections at low energy. At high energy the inelastic cross-sections are larger than the elastic cross-sections. AYS approach suffers from the strong weakness in that it does not account for the electron-ambient electron interactions rigorously and therefore the results of the calculations based on AYS approach are less reliable at higher altitude where the electron density becomes appreciable in the F region.

2.2.3 Applications of Yield Spectra

AYS approach for studying the interaction of low and medium energy electrons with planetary atmospheres has been found very useful in the applications cited in the present thesis. The calculations based on AYS approach are simpler to carry out as compared to those by other methods mentioned in Section 2.1. However, the simplicity of this approach is not at the cost of accuracy of results for the following two reasons: (1) the electron impact inelastic cross sections used by various workers in this field are not consistent with each other and a factor of 2 or more variation is clearly found among the cross sections values, and (2) The experimental observations of solar EUV, X-ray flux and neutral model atmosphere are also depict strong variations and a consensus has not yet been reached. Until such time more accurate input data and experimental observations are not available, AYS approach will remain a useful tool for studying many problems of space physics related to excitation/ionization processes. The utility of the ease of calculation using the AYS approach has been clearly demonstrated in the calculations of the research problems undertaken in Chapters 3 and 4 of this thesis. These problems would certainly have been prohibitively expensive using other approaches which can be more accurate but would have required a very long computer time and effort. The generalized AYS approach can also be used fruitfully for mixture of gases in planetary atmospheres.

2.3 IONIZATION PROCESSES USED

Ionization is the process by which an atom or a molecule acquires a negative or positive charge by gaining or losing electrons, often in conjunction with other chemical changes. Ionization occurs whenever sufficiently energetic charged particles or radiant energy travel through gases, liquids, or solids. Charged particles, such as alpha particles and electrons from radioactive materials, cause extensive ionization along their paths. Energetic neutral particles, such as neutrons and neutrinos, are more penetrating and cause almost no ionization. Pulses of radiant energy, such as X-ray and gamma-ray photons, can eject electrons from atoms by the photoelectric effect to cause ionization. The energetic electrons resulting from the absorption of radiant energy and the passage of charged particles in turn may cause further ionization, called secondary ionization. Here, we have described the ionization processes due to impact of photon and photoelectron in dayside ionosphere of Mars.

2.3.1 Photoionization rates

The electromagnetic radiation produces photoelectron in the atmosphere of Mars due to following chemical reactions:

$$X + hv \rightarrow X^{+} + e_p \tag{2.17}$$

where X is atmospheric gas, e_p is the photoelectrons having energies between 1-100 eV. The above process occurs in the atmosphere when photon energy hv ($\leq$ 1025Å) is equal to or greater than the ionization potential (I_p) of gas X. The photoelectrons again collide with gases and lose their energy in the atmosphere through excitation and ionization processes. The ion production rate due to absorption of solar EUV/X-ray radiation at altitude Z and solar zenith angle χ is given below:

$$\mathrm{q}\ (\mathrm{Z}, \chi) = \sum_i \mathrm{n_i}(Z)\ \sum_\lambda \sigma_\mathrm{i}^\mathrm{I}(\lambda)\,\mathrm{I}(\infty, \lambda,)\ \exp\left[-Ch(\chi)\sum_i \sigma_\mathrm{i}^\mathrm{A}(\lambda)\int_z^\infty \mathrm{n_i}(\mathrm{z})dZ\right] \tag{2.18}$$

where $\sigma_i^A(\lambda)$ and $\sigma_i^I(\lambda)$ are the total photoabsorbtion and photoionization cross section of i^{th} gas at wavelength λ, Ch(χ) is the Chapman function, $n_i(Z)$ is the neutral density at altitude Z and I (∞,λ) is the incident solar flux at the top of the Martian atmosphere. Using equation (2.18) the primary photoelectron production rate is calculated as below:

$$\mathrm{Q}\ (\mathrm{Z}, \mathrm{E}) = \sum_i \mathrm{n_i}(\mathrm{z})\ \sum_\lambda \sigma_\mathrm{i}^\mathrm{I}(\lambda)\,\mathrm{I}(\mathrm{Z}, \lambda,)\,\delta\left(\frac{\mathrm{hc}}{\lambda} - \mathrm{E} - \mathrm{W_i}\right) \tag{2.19}$$

$$\mathrm{I}\ (\mathrm{Z}, \lambda) = I(\infty, \lambda)\exp\left[-Ch(\chi)\sum_i \sigma_\mathrm{i}^\mathrm{A}(\lambda)\int_z^\infty \mathrm{n_i}(\mathrm{z})dZ\right] \tag{2.20}$$

where $\delta\left(\frac{hc}{\lambda} - E - W_i\right)$ is the delta function in in which $\frac{hc}{\lambda}$ is incident photon energy and E is the energy of ejected photoelectrons. W_i is the ionization potential of i^{th} constituents. The Q (Z,E) is the primary photoelectron production rates of i^{th} species in the unit of cm^{-3} eV^{-1} s^{-1}.

2.3.2 Photoelectron production rates

Using two dimensional spectra we can calculate photoelectron impact ionization rate as given below:

$$J_i(Z) = \int_{W_i}^{\infty} dE \int_{W_i}^{E_0} Q\,(Z,E)\; U^c(E,E_o)\,P_i(E)\,dE_o \tag{2.21}$$

where P_i is the ionization probability as given below:

$$P_i(E) = \frac{n_i(Z)\,\sigma_i(E)}{\sum n_i(Z)\,\sigma_{T_i}(E)} \tag{2.22}$$

Q (Z, E) and $U^c(E, E_o)$ are calculated from equations (2.19) and (2.13) respectively. The ion production rates J_i (Z) for ith species are calculated from equation (2.21) in the unit of $cm^{-3}s^{-1}$.

2.3.3 Photoelectron flux

The production rates are directly related to photoelectron flux. The photoelectron production rates are defined below:

$$J_i(Z) = n_i(Z) \int_{W_i}^{\infty} \phi(Z,E)\,\sigma_i(E)\,dE \tag{2.23}$$

Comparing equation (2.21) and (2.23) we get,

$$\phi(\mathrm{Z}, \mathrm{E}) = \int_{E}^{\infty} \frac{Q(Z,E)\, U^{c}(E,Eo)}{\sum n_i \sigma_{T_i}(E)}\, dE_0 \tag{2.24}$$

This equation calculates the photoelectron flux spectra of energy E al altitude Z in the unit of $cm^{-2}\ s^{-1}\ eV^{-1}$.

❒❒❒

REFERENCES

Banks, P. M., and Nagy, A. F. (1970), Concerning the influence of elastic scattering upon photoelectron transport and escape, J. Geophys. Res., **75**, 1902–1910.

Bhardwaj, A., Haider, S. A., Singhal, R. P (1995), Consequences of cometary aurora on the carbon chemistry at Comet P/Halley, Adv. Space Res. **16**, 31–36.

Bhardwaj, A., Haider, S. A, and Singhal, R. P (1990), Auroral and photoelectron fluxes in cometary ionosphere, Icarus, **85**, 216–228.

Bougher, S. W., Engel, S., Roble, R. G., and Foster, B (2000), Comparative terrestrial planet thermospheres: 3. Solar cycle variation of global structure and winds at solstices, J. Geophys. Res., **105**, 17,669–17,692.

Dalgarno, A., McElroy, B. M. and Moffett R. J (1963), Electrons temperatures in the neutrino experiments. In: Proc. Ind. Acad. Sci. **63**, 217.

Evans, R. D (1995), The atomic nucleus, McGraw Hill Publication, USA, 567–591.

Green, A. E. S., and Sawada, T (1972), Ionization cross sections and secondary electron distributions, J Atmos Sol-TerrPhy, **34**, 1719-172.

Green, A. E. S., and Barth, C. A (1965), Calculations of Ultraviolet Molecular Nitrogen Emissions from the Aurora, J. Geophys. Res., **70**, 1083-1092.

Green, A. E. S., Jackman, C. H., and Garvey, R. H (1977), Electron impact on atmospheric gases, 2 Yield spectra, J. Geophys. Res., **82**, 5104–5111.

Haider, S. A., and Bhardwaj, A (2005), Radial distribution of production rates, loss rates and densities corresponding to ion masses$\leqslant$ 40 amu in the inner coma of Comet Halley: Composition and chemistry, Icarus, **177** 196-216.

Haider, S. A., and Mahajan, K. K (2014), Lower and upper ionosphere of Mars, Space Science Reviews, **182**, 19-84.

Haider, S. A., and Masoom, J (2019), Modeling of diffuse aurora due to precipitation of H^+-H and SEP electrons in the nighttime atmosphere of Mars: Monte Carlo simulation and MAVEN observation, J. Geophys. Res. Space Physics (In press)

Haider, S. A., and Singhal, R. P (1983), Analytical yield spectrum approach to electron energy degradation in Earth’s atmosphere, J. Geophys. Res., **88**, 7185–7189.

Haider, S. A., Batista, I. S., Abdu, M. A., Santos, A. M., Shah, S. Y, et al. (2016), Flare X-ray photochemistry of the E region ionosphere of Mars, J. Geophys. Res., Space Physics, **121**, 6870-6888.

Haider, S. A., Kim, J., Nagy, A. F., Keller, C. N., Verigin, M. I., Gringauz, K. I, et al. (1992), Calculated ionization rates, ion densities and airglow emission rates due to precipitating electrons in the nightside ionosphere of Mars, J. Geophys. Res., **97**, 10,637–10,641.

Haider, S. A., Abdu, M. A., Batista, I. S., Sobral, J. H., Kallio, E., Maguire, W. C, et al.(2009a), On the responses to solar X-ray flare and coronal mass ejection in the ionosphere of Mars and Earth, Geophys. Res. Lett., **36**, 1-5.

Haider, S. A., Mahajan, K. K., and Kallio, E (2011), Mars ionosphere: A review of experimental results and modeling studies, Reviews of Geophysics, **49**, 1-37 2011RG000357.

Haider, S. A., Pandya, B. M., and Molina-Cuberos, G. J (2013), Nighttime ionosphere caused by meteoroid ablation and solar wind electron-proton-hydrogen impact on Mars: MEX observation and modeling, J. Geophys. Res., Space Physics, **118**, 6786-6794.

Haider, S. A., Seth, S. P., Kallio, E., and Oyama, K. I. (2002), Solar EUV and electron-proton-hydrogen atom-produced ionosphere on Mars: Comparative studies of particle fluxes and ion production rates due to different processes, Icarus, **159**, 18–30.

Haider, S. A., Sheel, V., Smith, M. D., Maguire, W. C., and Molina-Cuberos, G. J. (2010), Effect of dust storm on the D region of the Martian ionosphere: Atmospheric electricity, J. Geophys. Res., **115**, 1-10A12336.

Haider, S. A., Singh, V., Choksi, V. R., Maguire, W. C., and Verigin, M. I (2007), Calculated densities of $H_3O^+(H_2O)_n$, $NO_2^-(H_2O)_n$, $CO_3^-(H_2O)_n$ and electron in the nighttime ionosphere of Mars: Impact of solar wind electron and galactic cosmic rays, J. Geophys, Res., **112**, 1-9, A12309.

Jackman, C. H., and Green, A. E. S (1979), Electron impact on atmospheric gases, 3. Spatial yield spectra for N_2, J. Geophys, Res., Space Physics, **84**, 2715-2724.

Jackman, C. H., Garvey, R. H., and Green, A. E. S (1977), Electron impact on atmospheric gases: 1. Updated cross sections, J. Geophys. Res., **82**, 5081–5090.

Mantas, G. P., and Hanson, W. B (1979), Photoelectron fluxes in the Martian atmosphere, J. Geophys. Res., **84**, 369–385.

Pandya, B. M., and Haider, S. A (2014), Numerical simulation of the effects of Meteoroid ablation and solar EUV/X-ray radiation in the dayside ionosphere of Mars: MGS/MEX observations, J. Geophys. Res. Space Physics, **119**, 9228–9245.

Porter, H. S., and Jump Jr F. W (1978), Analytical total and angular elastic electron impact cross sections for planetary atmosphere, Tech. Rep. CSC/TM-78/CO17, prepared for NASA, Goddard Space Flight Centre, Comput. Sci. Corp., Greenbelt, Md.

Sawada, T., Strickland, D. J., and Green, A. E. S (1972a), Electron energy degradation in CO_2, J. Geophys. Res.,**77**, 4812-4818.

Sawada, T., Sellin, D. L., and Green, A. E. S (1972b), Electron impact excitation cross sections and energy degradation in CO, J. Geophys. Res.,**77**, 4819-4828.

Seth, S. P., Haider, S. A., and Oyama, K. I.(2002), The photoelectron flux and nightglow emissions of 5577 and 6300 Å due to solar wind electron precipitation in Martian atmosphere, J. Geophys. Res., **107**, 1324 (19)1-(19)-11.

Shinagawa, H., and Cravens, T. E (1992), The ionospheric effects of a weak intrinsic magnetic field at Mars, J. Geophys. Res., **97**, 1027-1035.

Siddhi Y. S, Haider,S. A., Molina-Cuberos, G. J., Abdu, M. A., Batista, I (2019), A coupled model of the D and E regions of Mars' ionosphere for flare and non-flare electron density profiles: Comparison with Earth's ionosphere, Icarus. (Under review).

Singhal, R. P., and Green, A. E. S (1981), Spatial aspects of electron energy degradation in atmospheric oxygen, J. Geophys. Res., **85**, 4776-4780.

Singhal, R. P., and Haider, S. A (1984), Analytical yield spectrum approach to photoelectron fluxes in the Earth's atmosphere, J. Geophys. Res., **89**, 6847–6852.

Singhal, R. P., Jackman, C. H., and Green, A. E. S(1980), Spatial aspects of low and medium energy electron degradation in N2, J. Geophys. Res., **85**, 1246–1254.

Singhal, R. P., Chakravarty, S. C., Bhardwaj, A., and Prasad, B (1992), Energetic Electron Precipitation in Jupiter's Upper Atmosphere, J. Geophys. Res., **97**, 18245-18256.

Spencer, L. V., and Fano, U(1954), Energy spectrum resulting from electron slowing down, Phys. Rev., **93**, 1172–1181.

Swartz, W. E (1972), Electron production, recombination and heating in the F region of ionosphere, Sci. Rep. 381, Ionosphere. Res. Lab., Pa. State Univ., University Park, Pa.

Tanaka, T. (1998), Effects of decreasing ionospheric pressure on the solar wind interactionwith non-magnetized planets, Earth and planet Space, **50**, 259.

Thirupathaiah, P., Shah, S. Y., and Haider, S. A. (2019), Characteristics of solar X-ray flares and their effects on the ionosphere and human exploration to Mars: MGS radio science observations, Icarus, **330**, 60-74.

❑❑❑

CHAPTER - 3

EFFECTS OF SOLAR X-RAY FLARES IN THE D REGION IONOSPHERE OF MARS

CONTENTS

There are no measurements in D region ionosphere of Mars. Therefore, it is necessary to evaluate opportunity for obtaining the observations of electron density profile in D region ionosphere of Mars. In this Chapter we have discussed the effect of solar flares in the D region ionosphere of Mars. The flare induced D layer was never reported earlier on Mars. We report a new source of ionization, in the D region ionosphere of Mars, which is hard X-rays (0.5-3Å). We have developed a model to calculate Ionospheric Electron Content (IEC) for flare and non-flare electron density profiles due to impact of hard X-rays (0.5-3Å) and Galactic Cosmic Rays (GCR) in D region of Mars' ionosphere. The flare D peak electron density profile is larger by 1-2 orders of magnitude than that produced for non-flare profiles. The modeling results for these two solar flares are compared with the Earth based ionosonde measurements in D region.

3.1 INTRODUCTION

Previous investigators have reported that the Martian ionosphere consist a permanent D layer due to impact of GCR (Whitten et al., 1971; Molina-Cuberos et al., 2002; Haider et al., 2015, 2016). In this Chapter we have reported first time a new source of D layer that was produced in the lower ionosphere by hard X-rays (0.5-3Å) (Siddhi et al., 2019). We have developed an ion-neutral chemical model to calculate the ion and electron densities due to impact of hard X-rays in presence of solar X-ray flares that occurred on 6 April, 2001 and 17 March, 2003. There is no measurement of flare profile in the daytime lower ionosphere of Mars similar to that observed on the Earth's ionosphere. Therefore we have compared estimated electron density profiles of Mars' ionosphere with Digisonde observation of Earth's ionosphere. The present ionospheric instruments (Radio occultation and Mars Advanced Radar for Subsurface and Ionosphere Soundings (MARSIS)) orbiting around Mars cannot observe the D region ionosphere. Therefore, we have compared estimated D layers of Mars' ionosphere with the observed D layer of Earth's ionosphere.

3.1.1 D layers of Earth and Mars' ionosphere

D layer is observed at ~65-75 km due to impact of Lyman alpha radiation ionizing the minor constituents NO in dayside ionosphere of Earth. GCR can affect the whole atmosphere down to the ground and became a major source of ionization in lower part of D region (cf. Schunk and Nagy, 2000). The peak electron density is observed ~ 1 x 10^4 cm^{-3} under normal condition in D region ionosphere of Earth. D layer begins to disappear in the nighttime of Earth's ionosphere because Lyman alpha radiation is absent and GCR produced a less amount of ionization. The solar Lyman alpha ionization is not affective in lower ionosphere of Mars because NO density in the Martian mesosphere is lower by ~2-3 orders of magnitude than that observed in the Earth's mesosphere (cf. Aikin, 1968; Hargreaves, 1992). The GCR is an important source of ionization for the formation of the D layer in the daytime as well as in the nighttime ionosphere of Mars. GCR has been reported an important source of D region ionosphere of Mars at altitude ~ 25-30 km with peak density ~1 x 10^2 cm^{-3} (Whitten et al., 1971; Molina-Cuberos et al., 2002; Haider et al., 2009a, 2010) which has been discussed in Chapter 1. The column densities in the Earth and Mars atmospheres are nearly ~2.2 x 10^{29} m^{-2} and ~2.3 x $10^{27}m^{-2}$, therefore GCR is penetrating deep into the ionosphere of Mars and form a D layer at lower altitudes than that observed in the Earth's ionosphere.

3.1.2 GCR impact on Earth and Mars

The high energy cosmic rays are propagating into the atmospheres of Earth and Mars and producing nucleonic cascades. The impact of primary GCR on to the atmospheric gases produces protons, neutrons and pions. Fast secondary nucleons can gain enough energy to increase the production of the particles by neutral collisions. Neutral pions quickly decay to gamma rays and their contribution to the energy deposition is very important in the lower part of the atmosphere. At the D peak region the maximum ion production rates are produced due to protons. The charged pions decay to muons, which do not decay before reaching the ground, and hence the muon energy is transferred to the surface which is shown in figure 3.1.

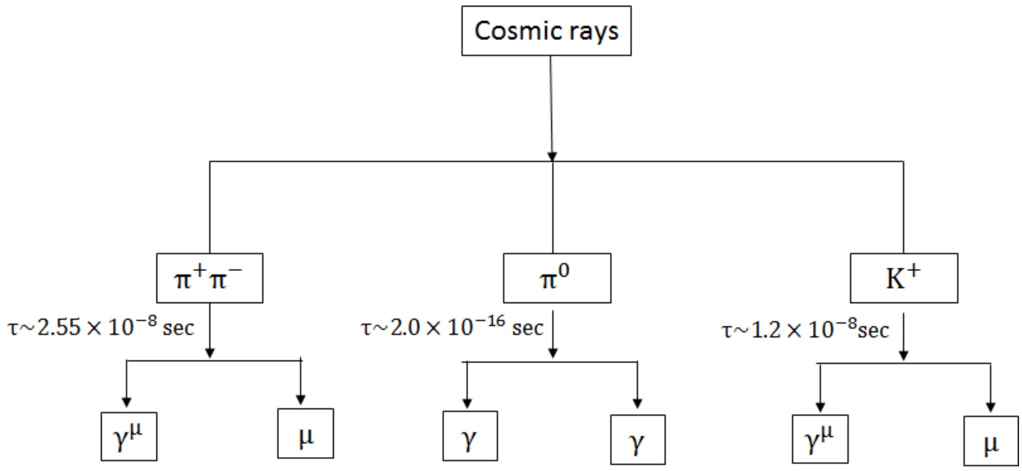

Figure 3.1 Schematic diagram and life time of secondary cosmic rays.

3.1.3 Hard X-rays impact on Earth and Mars

The hard X-rays are the highest energy X-rays (~ 10 keV), while the lower energy X-rays are referred to as soft X-rays. Since hard X-rays can penetrate more deeply into the atmosphere than the soft X-rays, they require a denser medium to be absorbed in the atmosphere. The hard X-rays (0.5-3 Å) is not an important source of the D layer in the Earth's ionosphere (Mitra, 1974; Davies, 1990). We have found that hard X-rays is a major source of the D layer in Mars' ionosphere after GCR impact ionization. Both sources have produced D layer at about 25-30 km. The D layer due to impact of hard X-rays is larger by an order of magnitude than that produced by GCR radiation (Siddhi et al., 2019). This is a first research result in the D region ionosphere of Mars. The hard X-rays produced maximum photoelectrons in the vicinity of ionization peak (Thirupathaiah et al., 2019). Therefore, photoelectron impact ionization rates are larger than the photoionization rates around the peak altitude.

3.2 SOLARX-RAY FLARES: HARD X-RAYS (0.5-3Å)

The solar X-ray flares are broadly classified as X, M, C and B-classes according to their X-ray brightness in the wavelength range 1 to 8 Å. X-class flares are major events that can trigger planet-wide radio blackouts and long-lasting radiation storms. M class flares are medium sized, which can cause minor radiation storms. C and B-class flares are smaller compared to X and M- class flares. The occurrence of solar flares depends on sunspot number which in turn depends on solar activity. The sunspot number increases as the sun progresses in its activity during 11-years solar cycle. Thus, the frequency of solar flare events varies with the 11-year sunspot cycle with rarely one event per day at solar minimum and 5-6 events per day at solar maximum (Mitra, 1974). A thorough understanding of the affects of solar flares on Martian environment is necessary for future human exploration missions for the safe operation of equipment's and astronauts' health because the enormous energy that suddenly strikes the Martian environment can damage the equipment's and lethal to astronauts. The solar flares can blackout communication and navigation of satellites, and skew the results. They can create a large amount of electrons and ions in the ionosphere of Mars. The solar flares often followed by giant clouds of electrified gas called Coronal Mass Ejections (CME) which can billow into the solar system and overtake Mars in a matter of hours or days (Haider et al., 2009b). Geostationary Operational Environment Satellite (GOES) is continuously measuring the solar X-ray flares reaching on the Earth at two shorter wavelength bands from 0.5-3Å and 1-8Å (Bornmann et al., 1996*)*.

3.2.1 Mars' Ionospheric responses to hard X-ray flares

The figure 3.2 (a, b) represents a time series of solar X-ray flux distributions in the wavelength range 0.5-3 Å that were observed by GOES 10 on 6 April, 2001 and 17 March, 2003. The corresponding observations have shown the greater enhancements at 19:21 UT and 19:05 UT respectively which can increase electron densities in the D region ionospheres of both Mars and Earth. Based on observed Sun-Mars distance, the peak solar X-ray flux should reach Mars ~6 min later. In figure 3.2 (a, b) the X-ray fluxes are not varying significantly with UT except at the flares time. Therefore, we have averaged X-ray flux over UT for both flare days (without adding flare time flux) and used in the model calculations of non-flare electron density profiles. The flare electron density profiles are calculated on 6April, 2001 and 17 March, 2003 by using the corresponding peak flare fluxes between 0 km and 70 km. These electron density profiles are shown in figure 3.4. The IEC is obtained by integrating these electron density profiles. The estimated IEC in presence and absence of solar X-ray flares are shown in figure 3.3 (c, d). The calculated ion density profiles in presence and absence of solar flares are shown in figures 3.5 and 3.6 respectively. These results are discussed in Sections 3.3.1-3.3.3 and compared with the D region profiles of Earth's ionosphere which have been measured at nearly same locations of MGS observations.

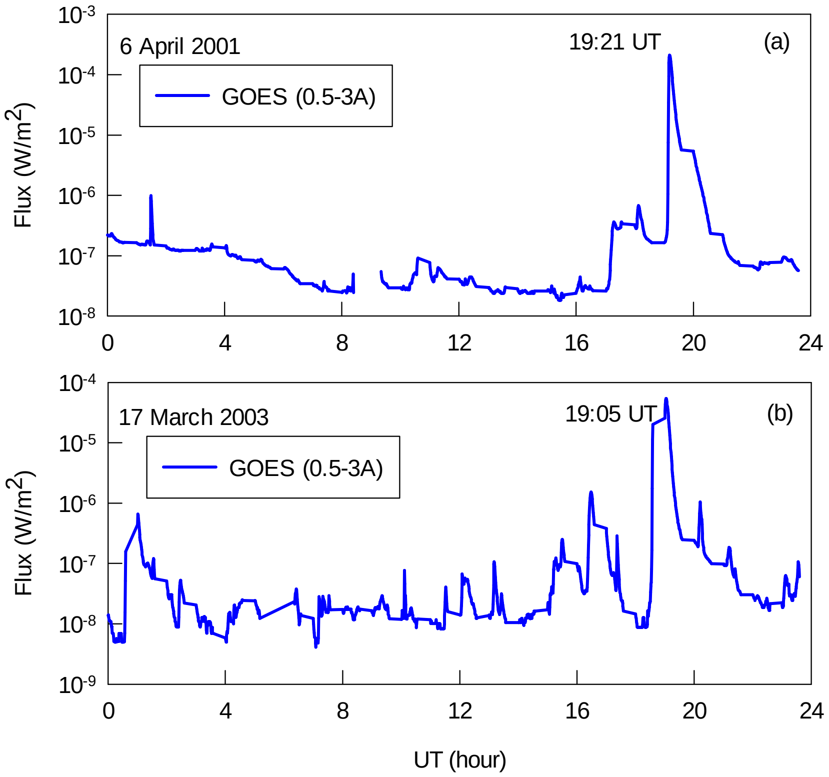

Figure 3.2 Time series of GOES flux plotted at wavelength (0.5-3 Å) for 6 April, 2001 and 17 March, 2003.

3.2.2 Earth's ionospheric responses to hard X-ray flares

The Digisonde measures the minimum plasma frequency f_{min} reflected by the upper layers of the Earth's ionosphere, which is a measure of the radio wave absorption due to electron-neutral collision (Reinisch et al., 2009). The electron density cannot be measured directly from Digisonde in the D region ionosphere of Earth. But enhancement in f_{min} is used as a proxy for the electron density increase in the D region ionosphere of Earth during the flare time. The effects of two flares mentioned in Section 3.2.1 were also observed by a Digisonde in the D region of the Earth's ionosphere at College AK (64.9°N, 212°E). The time distributions of f_{min} in the D region of Earth's ionosphere are shown in figures 3.3a and 3.3b for two flares that occurred on 6 April, 2001 and 17 March, 2003 respectively.

3.2.3 Comparison of D region ionospheres of Earth and Mars

In figures 3.3a and 3.3b we have compared f_{min} profiles obtained from Digisonde at College AK (64.9°N, 212°E) during two flare events that occurred on 6 April, 2001 and 17 March, 2003 in the D region ionosphere of Earth. Similarly in figures 3.3c and 3.3d we have compared IEC profiles obtained from the model for these two flare events in the D region ionosphere of Mars. Mars and Earth were nearly in the same line on both flare days (Earth-Sun-Mars angles were 30.2° and 62.3° when X-ray flares occurred on 6 April 2001 and 17 March 2003 respectively (website://www.windows.ucar.edu)). This confirms that both flares were leading towards Earth and Mars during these flare events. The IEC values for D region ionosphere of Mars were obtained by integrating 24 electron density profiles between 0 to 24 UT at altitude from 0 km to 70 km.

In figures 3.3a and 3.3b f_{min} increased by factors of 5 and 2 at 19:30 UT and 20:45 UT respectively. These observations were carried out by the Digisonde at 30 min and 15 min intervals respectively in the two cases. The maximum IEC of the D region ionosphere is calculated to be 15 x 10^{10} cm^{-2} and 7.5 x 10^{10} cm^{-2} at 19:27 UT and 19:11 UT respectively. The results over College AK also showed that there were significant enhancements in electron densities of the D region in the Earth' ionosphere due to impact of these flares as evidenced by the increase of minimum plasma frequency, f_{min} in the ionogram. It should be noted that flare responses on 6 April 2001 and 17 March 2003 shown in figures 3.3a and 3.3b were observed from ~30 min to ~1 hour between 19:10 - 19:40 UT and 18:50 - 19:50 UT respectively. So the resultant ionizations continued throughout the events after the flare peaks of GOES measurements. In figure 3.3b the time difference between the flare event and its associated f_{min} is very large. It seems that the enhancement in the f_{min} on 17 March 2003 is not associated with the flare event. We feel that this enhancement in f_{min} occurred by CME which was detected by GOES on 17 March 2003 at about 20:35 UT (https://www.spaceweather.com/en/archive).

The IEC and electron density profiles are also estimated for both days in the D region of Mars' ionosphere due to impact of GCR (not shown in figure 3.3). The IEC produced by hard X-rays is larger by about an order of magnitude than that produced by GCR. Our results suggests that the electron densities in the D regions of Earth and Mars' ionosphere were enhanced by factors of ~ 2-6 due to impact of these flares.

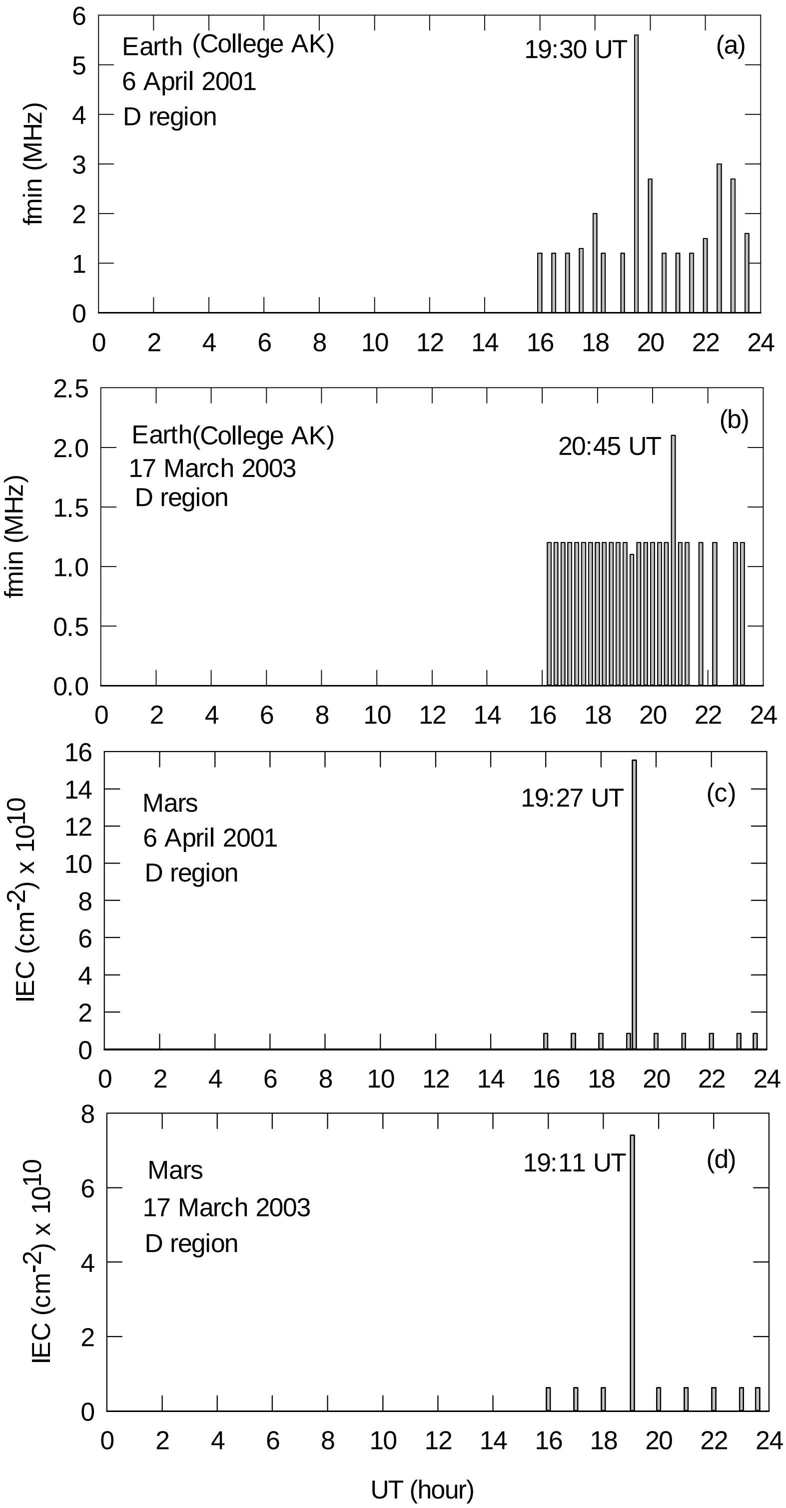

Figure 3.3. Time series of minimum plasma frequency f_{min} in D region of Earth's ionosphere (figures 3.3a and 3.3b) and Time series of estimated IEC in D region of Mars' ionosphere (figures 3.3c and 3.3d) for 6 April, 2001 and 17 March, 2003.

3.3 MODELING IN THE D REGION OF MARS' IONOSPHERE

We have used two dimension composite yield spectra U^c (E, E_o) and energy loss model from Chapter 2 (see equations 2.13 and 2.3) to calculate flare and non-flare production rate between 0-70 km in the Mars' ionosphere due to impact of three ionization sources: (1) Photoionization, (2) photoelectron impact ionization and (3) GCR impact ionization. These three ionization sources are discussed in Chapter 2. By using these three sources we have calculated the total ion production rates for flare and non-flare period. The total ion production rates are calculated using the equations as given below:

$$J(h,\chi) = \int_{E_o}^{\infty} dE_o \int_{E}^{\infty} P_i(E)\ R_i(h,\chi,E)\ U^c(E,E_o)\ dE + \int_{E}^{\infty} R_i(h,\chi,E)\ dE + \frac{2\pi}{Q}\int_{E}^{\infty}\left(\frac{dE}{dh}\right) F(\chi,E)\ dE \qquad (3.1)$$

where Pi (E) is the ionization probability at energy E, Ri (h, χ, E) is the primary photoelectron energy spectra (in $cm^{-3}\ s^{-1}\ eV^{-1}$) at altitude h and SZA χ, F (χ, E) is the GCR flux (Haider et al., 2009a). In equation (3.1) first term, second term and third term represent photoelectron impact ionization rate, photoionization rate and GCR impact ionization rate respectively. In the first term U^c(E, E_o) and Pi (E) are given by equations (2.13) and (2.22) respectively. In the first and second term R_i (h, χ, E) is calculated by equation (2.19). The third term is described in equation (2.19). The total ion production rate is used in the steady state coupled continuity model to calculate electron density profiles in the D region ionosphere of Mars. The electron density, n_e is calculated as $n_e = \Sigma n_i^+ - \Sigma n_i^-$, where Σn_i^+ is the sum of all positive ion densities and Σn_i^- is the sum of all negative ion densities, which is also described briefly in Chapter 2. Using charge neutrality and steady state conditions the electron density n_e is obtained by iteration process.

3.3.1 Electron densities in the D region of Mars' ionosphere

In figure 3.4 we have shown a comparison of the non-flare and flare electron density profiles estimated on 6 April, 2001 and 17 March, 2003 in D region ionosphere of Mars. The estimated electron density profile due to GCR impact is also shown in this figure. These calculations are carried out at solar zenith angle $\chi = 71^o$. In this model calculation we have taken neutral model atmosphere of 12 gases (Ar, H_2, H_2O, O_2, N_2, O, CO, CO_2, O_3, NO, NO_2 and HNO_3) from Millour et al. (2014) and Molina-Cuberos et al. (2002). The neutral temperature is also taken from Millour et al. (2014). The D peaks of non-flare profiles show a very small change on both flare days because the hard X-rays flux is almost same for both the days. The electron densities due to impact of GCR are nearly same for 6 April, 2001 and 17 March, 2003 because the same GCR flux is used for both days. The D peak electron densities of non- flare and flare profiles increased by about one and two orders of magnitude due to impact of hard X-rays than that produced by GCR impact ionization respectively. We have also calculated positive and negative ion densities for flare and non-flare periods due to impact of hard X-rays in the lower ionosphere of Mars. The flare profiles of ion densities estimated for 6 April, 2001 and 17 March, 2003 are described in Section 3.3.2. The Non-flare profiles of ion densities estimated for 6 April, 2001 and 17 March, 2003 are described in Section 3.3.3.

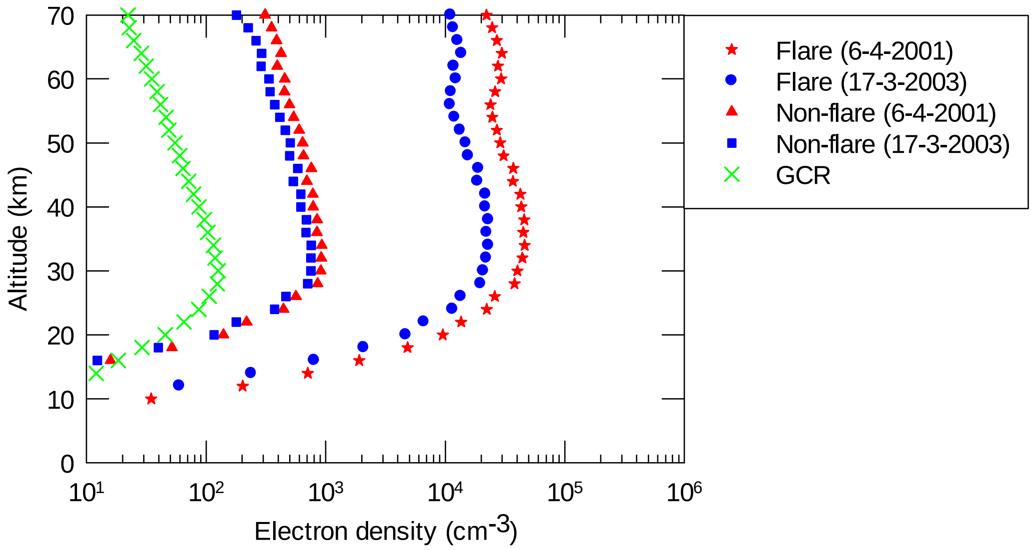

Figure 3.4. The estimated non-flare electron density profiles due to impact of hard X-rays (0.5-3 Å) on 6 April, 2001 and 17 March, 2003 are shown in figure (see red triangle and blue square). The estimated flare electron density profiles due to impact of hard X-rays (0.5-3 Å) on 6 April, 2001 and 17 March, 2003 are also shown (see red star and blue circle). The estimated electron density profile due to impact of GCR is shown by green crossed line.

3.3.2 Flare profiles of ion densities in the D region of Mars' ionosphere

The figures 3.5a and 3.5b represent the flare profiles of nine positive ions ($H_3O^+(H_2O)_4$, $H_3O^+(H_2O)_3$, $H_3O^+(H_2O)_2$, $H_3O^+H_2O$, H_3O^+, CO_2^+, $O_2^+CO_2$, NO^+, and O_2^+) and eight negative ions ($CO_3^-(H_2O)_2$, $CO_3^-H_2O$, CO_3^-, CO_4^-, $NO_2^-H_2O$, $NO_2^-(H_2O)_2$, $NO_3^-H_2O$, and $NO_3^-(H_2O)_2$) for 6 April, 2001 respectively. The flare profiles of these positive and negative ions for 17 March, 2003 are shown in figures 3.5c and 3.5d respectively. The flare electron density profiles are also plotted in each figure. The calculated densities due to flare impact on 17 March, 2003 are lower than that estimated for flare impact on 6 April, 2001. This is due to the fact that hard X-ray flare was not quiet intense on 17 March, 2003. The hydronium ions $H_3O^+(H_2O)_n$ for n =1-4 are dominant at altitude ≤ 70 km where three body reactions are important. Below 40 km the negative cluster ions $CO_3^-(H_2O)_n$ and $NO_2^-(H_2O)_n$ for n = 1-2 are dominant. Above this altitude electrons are dominant in the Mars' ionosphere. The flare electron density profiles have produced a broad peak at altitude 30 km in the lower ionosphere of Mars. In this model calculation the chemical scheme in the absence of dust storm is taken from figure 1.2. In Chapter 1 the chemistry of the production and loss reactions for figure 3.5 is given. Therefore, it is not given in Chapter 3 again. We have calculated peak values of flare ion density profiles to be ~ 4.0 x 10^4 cm^{-3} on 6 April, 2001 for the dominant ions $H_3O^+(H_2O)_2$ and $CO_3^-(H_2O)_2$. On 17 March, 2003 the peak values of these ions were estimated to be ~ 2.0 x 10^4 cm^{-3}.

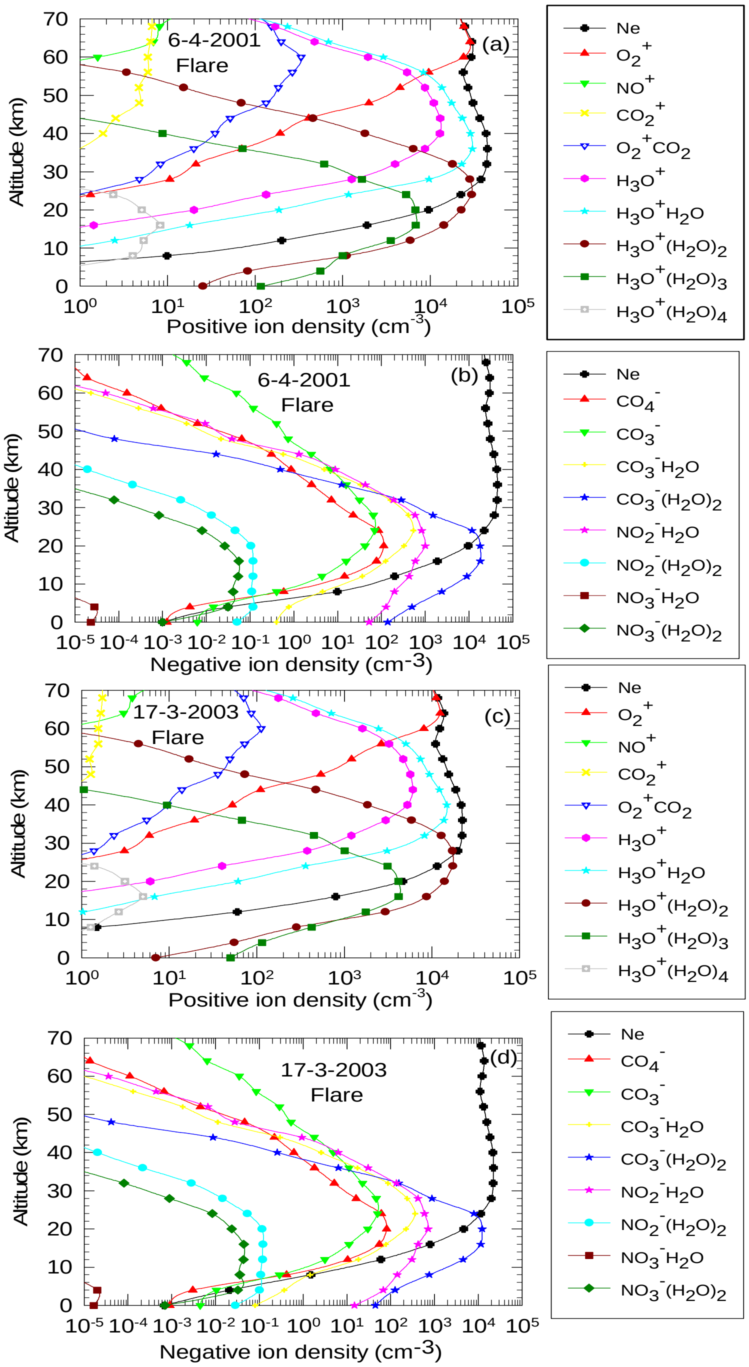

Figure 3.5. The flare induced density profiles of positive ions ($H_3O^+(H_2O)_4$, $H_3O^+(H_2O)_3$, $H_3O^+(H_2O)_2$, $H_3O^+H_2O$, H_3O^+, CO_2^+, $O_2^+CO_2$, NO^+, and O_2^+) and negative ions ($CO_3^-(H_2O)_2$, $CO_3^-H_2O$, CO_3^-, CO_4^-, $NO_2^-H_2O$, $NO_2^-(H_2O)_2$, $NO_3^-H_2O$, and $NO_3^-(H_2O)_2$) for 6 April, 2001 are shown in figures a and b respectively. The flare induced density profiles of these positive and negative ions for 17 March, 2003 are plotted in figures c and d respectively. The estimated altitude profile of electron density at flare time is also shown in Figures 3.5 a-d.

3.3.3 Non-flare profiles of ion densities in the D region of Mars' ionosphere

The figures 3.6a and 3.6b represent the non-flare profiles of positive and negative ions for 6 April, 2001. The figures 3.6c and 3.6d also represent the non-flare profiles of these positive and negative ions but for 17 March, 2003. The non-flare electron density profiles are also plotted in each figure. The non-flare electron density profiles have produced a broad peak at altitude 25 km in the lower ionosphere of Mars. We have also found three dominant ions $H_3O^+(H_2O)_2$, $CO_3^-(H_2O)_2$ and $NO_2^-H_2O$ in the non-flare ion density profiles. The ion densities of non-flare profiles are lowered by about an order of magnitude than that produced by flare profiles. The chemical scheme is taken same on both flare days in the flare and non-flare profiles of ion and electron densities. The neutral model atmospheres for 6 April, 2001 and 17 March, 2003 are taken from Millour et al. (2014) at observing location of f_{min} at college AK (64.9^{o}N, 212^{o}E). Due to lack of measurements, D layer is not observed in the lower ionosphere of Mars. In absence of these measurements we have theoretically calculated D layers on 6 April, 2001 and 17 March, 2003 when solar flares were detected by GOES 10 in soft X-rays (1-8Å) and hard X-rays bands (0.5-3Å) simultaneously (Bornmann et al., 1996). Solar flares in soft X-rays band (1-8Å) affects in the E region ionosphere of Mars. Responses of this band have been found in several electron density profiles in the E region ionosphere of Mars (Fallows et al, 2015; Thirupathaiah et al., 2019). We have also studied the effect of soft solar X-ray flares (1-8Å) in the E region ionosphere Mars. This has been described in chapter 4.

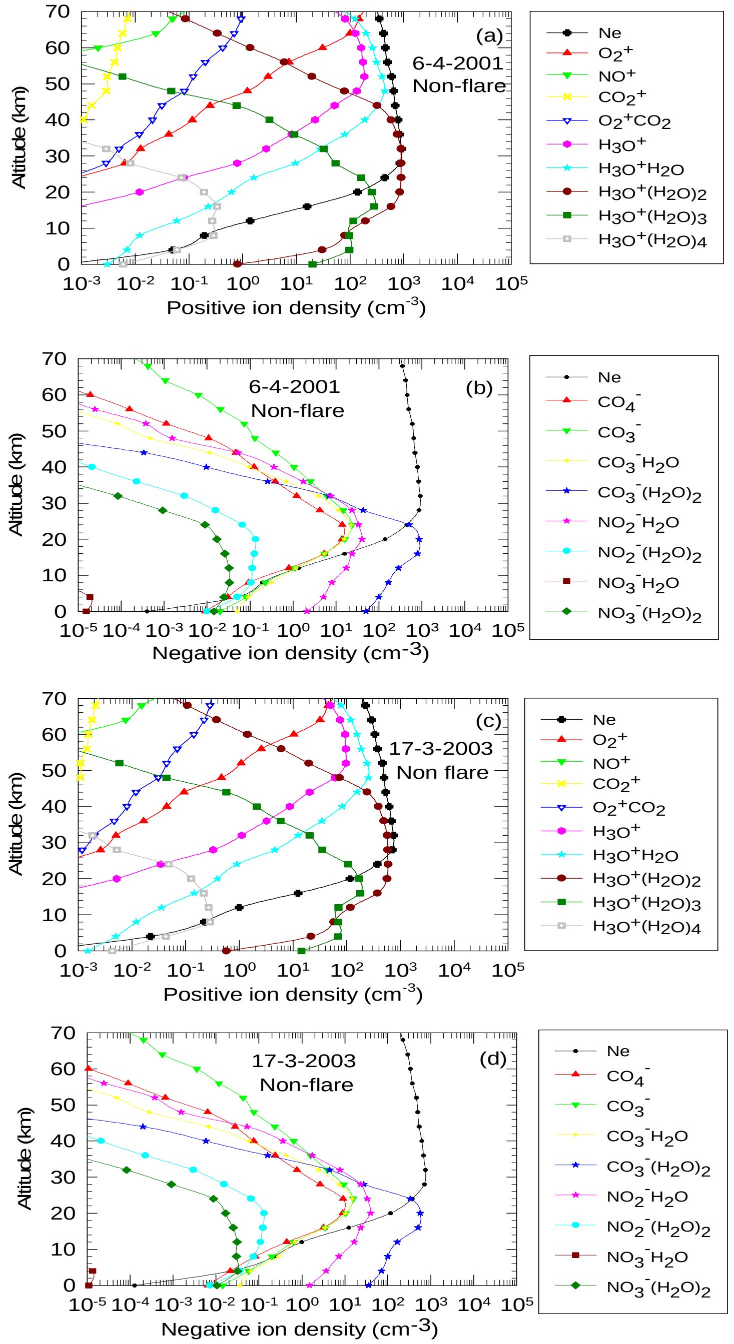

Figure 3.6. Non-flare density profiles of positive ions ($H_3O^+(H_2O)_4$, $H_3O^+(H_2O)_3$, $H_3O^+(H_2O)_2$, $H_3O^+H_2O$, H_3O^+, CO_2^+, $O_2^+CO_2$, NO^+, and O_2^+) and negative ions ($CO_3^-(H_2O)_2$, $CO_3^-H_2O$, CO_3^-, CO_4^-, $NO_2^-H_2O$, $NO_2^-(H_2O)_2$, $NO_3^-H_2O$, and $NO_3^-(H_2O)_2$) for 6 April, 2001 are plotted in figures a and b respectively. The non-flare density profiles of these positive and negative ions for 17 March, 2003 are plotted in figures c and d respectively. The non-flare electron density profiles are also plotted in figures 3.6 a-d.

3.3.4 The ion density profiles due to impact of GCR in the D region of Mars' ionosphere

We have calculated ion and electron density for 6 April, 2001 and 17 March, 2003 due to impact of GCR from 0 to 70 km in lower ionosphere of Mars. The figures 3.7a and 3.7b represent the positive and negative ion and electron densities due to impact of GCR for 6 April, 2001. The positive and negative ion densities are nearly same for 17 March, 2003 because GCR flux is not changing with location. Therefore, we have only plotted these profiles for 6 April, 2001. The electron density give a broad peak at altitude 25 km. In the chemistry of positive ions hydrated hydronium ions, $H_3O^+(H_2O)_2$ is dominant ion below 70 km. In the chemistry of negative ions, water clusters of NO_2^- and CO_3^- (i.e $NO_2^- H_2O$ and $CO_3^-(H_2O)_2$) are major below 40 km. Above this altitude electrons plays an important role in the lower ionosphere of Mars. The maximum densities of these ions are estimated ~10^3 cm^{-3} on the surface of Mars. The chemical scheme is same as described in chapter 1 without adding dust reactions. The peak value of electron density is ~1.0 x 10^2 cm^{-3} at ~25 km due to impact of GCR in the lower ionosphere of Mars. It has been found that the electron density produced by GCR is lower by about one and two order of magnitude than that produced by non-flare and flare electron density profiles.

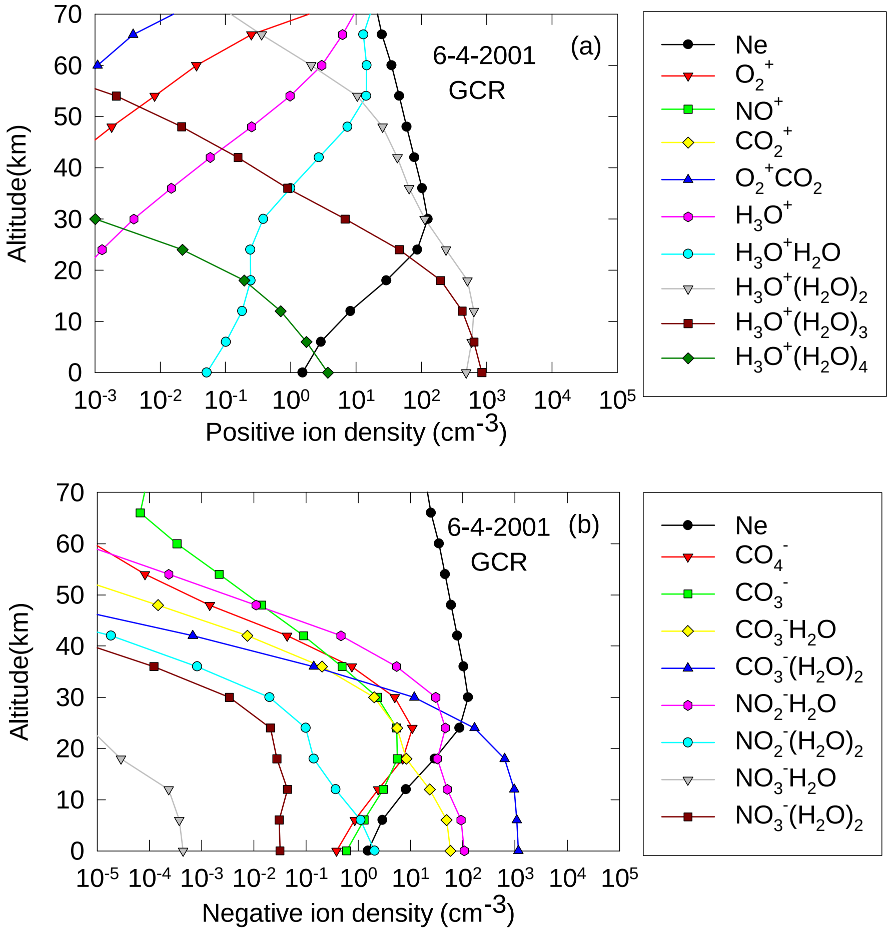

Figure 3.7. The density profiles due to impact of GCR of positive ions ($H_3O^+(H_2O)_4$, $H_3O^+(H_2O)_3$, $H_3O^+(H_2O)_2$, $H_3O^+H_2O$, H_3O^+, CO_2^+, $O_2^+CO_2$, NO^+, and O_2^+) and negative ions ($CO_3^-(H_2O)_2$, $CO_3^-H_2O$, CO_3^-, CO_4^-, $NO_2^-H_2O$, $NO_2^-(H_2O)_2$, $NO_3^-H_2O$, and $NO_3^-(H_2O)_2$) for 6 April, 2001 are shown in figures a and b respectively. The estimated altitude profile of electron density at flare time is also shown in Figures 3.7 a-b.

REFERENCES

Aikin, A. C (1968), The lower ionosphere of Mars, Icarus, **9**, 487–497.

Bornmann, P. L., Speich, D., Hirman, J., Pizzo, V. J., Grubb, R., Balch, C, et al. (1996), "GOES solar x-ray imager: overview and operational goals". Proc. SPIE 2812, GOES-8 and Beyond, (1996/10/18), **2812,** 309-319.

Davies, K. (1990), Ionospheric Radio, Peter Peregrinus, London.

Fallows, K., Withers, P., and Gonzalez, G (2015), Response of the Mars ionosphere to solar flares: Analysis of MGS radio occultation data, J. Geophys. Res., **120**, 9805-9825.

Haider, S. A., Batista, I. S., Abdu, M. A., Santos, A. M., Shah, S. Y, et al. (2016), Flare X-ray photochemistry of the E region ionosphere of Mars, J. Geophys. Res., Space Physics, **121**, 6870-6888.

Haider, S. A., Batista, I. S., Abdu, M. A., Muralikrishna, P., Shah, S. Y., and Kuroda, T (2015), Dust storm and electron density in the equatorial D region ionosphere of Mars: Comparison with Earth's ionosphere from rocket measurements in Brazil. J. Geophys. Res., **120**, 8968-8977.

Haider, S. A., Abdu, M. A., Batista, I. S., Sobral, J. H., Kallio, E., Maguire, W. C, et al.(2009a), On the responses to solar X-ray flare and coronal mass ejection in the ionosphere of Mars and Earth, Geophys. Res. Lett., **36**, 1-5.

Haider, S. A., Abdu, M. A., Batista, I. S., Sobral, J. H., Luan, X., Kallio, E, et al. (2009b), D, E, and F layers in the daytime at high-latitude terminator ionosphere of Mars: Comparison with Earth’s ionosphere using COSMIC data, J. Geophys. Res., **114**, 1-12,A03311

Haider, S. A., Sheel, V., Smith, M. D., Maguire, W. C., and Molina-Cuberos, G. J. (2010), Effect of dust storm on the D region of the Martian ionosphere: Atmospheric electricity, J. Geophys. Res., **115**, 1-10A12336.

Hargreaves, J. K (1992), The Solar Terrestrial Environment: An Introduction to Geospace-The Science of the Terrestrial Upper Atmosphere, Ionosphere and Magnetosphere, Cambridge Univ. Press, New York

Millour, E., Forget, F., Spiga, A., Navarro, T., Madeleine, J. B., Pottier, A, et al. (2014), A new Mars climate database v5.1, paper 1301 presented at The Fifth International Workshop on Mars Atmosphere: Modeling and Observations, Oxford, U. K., Jan. 2014.

Mitra, A. P. (1974), Ionospheric Effects of Solar Flares, 294 pp.,Springer, New York.

Molina-Cuberos, G. J., Lichtenegger, H., Schwingenschuh, K., López-Moreno, J. J., and Rodrigo, R (2002), Ion- neutral chemistry model of lower ionosphere of Mars. J. Geophys, Res., **105**, (3)1-(3)7.

Reinisch, B. W., Galkin, I. A., Khmyrov, G. M., Kozlov, A. V., Bibl, K., Lisysyan, I. A (2009), New Digisonde for research and monitoring application, Radio Sci., **44**, 1-15, RSOA24.

Schunk, R., and Nagy, A.(2000), Ionospheres: Physics, Plasma Physics and Chemistry, Cambridge Univ. Press, New York.

Siddhi Y. S, Haider,S. A., Molina-Cuberos, G. J,, Abdu, M. A., Batista, I (2019), A coupled model of the D and E regions of Mars' ionosphere for flare and non-flare electron density profiles: Comparison with Earth's ionosphere, Icarus. (Under review).

Thirupathaiah, P., Shah, S. Y., and Haider, S. A. (2019), Characteristics of solar X-ray flares and their effects on the ionosphere and human exploration to Mars: MGS radio science observations, Icarus, **330**, 60-74.

Whitten, R.C., Poppoff, I. G., and Sims, J. S (1971), The ionosphere of Mars below 80 km altitude-I, Planet. Space Sci., **19**, 243–250.

❒❒❒

CHAPTER - 4

PHOTOCHEMISTRY OF E REGION IONOSPHERE OF MARS

CONTENTS

The solar X-ray flare response is a key problem in the planetary ionospheres. The MGS observed the responses of 32 solar X-ray flares in the E-region electron density profiles during its lifespan. We have estimated IEC from these measured profiles. Among these measurements we have modeled only two electron density flare profiles that were observed on 6 April 2001 and 17 March 2003. The modeled results are greater than the measurements by a factor of ~ 2-3 at the flare time. Seasonal variations of 32 electron production rates in the E region ionosphere of Mars are also estimated in presence of solar X-ray flares. We have also calculated the biological doses for X, M, C class flares to study the human risk for exploration to Mars.

4.1 INTRODUCTION

Radio occultation experiment has been found very useful for the measurements of Mars' ionosphere. It is a remote sensing experiment. The radio science experiment on board MGS has observed 5600 electron density profiles during 24 December, 1998 to 9 June, 2005 (Withers et al., 2008). This experiment was also aboard on Mars Express (MEX) and has observed 500 electron density profiles (Haider and Mahajan, 2014). These profiles show E and F peaks at altitudes ~115 km and 135 km due to impact of X-rays (10-90 Å) and solar EUV (90-1025 Å) radiations respectively. The MARSIS experiment also measured an increase in the peak electron density of about 30% during a solar flare, which returned to the pre-flare level within a few minutes (Nielsen et al., 2006). The response of this flare in the F region was smaller than that observed in the E region. Therefore it was not detected by radio occultation observations.

In this Chapter we have studied 32 flare profiles of electron densities that were observed by radio science experiment onboard MGS during solar cycle 23. Out of 32 profiles recorded during flare periods, 10 were associated with X-class flares, 12 with M class, and 10 with C class. Their E-peak flare densities vary with solar X-ray flux, SZA, Solar Longitude (Ls), Universal Time (UT), and latitude. We have examined the E-peak electron density dependence of 32 flare profiles with these parameters. Percentage increase in IEC and E-peak electron production rates of these flare profiles are estimated in the E region ionosphere of Mars. We have also studied the implications of solar X-ray flares on the habitability of all kinds of bio-organisms. The biological doses of 32 flares are estimated using GOES X-ray fluxes. The characteristics of X, M and C class flares, their affects on electron density profiles and biological doses are given in Table 1 (Fallows et al., 2015). Although 32 profiles are limited to study the correlations of flare E-peak densities on Ls, SZA, latitudes and solar X-ray fluxes, the limitation of datasets do not bias the results. Our results are able to investigate the flare electron density dependence quantitatively on these parameters. However, additional observations would greatly improve the accuracy of the flare dependence on these parameters.

Table 4.1: Characteristics of solar X-ray flares on Mars' ionosphere

#	Date	Class[a]	Location[a] (Sun Disc)	Start Time[a] (UT)	Peak Time[a] (UT)	End Time[a] (UT)	Flare Profile Time (UT)	Total Profile #	SZA (deg)	ESM (deg)	Dose (Gray*)
X-Class Flares											
1	24/11/2000[c]	X1.8	N21E06	21:43	21:59	22:12	22:03	10	83.9	103.2	1.50E-02
2	25/11/2000[e]	X1.9	N21W08	18:33	18:44	18:55	19:37	12	83.8	102.7	1.60E-02
3	02/04/2001[e]	X1.1	N16W56	10:58	11:36	12:05	12:12	7	71.8	32.2	9.83E-03
4	06/04/2001[e]	X5.6	S21E47	19:10	19:21	19:31	20:13	11	72.0	30.2	4.74E-02
5	10/04/2001[c]	X2.3	S22W07	05:06	05:26	05:42	06:39	7	72.1	28.3	1.93E-02
6	15/04/2001[b,c]	X14.4	S22W72	13:19	13:50	13:55	14:14	6	72.5	25.9	9.92E-02
7	17/03/2003[e]	X1.5	S14W26	18:50	19:05	19:16	19:38	7	71.0	62.2	1.34E-02
8	18/03/2003[e]	X1.5	S16W39	11:51	12:08	12:20	13:17	7	71.0	61.7	1.25E-02
9	29/05/2003[c,d]	X1.2	S07W32	00:51	01:05	01:12	01:38	10	78.4	31.2	8.95E-03
10	17/01/2005[d]	X3.8	N13W15	06:59	09:52	10:07	11:36	8	74.6	113.6	3.64E-02
M-Class Flares											
11	21/11/2000[e]	M1.6	N09W46	19:13	19:21	19:27	19:31	8	84.3	104.9	1.26E-03
12	20/01/2001[e]	M7.7	S07E57	21:06	21:20	21:32	21:16	8	76.6	70.5	6.52E-03
13	28/03/2001[e]	M4.3	N17E11	11:21	12:40	13:06	12:28	9	71.8	34.6	3.74E-03
14	26/04/2001[e]	M7.8	N16W15	11:26	13:12	13:19	13:15	5	73.6	20.8	6.37E-03
15	21/04/2003[e]	M2.8	N18E09	12:54	13:07	13:14	13:17	11	73.0	46.3	2.46E-03
16	31/05/2003[c,d]	M9.3	S07W59	02:13	02:24	02:40	02:40	8	78.8	30.4	7.57E-03
17	29/12/2004[e]	M2.3	N04E74	15:57	16:27	16:38	16:15	8	76.4	123.5	1.95E-03
18	30/12/2004[e]	M4.2	N04E61	22:02	22:18	22:28	23:39	13	76.2	123.0	3.20E-03
19	09/01/2005[e]	M2.4	S09E82	8:25	08:51	09:09	09:20	9	75.2	117.7	2.01E-03
20	23/01/2005[e]	M1.0	N11W93	01:28	01:51	02:01	03:00	10	74.2	110.5	9.48E-04
21	19/02/2005[e]	M3.3	S09W32	10:36	11:01	11:13	12:24	7	73.2	97.2	3.02E-03
22	13/05/2005[c,d]	M8.0	N12E19	16:13	16:57	17:28	18:07	10	82.7	62.8	7.43E-03
C-Class Flares											
23	07/11/2000[e]	C2.2	N03W50	16:24	16:28	16:34	18:09	6	85.9	112.9	1.63E-04
24	17/11/2000[e]	C2.3	N14E63	10:54	11:07	11:38	11:33	11	84.8	107.2	2.09E-04
25	13/12/2000[e]	C5.8	N08E25	21:55	22:04	22:16	21:06	11	81.6	92.3	4.57E-04
26	19/12/2000[e]	C9.5	N08W57	10:03	10:24	10:28	10:30	10	80.8	88.8	5.94E-04
27	07/04/2001[e]	C2.0	S08E14	09:15	09:35	09:48	08:00	5	72.0	29.7	1.77E-04
28	18/04/2001[e]	C2.2	S20W120	02:11	02:14	02:16	03:05	7	72.7	24.5	1.05E-04
29	13/05/2001[e]	C1.6	S16E03	20:47	20:52	21:02	21:23	12	76.9	13.2	1.18E-04
30	25/05/2001[e]	C5.2	N05E25	19:12	19:37	19:57	19:59	7	80.9	8.1	4.59E-04
31	01/01/2005[e]	C1.2	N04E34	14:08	14:24	14:32	14:54	8	76.0	121.9	1.06E-04
32	17/04/2005[e]	C4.6	N02E14	20:46	21:07	21:15	21:59	12	77.8	72.5	2.32E-04

*1 Gray = 10^4 erg / gm, [a]https://www.spaceweatherlive.com, [b]Published in Mendilo et al. (2006),[c]Published in Mahajan et al. (2009), [d]Published in Haider et al. (2012), [e]Publishedin Fallows et al. (2015).

4.1.1 Effects of solar X-ray flares in the E region ionosphere of Mars

The E region of Mars' ionosphere is produced at altitude range 90-120 km by X-rays (10-100Å) (Fox, 2004; Haider et al., 2009a, 2016). In normal condition the peak electron density ~ 2 to 4 x 10^4 cm^{-3} is observed in the E region of Mars' ionosphere (Schunk and Nagy, 2000). Martinis et al. (2003) and Fox (2004) estimated E layer in the Martian ionosphere due to absorption of soft X-rays in the wavelength range of 18 to 50 Å. The responses of solar X-ray flares in the Martian ionosphere were first reported by Gurnett et al. (2005) from MARSIS observations. Mendillo et al. (2006) showed that the E layer of Mars' ionosphere is formed due to impact of X-rays between wavelength 10 Å and 50 Å. Haider et al. (2009a) identified ~150% increase in the E-region electron density due to X-ray flare of 13 May, 2005. They confirmed about the arrival of CMEs in the E region of Mars' ionosphere after ~38 hours from the explosion of this flare.

The ionospheric responses to five flares on 24 November, 2000, 2 and 10 April, 2001, 29 and 31 May, 2003 were studied by Mahajan et al. (2009). They found a well-defined E-peak during the flare period. Lollo et al. (2012) modelled the electron density profiles of 15 and 26 April, 2001. They found that the E-peak density can exceed from the F-peak during the intense solar X-ray flares. Haider et al. (2012) investigated ionospheric responses to solar X-ray flares and CME during periods 29 May to 3 June 2003, 15-20 January 2005 and 12-18 May 2005. They modelled a large increase by a factor of 4-8 in the E region ionosphere at the flare time. They have also investigated the effect of CMEs in the E region ionosphere, which enhanced electron density by a factor of ~ 2 during 30-31 May 2003, 2-3 June 2003 and 16-17 May 2005. Recently, Fallows et al. (2015) developed a response function, which confirmed the findings of earlier investigators on the ionospheric responses to solar X-ray flares.

4.1.2 MGS measurements of flare electron density Profiles

The MGS radio occultation experiments measured 5600 electron density profiles during 683 days. MGS dataset is the largest and has highest cadence observations during solar maximum condition. The mission flew through an active solar maximum, which peaked in 2001 (Gopalswamy et al., 2012). It is therefore the best suited for the studies of a transient and short-term phenomena such as solar flares. Within a 2 h cadence period, the effect of a solar flare is likely to be visible in only a single profile. However, several additional profiles from within a few hours of the affected profile are available to characterize the baseline ionospheric conditions. We have plotted 85, 106 and 89 electron density profiles that were observed by MGS with an apparent solar flare responses of 10-X class flares (figure 4.1 (a_1-a_{10})), 12 M class flares (figure 4.2 (b_1-b_{12})) and 10-C class flares (figure 4.3 (c_1-c_{10})) respectively (Table 1). The flare profiles are plotted by red line. The non-flare profiles are plotted by different colours. The E and F peaks are observed at ~112 km and ~ 140 km are due to absorptions of solar X-rays and EUV radiations respectively (Bougher et al., 2001; Haider et al., 2009a). The E layer does not always show a clear peak in the electron density profiles of MGS. The MGS observations were made between local times 2 to 14 hour at high latitudes (63^{o}N-85^{o}N) and high SZA (71^o-86^o) during the flare period. MGS did not measure the electron densities for all flare events that occurred in the entire Martian year.

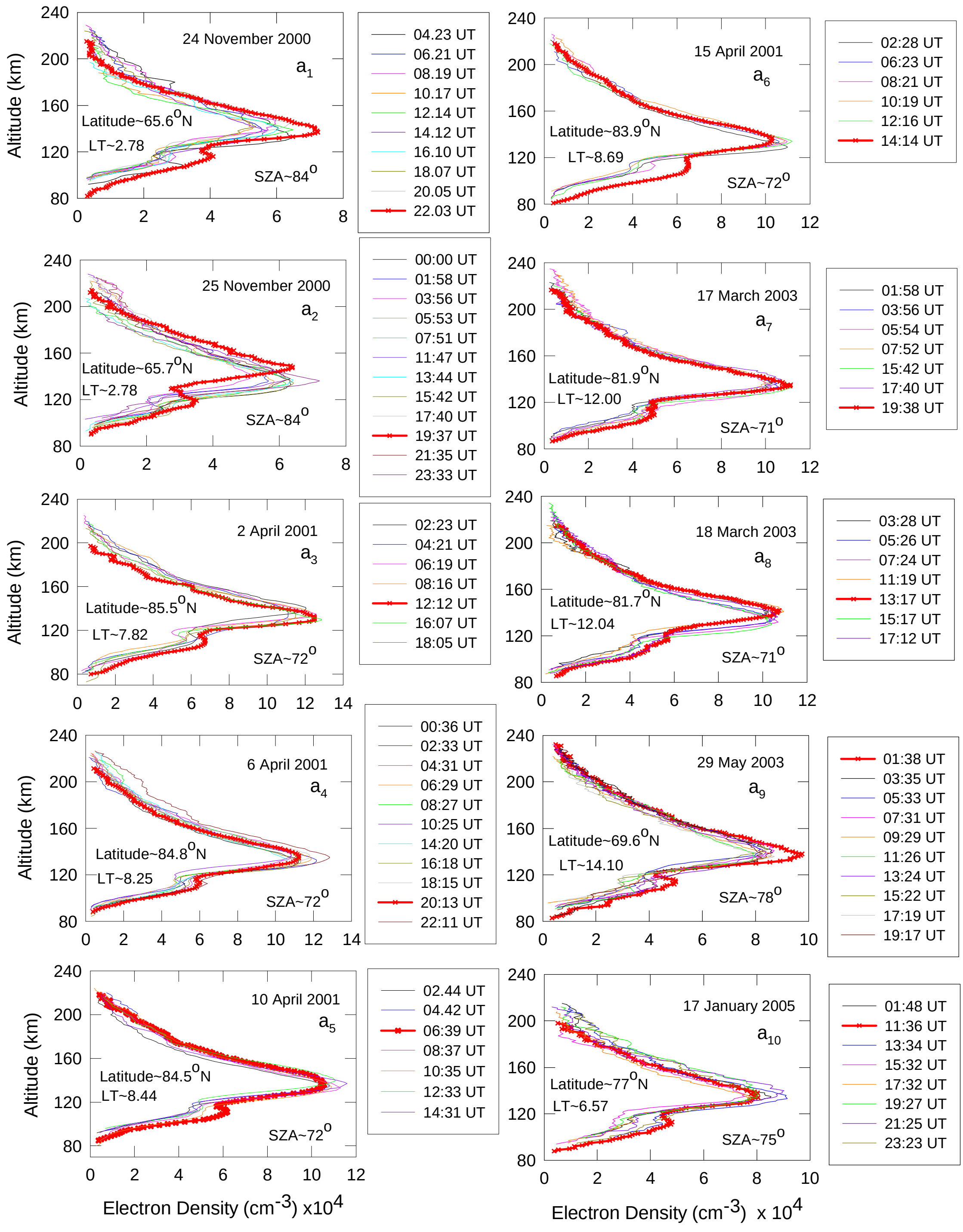

Figure 4.1 10 X-class (a_1-a_{10}) flare electron density profiles observed by MGS on 10 respective flare days. The flare profiles are plotted by red lines with cross symbol. Latitude, LT and SZA refer to the flare time profile only.

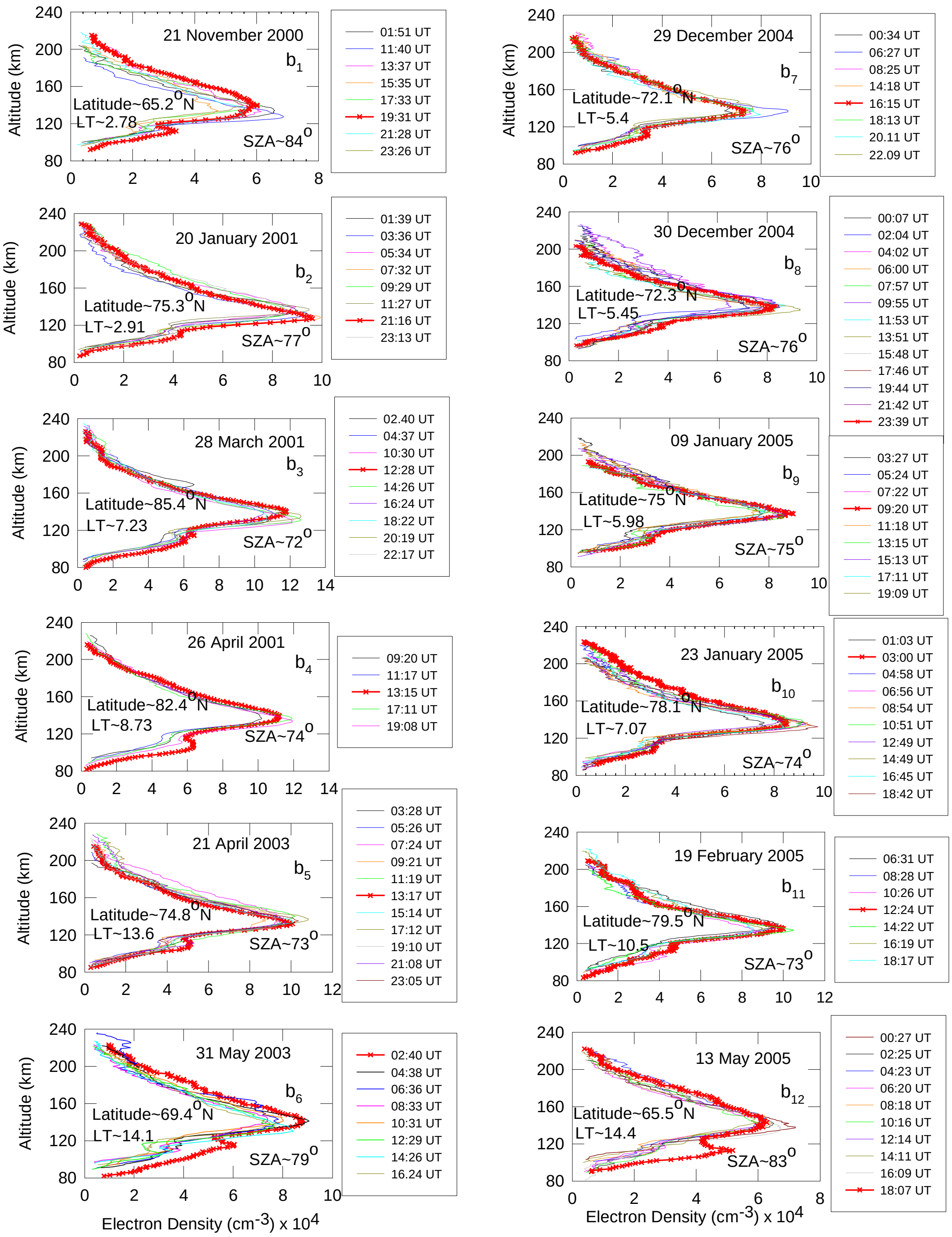

Figure 4.2 Same as in figure 4.1 but for M-class (b_1-b_{12}) flare electron density profiles observed by MGS.

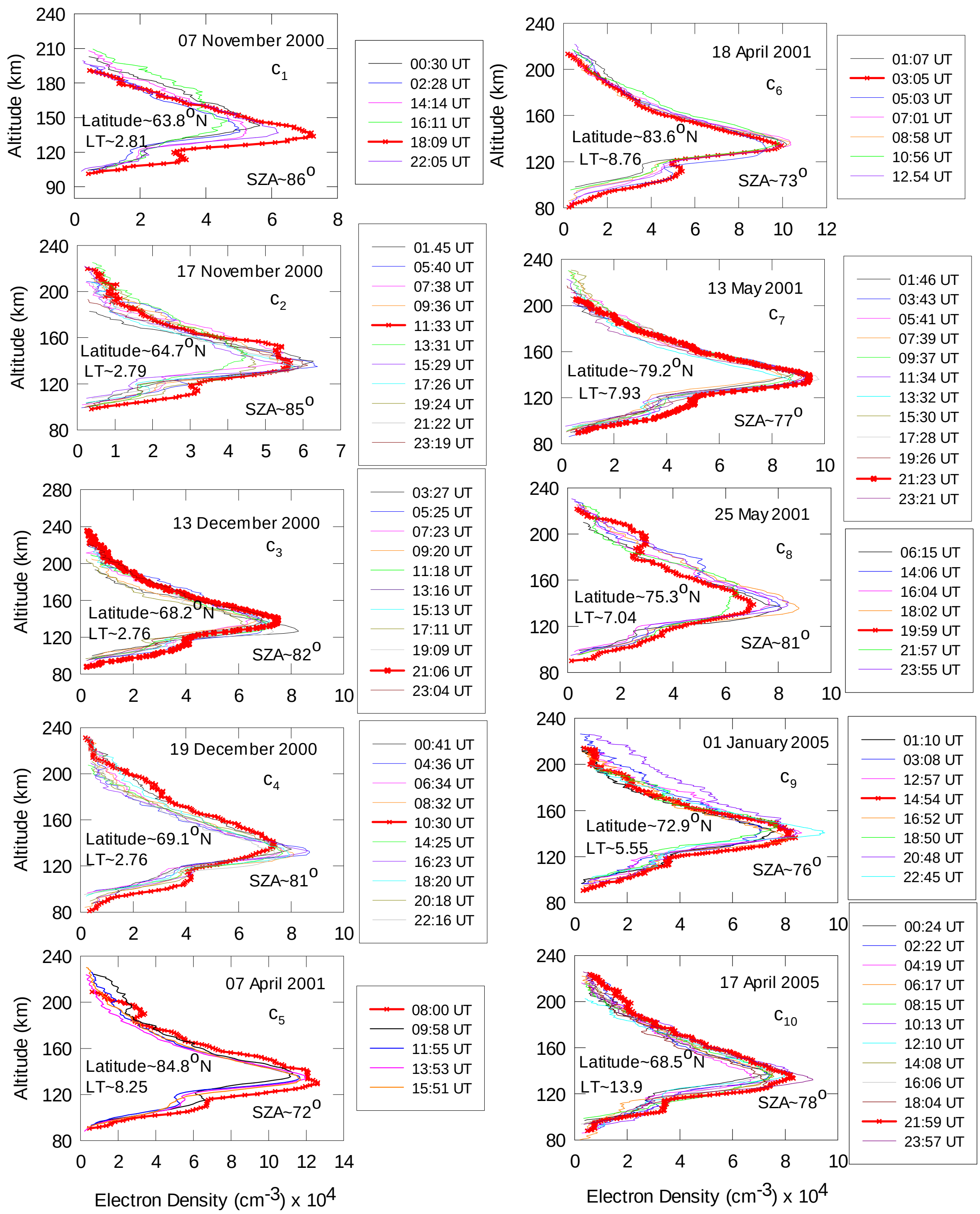

Figure 4.3 Same as in figure 4.1 but for C-class (c_1-c_{10}) flare electron density profiles observed by MGS.

It should be noted that 20 solar X-ray flares are reaching on Mars at ESM angles between 8.1° and 97.2°. The remaining 12 solar flares were arrived on Mars at ESM angles between 102.7° and 123.5°. Therefore, these flares faced Earth and Mars nearly in the same side and were visible at Mars. In figure 4.2a_4, the value of E peak at 22:11 UT is larger at altitude ~ 113 km by ~ 6% than the peak flare profile at 20:13 UT. This enhancement in the E layer may be related to post-flare effect, which was observed during ~ 3 hours cadence period (Tsurutani et al., 2005; Haider et al., 2016). It should be noted that responses of solar flares in 32 electron density profiles were observed by MGS within 2-3 hour cadence period after the flare peak (see figures 4.1 (a_1-a_{10}), 4.2 (b_1-b_{12}), 4.3 (c_1-c_{10}) and figure 4.5).

4.1.3 Dependence of peak electron density on Solar X-ray flux and SZA

We have studied the correlation between the measured E peak electron density and GOES solar X-ray flux. Under the photochemical equilibrium condition (production= loss) the electrical neutrality is required as q = α [N_e] [O_2^+], where q is production rate, [O_2^+] is the density of major ion (Fox, 2004; Haider et al., 2009a) and α is the dissociative recombination coefficient. Since the density of O_2^+ is nearly equal to the electron density, we can consider [N_e] = [O_2^+], then q = α N_e^2. The q is directly proportional to solar ionizing flux F. Then F is also proportional to N_e^2. We have studied this relationship in figure 4.4a, 4.4b, and 4.4c. This figure represent the dependence of$\log_{10}$ (N_f/N_0) as a function of $\log_{10}$ (F_f/F_0) at E layer peak altitudes. The subscripts f and 0 represent instantaneous flare time and pre-flare values. This figure was plotted by using 10, 12 and 10 sample data points for X, M and C class flares respectively. We have plotted these data points with standard deviation. These data points are fitted by linear regression formula Y = mX, where Y = $\log_{10} (N_f/N_0)$, X = $\log_{10} (F_f/F_0)$ and m is a fitting constant. The values of m are nearly equal to 0.11 ± 0.01, 0.09 ± 0.01 and 0.26 ± 0.02 for X, M and C class flares respectively. The values of b are nearly equal to -0.035 ± 0.02, 0.032 ± 0.01 and 0.025 ± 0.015 for X, M and C class flares respectively. Although we have a limited sample data points but a positive correlation is found between the instantaneous flare time increase in electron density and ionizing peak X-ray flux. The best fit value of m increases with decreasing the intensity of X-ray radiations from X-to C-class flares. In figure 4.4 (a-c) the electron densities are also influenced by SZA. The peak electron density enhancements in the flare profiles are generally greater at larger SZA. It should be noted that the small changes in GOES X-ray fluxes are producing large changes in the E region electron density.

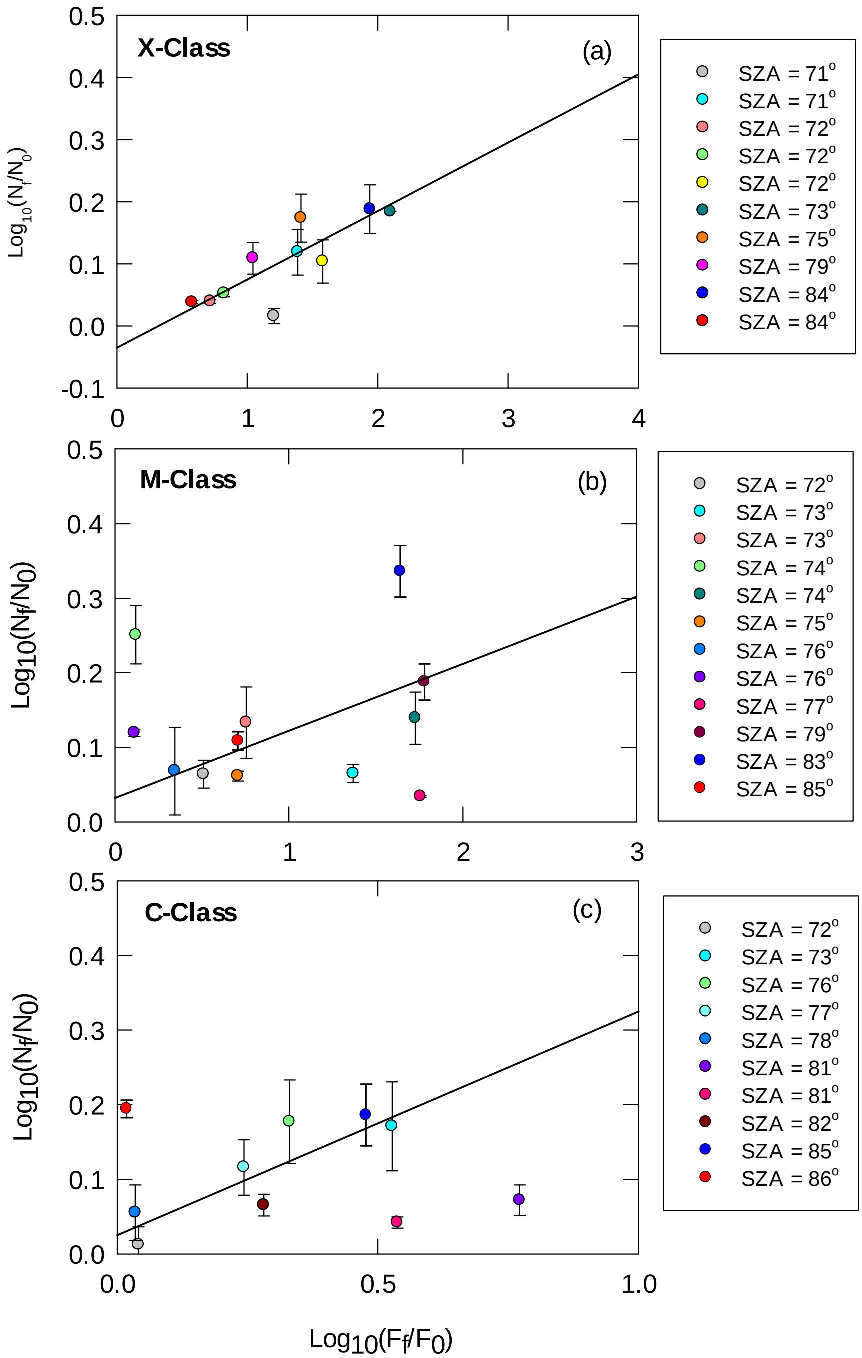

Figure 4.4 Relationship between $\log_{10}$ (N_f/N_o) and $\log_{10}$ (F_f/F_o) with standard deviation for 10 X-class (a), 12 M-class (b) and 10 C class (c) flares. SZA are shown by different colors for different flare profiles. The solid lines are fitted by linear regression for 10 X-class, 12 M-class and 10 C-class flares.

4.2 CHARACTERISTICS OF E REGION MARS' IONOSPHERE DURING SOLAR FLARES

In this section we have studied variations of IEC of 32 electron density profiles with UT. The flare profiles are integrated from lower height to E-F valley altitudes to obtain the IEC in the E region ionosphere. The seasonal variations of E-peak electron production rates are also calculated for 32 flare profiles. The dependence of peak electron density with solar X-ray flux at different SZA is shown in figures 4.4 (a-c) in section 4.1.3. The strong solar flares affect all kind of life from human to microbial. Therefore we have also calculated biological doses ~ 0.1 - 1.0 x 10^{-1}, 1 - 8 x 10^{-3} and 1-6 x10^{-4} Gy for X, M, C class flares respectively to study the human risk for exploration to Mars. Among 10 X-class flares X14.4 is a strong solar flare that gives highest dose, which is potentially lethal for humans (see Table 1). The latitude dependence of peak electron density is not significant therefore it is not plotted. We report that 32 flare profiles are not enough to explain dependence of peak electron densities clearly on SZA, latitude, longitude, UT, LT, and Ls. Additional observations can improve the accuracy of the flare dependence on these parameters.

4.2.1 Variation of IEC with UT

In the left panels of figure 4.5 (a-c) we represent time variation of percentage increases in the measured IEC of 10 flares of X-type, 12 flares of M-type, and 10 flares of C-type, respectively. The time variation of percentage increases in 32 solar X-ray fluxes of X, M and C class flares are also shown in the right panels of figure 4.5 (d-f) respectively. As shown in figures 4.1 (a_1-a_{10}), 4.2 (b_1-b_{12}) and 4.3 (c_1-c_{10}), the ionosphere of Mars was calm before the solar flares. The ionosphere significantly perturbed during the flare time (see figures 4.1-4.3 by red lines). In figure 4.5 (d-f) the percentage increases in the X-ray flux are maximum on 15 April, 2001, 31 May, 2003, and 19 December, 2000 for X14.4, M9.3 and C9.5 types of solar X-ray flares. We have found maximum enhancements of ~200%, ~140%and ~ 90% in the time series of IEC for X, M and C class flares respectively.

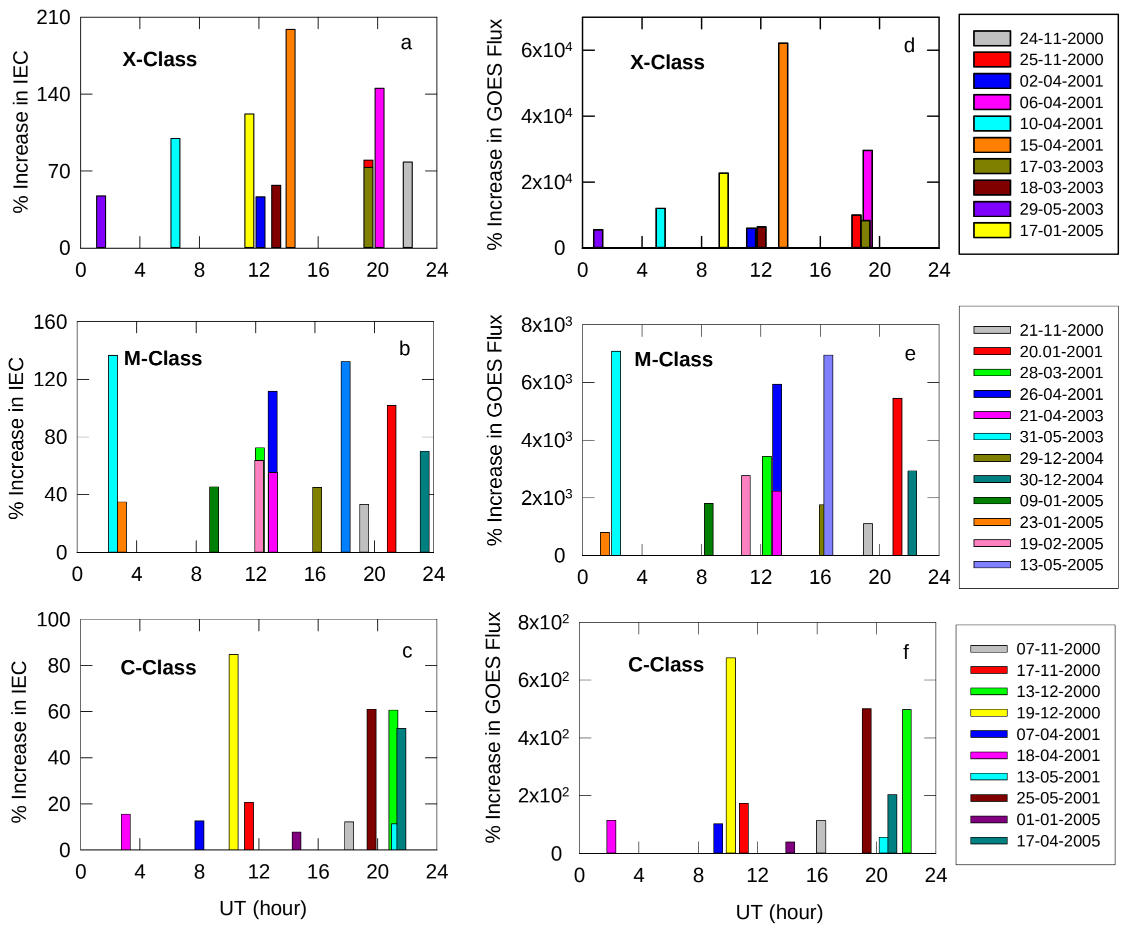

Figure 4.5. Left panel: The % increase in IEC at different UT for 10 X-class (a), 12 M-class (b) and 10 C-class (c) flare profiles as observed by MGS. Right panel: The % increase in corresponding solar X-ray fluxes at different UT for 10 X-class (d), 12 M-class (e) and 10 C-class (f) flares as observed by GOES 10 at peak flare time.

It should be noted that the decay time of the flare is more than the rise time of the flare. It can be seen in the time series of the GOES spectra of 32 flares (not shown here). Therefore, the effects of X-ray flares are continued for a longer time up to ~ 2 hours or some times more in the E region ionosphere. The electron densities are not measured at the peak flare time. In figures 4.1 (a_1-a_{10}), 4.2 (b_1-b_{12}) and 4.3 (c_1-c_{10}), the measurements of electron densities are shown only during the decay phase of the flares. In comparing between figure 4.5 (a-c) and figure 4.5 (d-f) we have found a direct co-relation in percentage increase of GOES X-ray flux and IEC for X, M and C class flares.

4.2.2 Dependence of E peak production with Season

The peak electron production rates are calculated in the E region ionosphere of Mars due to effects of 10 X-class flares, 12 M-class flares and 10 C-class flares using the formula $q = \alpha N_e^2$ under the photo chemical equilibrium condition. The rate coefficient $\alpha = 1.67 \times 10^{-7} (T_e/300)^{-0.5}$ is taken from Torr and Torr (1979). The values of electron temperature (T_e) is equal to neutral temperature (T_n) below ~ 120 km, therefore we have taken $T_e = T_n$ from MCD (Martian year scenario) (Millour et al., 2014). In Figures 4.6a, 4.6b, and 4.6c we have fitted seasonal variations of X, M and C class flare E-peak electron production rates (P) by sinusoidal function respectively. The standard deviation and 0.95 % confidence limits **(**Haider et al. 2011**)**, for X, M and C class flares are also plotted in these figures. The P is fitted using the following equation:

$$P = P_0 + A\sin[B(L_s - C)] \tag{4.1}$$

where Ls varies between 70^o to 210^o, P_o is a vertical shift = $\frac{(P_{max} + P_{min})}{2}$, C is a horizontal shift = $\frac{(L_{max} + L_{min})}{2}$, A is amplitude, and B is a radian frequency = $\frac{\pi}{(L_{max} - L_{min})}$. The flare E-peak electron production rates are highly fluctuated for X-ray flares of types X14.4, M9.9 and C9.5 on 15 April, 2001, 31 May, 2003 and 19 December, 2000 at LT = 08:40, 14:05 and 02:45 respectively (The flare profiles X14.4, M9.9 and C9.5 are plotted in figures 4.1a_6, 4.2b_6 and 4.3c_4 respectively). It can be noticed that the distributions of flare E-peak electron production rates are not fully symmetric with seasons because seasonal coverage of MGS occultation is very limited. The Ls are normally distributed ranging from northern late spring (Ls = 70.3^o) to mid-fall (Ls = 225.8^o) with a median at Ls = 139.6^o. The flare E-peak electron production rates are maximum during the peak summer (Ls ≈ 150^o). The figure 4.6d shows the heliocentric distance of Mars as a function of Ls. In northern hemisphere Ls = 0^o-90^o, 90^o-180^o, 180^o-270^o and 270^o-360^o represent spring, summer, autumn and winter seasons respectively. The seasons of southern hemisphere are always opposite to northern hemisphere. The MGS observed the electron density profiles in northern hemisphere during solar cycle 23. The responses of solar X-ray flares were observed in limited electron density profiles at large heliocentric distance during late spring, summer and autumn seasons (Ls = 73^o to 210^o). Therefore, we have plotted E-peak electron production rates between Ls = 70^o to 270^o in figure 4.6 (a-c).

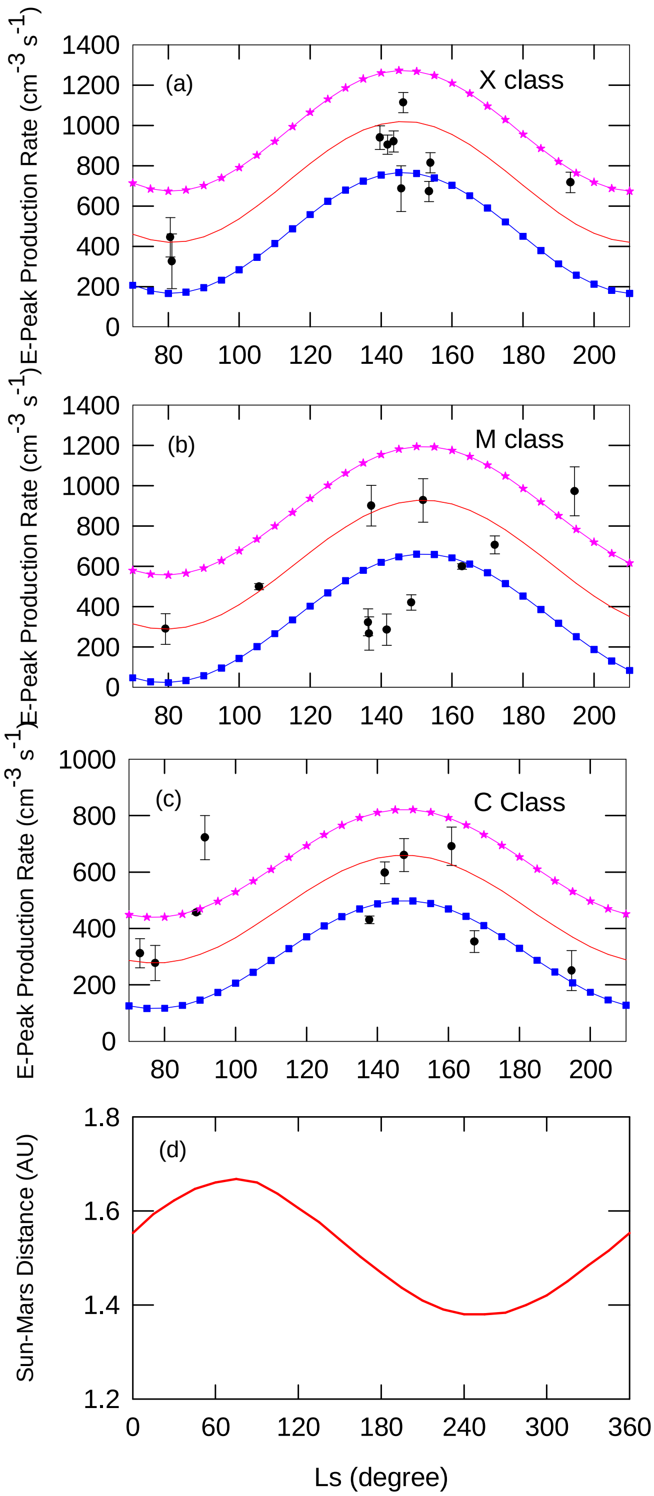

Figure 4.6 Variation of peak electron production rates with Ls for 10 X-class (a), 12 M-class (b) and 10 C-class (c) flare profiles as given in Table 1. These are fitted by sinusoidal function with standard deviation. Figure 4.6(d) shows the heliocentric distance of Mars as a function of Ls.

4.2.3 Calculation of biological dose of X-ray flares

We have calculated the biological dose (D) of 32 flares between 0 km and 125 km using the following expression:

$$D = \sum_{E_{\min}}^{E_{\max}} I_o \left(E\right) e^{-\tau} \, W\left(E\right) \delta E \qquad (4.2)$$

where E is the energy of X-ray radiation (1-8Å ≈ 1-12 keV), I_o is the X-ray flux of energy E at the top of the Martian atmosphere, τ is the optical depth, W(E) is the X-ray attenuation absorbed by the body at energy E and δE is the energy bin of X-rays radiation. The I_o (E) is obtained at flare peak by multiplying GOES 1-8 Å flux with scaling factor $(R_e/R_m)^2$, where R_e (~1.0 AU) and R_m are the orbital radii of Earth and Mars respectively. The values of R_m are taken from the observations of MGS for the respective flares**.** The optical depth is calculated between 0 km and 125 km (e.g. we have estimated $\tau = 10^4$ at 0 km, $\tau = 1.0$ at 100 km and $\tau = 0.0$ at 125 km) using radiative transfer method by considering absorption cross section for 1-8 Å radiation (cf. Petrova et al., 2012). The values of W(E) are taken from the National Institute of Standards and Technology Database (http://www.nist.gov/pml/data/xraycoef/). In Table 1 the biological doses are estimated from~ 0.1 to 1.0 x 10^{-2}, 1 to 8 x 10^{-3} and 1 to 6 x 10^{-4} Gy between 10 X class, 12 M class and 10 C class flares respectively. Among 10 X-class flares X14.4 is a strong solar flare that gives highest dose, which is potentially lethal for human risk in Mars' space.The biological dose is maximum at about 100 km. It is insignificant below 50 km. The effects of these flares are harmless at the surface of Mars because biological dose is zero there.

4.3 ELECTRON DENSITY ENHANCEMENT DURING SOLAR FLARES

The altitude profiles for the densities of six ions (CO_2^+, N_2^+, O_2^+, O^+, CO^+, and NO^+) and electron are calculated between 80 km and 200 km when two strong flares of X class: X5.6 and X1.5 impacted in the E region of Mars' ionosphere on 6 April, 2001 and 17 March, 2003 at 20:13 UT and 19:38 UT respectively. The effects of these flares have been observed by MGS in the electron density profiles shown in figures 4.1a_4 and 4.1a_7. In this calculation the photoionization and photoelectron impact ionization rates of CO_2^+, N_2^+, O_2^+, O^+, and CO^+ are calculated from two dimensional AYS model using equation (2.13). The production rate of NO^+ is not calculated from this method because direct ionization of NO has little effect on the density profile of NO^+ (Fox, 2004). We have taken neutral density of five gases CO_2, N_2, O_2, O, and CO from MCD model (Millour et al., 2014). The neutral density of NO is not given by this model. We have taken neutral density of NO from Fox (1993). It is assumed that density of NO is not changing significantly with locations. The chemistry of this model is described in Chapter 1 (see figure 1.3). The neutral temperature necessary to calculate the ion and electron densities are taken from the MCD model (Millour et al., 2014). The electron temperature is taken from Fox (2009). In this Chapter ion and electron density are calculated under steady state photochemical equilibrium condition using equation 2.6. This assumption is valid up to 200 km where chemical time is very large than the transport time (Haider et al., 2009b). These calculations are carried out at the same locations where MGS observed the flare profiles on 6 April, 2001 and 17 March, 2003 at 20:13 UT and 19:38 UT respectively

4.3.1 Modeling of flare electron density profiles observed by MGS

In figures 4.7a and 4.7b we have compared model results and observations of flare induced electron density profiles for 6 April, 2001 and 17 March, 2003 respectively. The MGS observed the complete electron density profiles in the E and F regions of Mars' ionosphere simultaneously at peak altitudes 100 km and 135 km respectively (Hinson et al., 1999; Patzold et al., 2005; Bougher et al., 2001). We have calculated electron density profiles in the E region ionosphere of Mars only due to impact of solar X-ray fluxes in wavelength range 1-8 Å. The E flare peak values are estimated to be ~ 2 x 10^5 cm^{-3} and 1.2 x 10^5 cm^{-3} on 6 April 2001 and 17 March 2003 respectively. The electron density profile in the F region is produced due to impact of solar EUV fluxes in the wavelength range ~100-1025 Å (Haider et al., 2009). Since the MGS cannot observe E region electron density profiles alone, we have compared our model results of two flare days with the corresponding complete flare profiles of MGS observations. In the vicinity of ionization peak, our model results are larger by a factor of ~ 2-3 than the measurements. This may be due to two main reasons: (1) we have used elastic cross sections of porter and Jump (1978) in our model calculation. These cross sections are smaller by a factor of 2 than the recent measurements of Itikawa (2002) and Buckman et al. (2002). Due to use of low elastic cross sections the peak electron density can increase by a factor of 2, and (2) we have neglected electron-ambient electron collisions in our calculation. In absence of electron-ambient electron collisions the peak electron density can increase. One can approximately incorporate this correction by adding term n_e (z) $\sigma_{e\text{-}e}^{eff}(E)$ in the summation appearing in the denominator of equation (2.22). Here $n_e(z)$ is the electron density and $\sigma_{e\text{-}e}^{eff}(E)$ is the effective electron-ambient-electron collision cross section (Bhardwaj et al., 1990).

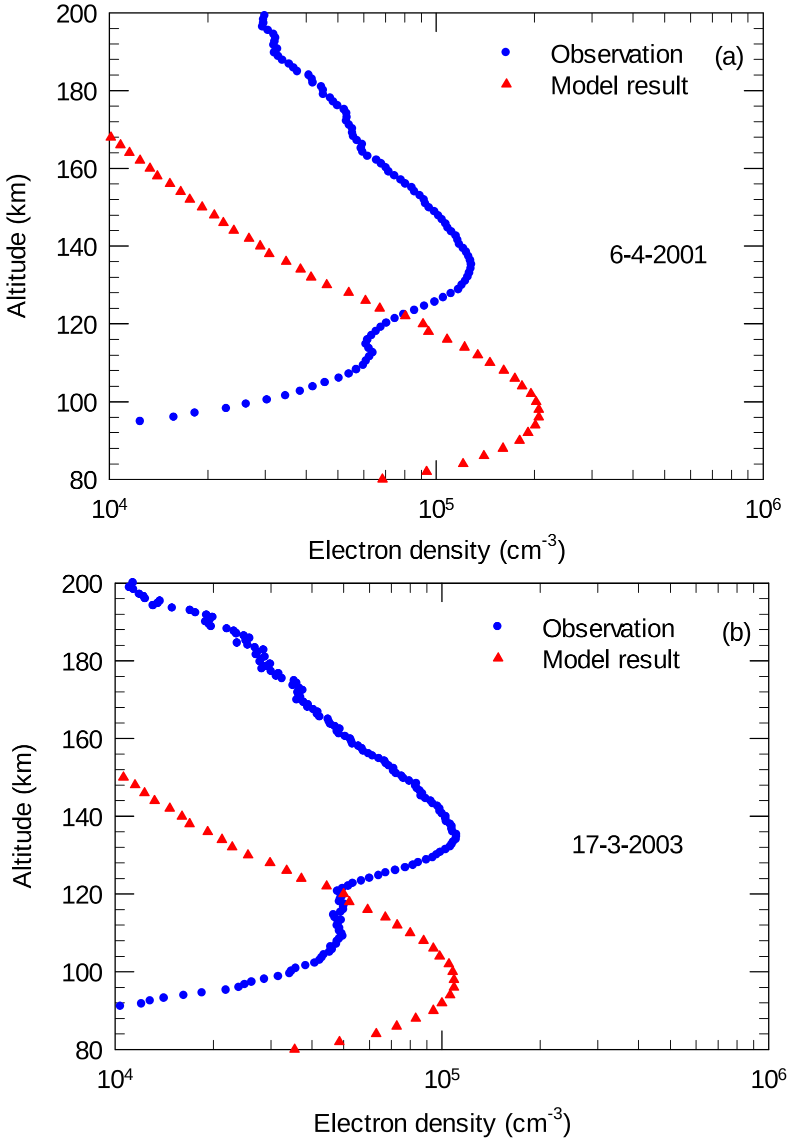

Figure 4.7 (a) Comparison between the modeled and observed electron density profiles on 6 April, 2001 and (b) 17 March, 2003. MGS observed these profiles. The electron densities are calculated on both days due to impact of X-rays (1-8 Å).

4.3.2 Calculation of ion density profiles in the E region of Mars' ionosphere due to impact of solar X-ray flares

In figures 4.8a and 4.8b we have plotted flare induced densities of six ions CO_2^+, N_2^+, O_2^+, O^+ NO^+, and CO^+ in the E region ionosphere of Mars between altitudes 80 and 200 km during the two flare events that occurred on 6 April, 2001 and 17 March 2003. In the E region ionosphere the densities of O_2^+ is proportional as $[O_2^+]$ α $[CO_2^+]$ [O]/N_e, where [N_e] and $[CO_2^+]$ are the densities of electron and CO_2^+. Although the production rate of CO_2^+ is dominant, it is quickly destroyed by atomic oxygen resulting in O^+ and O_2^+ ions in the Martian ionosphere. The ion NO^+ is formed owing to the destruction of O_2^+ with NO. The O_2^+ and NO^+ ions are entirely destroyed by dissociative recombination process. The ion O^+ is mostly destroyed by CO_2. This is a very fast reaction to permit the development of a significant layer of O_2^+ in the E region. The peaks of CO_2^+ and O_2^+ are located at about 110 km and 100 km respectively. The ion densities of major ion O_2^+ for two flares of 6 April, 2001 and 17 March, 2003 are estimated to be 2.5 x 10^5 cm^{-3} and 1.2 x 10^5 cm^{-3} respectively. In Table 1 strongest X-ray flare X14.4 occurred on 15 April, 2001. We have not calculated the electron and ion densities corresponding to this flare event because the response of this flare on the Marian ionosphere and its corresponding flare electron density profiles has been reported by Lollo et al (2012) in detail. The effects of 6 April, 2001 and 17 March, 2003 flares have been observed in the D region of Earth's ionosphere. There is no measurement and modeling of these flares responses in the D region of Mars' ionosphere. Therefore in Chapter 3 we have estimated electron density for both flare days in the D region of Mars' ionosphere and compared them with the D region of Earth's ionosphere. In Chapter 4 the modeling of ion and electron densities in the E region ionosphere of Mars are carried out on 6 April, 2001 and 17 March, 2003 and compared them with the MGS observations on both flare days. Our model results are also compared with the other model calculation of Lollo et al. (2012) in Section 4.3.3.

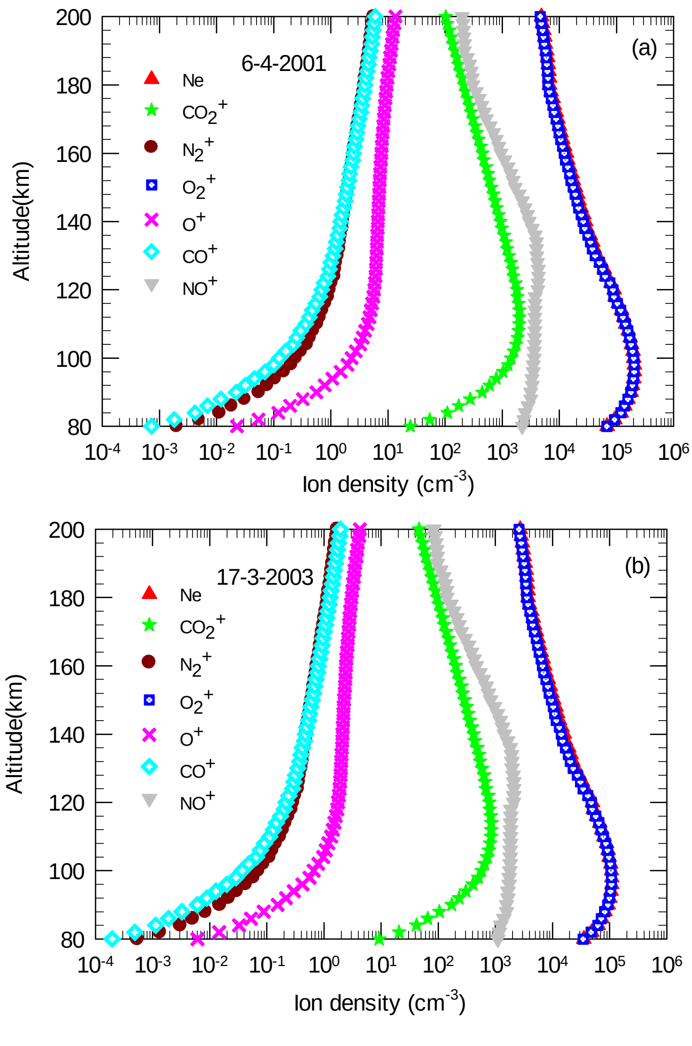

Figure 4.8 (a, b) Model calculation of ion densities of CO_2^+, N_2^+, O_2^+, O^+, CO^+, and NO^+ due to X-ray impact on (a) 6 April, 2001 and (b) 17 March, 2003 in the E region ionosphere of Mars. These calculations are carried out during the two flare events that occurred on 6 April, 2001 and 17 March, 2003.

4.3.3 Comparison of present and other model results of electron densities in the Martian ionosphere during flare event

There have been several studies on the effect of solar flares in E region ionosphere of Mars. Bougher et al. (2001) modeled the electron density profile observed by MGS in the daytime ionosphere of Mars by using Mars Thermosphere General Circulation model. They found a large difference between model and MGS measurements. Therefore, they increased solar x-ray fluxes (18-50Å) by factor of 10 in their model to produced E peak electron density for comparison with MGS observations. Fox (2004) constructed standard models by adopting the SC#21REFW and F79050N solar fluxes (Torr and Torr, 1979) for the calculation of photoionization rate, photoelectron impact ionization rate, ion density, and electron density in the daytime ionosphere of Mars for low and high solar activity periods. They did not model the MGS electron density profiles observed at flare time. However, Fox suggested that increasing the solar X-ray flux by a uniform factor cannot reproduce the E peaks that have been observed by the MGS. Later, Haider et al. (2009a , 2012), Mahajan et al. (2009), Lollo et al. (2012), and Fallows et al. (2015) modeled the E region ionosphere of Mars during flare period which describe in section 4.1.1. Recently, Haider et al. (2016) modeled six electron density profiles of Mars, which were strongly perturbed in the E region due to X-ray flares of 28 March and 6 April 2001, 17,18 March and 21, April 2003 and 19 February ,2005. They have found that the ion production rates, photoelectron flux, and ion and electron densities increased by 1–2 orders of magnitude at the peak of X-ray flares. They report that the estimated IEC of E layer increased by factors of 5–10 at the peak flare time compared to a factor of ~2 enhancements in the normalized IEC of the corresponding MGS profile, measured at variable times after the peak flare.

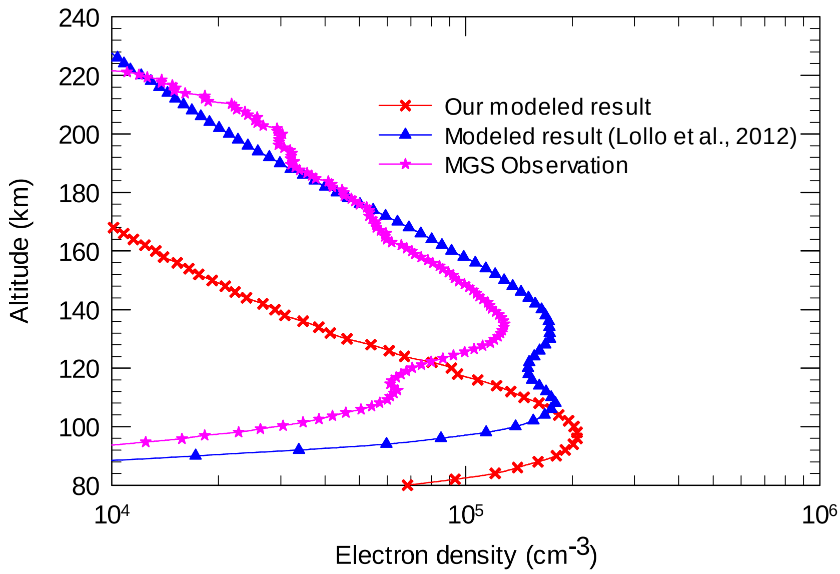

Figure 4.9 Comparison between the electron density profiles of our modeled result of 6 April 2001(blue triangle), Lollo et al. (2012) modeled result of 15 April, 2001 (red cross) and MGS observation during flare period from 80 to 200 km (pink star).

Among all these theoretical studied our result is close by the result of Lollo et al. (2012). Lollo modeled electron density profiles of 15 April 2001 which shows the largest electron density profile in E region. Their E peak electron density is larger than F region. In figure 4.9 we have shown the comparison between our model results of 6 April 2001, Lollo et al. (2012) modeled result of 15 April, 2001 and MGS observation. Lollo has modeled E and F peak both during flare condition. We have only reproduced the E region. The theoretical E peak density of Lollo et al. (2012) is larger by factor of ~2.5 than that observed by MGS. There is no theoretical electron density calculation in E region ionosphere of Mars during flare period for 6 April, 2001. Therefore we have compared our model result with Lollo et al. (2012), which was the nearest date with 6

April, 2001. By comparing these three electron density profiles, we conclude that the two theoretical model result show the nearly same enhancement during flare time and larger by factor of ~2-3 than MGS observation.

❐❐❐

REFERENCES

Bhardwaj, A., Haider, S. A., and Singhal, R. P (1990), Auroral and photoelectron fluxes in cometary ionosphere, Icarus, **85**, 216–228.

Bougher, S. W., Engel, S., Hinson, D. P., and Forbes, J. M (2001), Mars Global Surveyor radio science electron density: Neutral atmosphere implications, Geophys. Res. Lett., **28**, 3091–3094.

Buckman, S. J., Brunger, M. J, and Elford,M. T (2002), Cross sections for electron collisions with carbon dioxide, in Photon and Electron Interaction With Atoms, Molecules and Ions, Landolt-Bornstein Ser., vol. **17D**, edited by Y. Itikawa. 749–767, Springer, Berlin.

Fallows, K., Withers, P., and Gonzalez, G (2015), Response of the Mars ionosphere to solar flares: Analysis of MGS radio occultation data, J. Geophys. Res., **120**, 9805–9825.

Fox, J. L (1993), The production and escape of nitrogen atoms on Mars, J. Geophys. Res., **98**, 3297–3310.

Fox, J. L (2009), Morphology of the dayside ionosphere of Mars: Implications for ion outflows, J. Geophys. Res., **114**, 1-18, E12005.

Fox, J. L (2004), Response of the Martian thermosphere/ionosphere to enhanced fluxes of solar soft X-rays, J. Geophys. Res. **109**, 1-18, A11310.

Gopalswamy, N., Yashiro, S., Mäkelä, P., Michalek, G., Shibasaki, K., and Hathaway, D. H (2012), Behavior of solar cycles 23 and 24 revealed by microwave observations, Astrophys. J.,**750**, L42.

Gurnett, D. A., Kirchner, D. L., Huff, R. L., Morgan, D. D., Persoon, A. M., Averkamp, T. F, et al. (2005), Radar soundings of the ionosphere of Mars, Science **310**, 1929–1933.

Haider, S. A., Batista, I. S., Abdu, M. A., Santos, A. M., Shah, S. Y, et al. (2016), Flare X-ray photochemistry of the E region ionosphere of Mars, J. Geophys. Res., Space Physics, **121**, 6870-6888.

Haider, S. A., Abdu, M. A., Batista, I. S., Sobral, J. H., Kallio, E., Maguire, W. C, et al.(2009a), On the responses to solar X-ray flare and coronal mass ejection in the ionosphere of Mars and Earth, Geophys. Res. Lett., **36**, 1-5.

Haider, S. A., Abdu, M. A., Batista, I. S., Sobral, J. H., Luan, X., Kallio, E, et al. (2009b), D, E, and F layers in the daytime at high-latitude terminator ionosphere of Mars: Comparison with Earth's ionosphere using COSMIC data, J. Geophys. Res., **114**, 1-12,A03311

Haider, S. A., Mahajan, K. K., and Kallio, E (2011), Mars ionosphere: A review of experimental results and modeling studies, Reviews of Geophysics, **49**(4), 1-37.

Haider, S.A., and Mahajan, K. K (2014), Lower and Upper Ionosphere of Mars, Space Sci. Rev., **182**, 19-84

Haider, S. A., McKenna-Lawlor, S. M. P., Fry, C. D., Jain, R., and Joshipura, K. N (2012), Effects of solar X-ray flares in the E region ionosphere of Mars: First model results, J. Geophys. Res., **117**, 1-13, A05326.

Hinson, D. P., Simpson, R. A., Twicken, J. D., Tyler, G. L., and Flasar, F. M (1999), Initial result from radio occultation measurements with Mars Global Surveyor, J. Geophys. Res., **104**, 26997-27012.

Itikawa, Y (2002), Cross sections for electron collisions with carbon dioxide, J. Phy and Chem Reference Data, **31**, 749-767.

Lollo, A., Withers, P., Fallows, K., Girazian, Z., Matta, M., and Chamberlin, P. C (2012), Numerical simulations of the ionosphere of Mars during a solar flare, J. Geophys. Res.**117**, 1-13, A05314.

Mahajan, K. K., Lodhi, N. K., and Singh, S (2009), Ionospheric effects of solar flares at Mars, Geophys. Res. Lett., **36**, 1-5, L15207

Martinis, C. R., Wilson, J. K., and Mendillo, M. J. (2003), Modeling day-to-day ionospheric variability on Mars, J. Geophys. Res., **108**, (8)1-(8)-6.

Mendillo, M., Withers, P., Hinson, D., Rishbeth, H., and Reinisch, B (2006), Effects of solar flares on the ionospheres of Mars, Science, **311**, 1135-1138.

Millour, E., Forget, F., Spiga, A., Navarro, T., Madeleine, J. B., Pottier, A, et al. (2014), A new Mars climate database v5.1, paper 1301 presented at The Fifth International Workshop on Mars Atmosphere: Modeling and Observations, Oxford, U. K., Jan. 2014.

Nielsen, E., Zou, H., Gurnett, D. A., Kirchner, D. L., Morgan, D. D., Huff, R et al. (2006), Observations of vertical reflections from the topside Martian ionosphere, Space Sci. Rev., **126**, 373-388.

Pätzold, M., Tellmann, S., Häusler, B., Hinson, D., Schaa, R., and Tyler, G. L (2005), A sporadic third layer in the ionosphere of Mars, Science, **310**, 837–839.

Petrova, E. V., Hoekzema, N. M., Markiewicz, W. J., Thomas, N., and Stenzel, O. J (2012), Optical depth of the Martian atmosphere and surface albedo from high-resolution orbiter images, Planet. Space Sci., **60**, 287-296.

Porter, H. S., and Jump,F. W. (1978), Analytical total and angular elastic electron impact cross sections for planetary atmospheres, Tech. Rep. CSC/TM-78/0017, Comput. Sci. Corp., Greenbelt, Md. USA

Schunk, R. W., and Nagy, A. F. (2000), Ionospheres: Physics, Plasma Physics and Chemistry, Cambridge Univ. Press, New York.

Torr, D. G., and Torr, M. R. (1979), Chemistry of the thermosphere and ionosphere, J. Atmos. Terr. Phys., **41**, 797–839.

Tsurutani, B. T., Judge, D. L., Guarnieri, F. L., Gangopadhyay, P., Jones, A. R., Nuttall, J, et al. (2005), The October 28, 2003 extreme EUV solar flare and resultant extreme ionospheric effects: comparison to other Halloween events and the Bastille Day event. Geophys. Res. Lett. **12**, 1-4, L03S09.

Withers, P., Mendillo, M., Hinson, D. P., and Cahoy, K (2008), Physical characteristics and occurrence rates of meteoric plasma layers detected in the Martian ionosphere by the Mars Global Surveyor Radio Science Experiment, J. Geophys. Res. **113**, 1-15, A12314.

❒❒❒

CHAPTER - 5

EFFECT OF DUST STORM ON OZONE COLUMN DENSITY

CONTENTS

The study of a dust storm is a key problem in the lower atmosphere of Mars. We have developed a seasonal dependent energy loss model to calculate the production rate of O_3^+ in presence and absence of dust storm at low, mid and high latitudes between Ls~0º to 360º due to impact of GCR in daytime troposphere of Mars. The mixing ratio of O_3 is multiplied with air density to obtain the neutral density of ozone at different Ls and latitudes. In this chapter we have studied seasonal variability of O_3 column density during the daytime for MY 28 and MY 29. These model results are compared with the daytime observations of column ozone made by SPICAM onboard MEX. We report that that ozone is maximum in winter and minimum in summer. Ozone column density, dust opacity and production rates of O_3^+ were increased by a factor of ~3-4 during the dust storm period near the surface of Mars in MY 28 in southern hemisphere.The peak production rates of O_3^+ occurred between altitudes 30 km and 40 km, which increased up to Ls = 47.5º and it disappeared after Ls ~ 127.5º.

5.1 INTRODUCTION

The Martian atmosphere consists of mainly CO_2 (95.3%) and N_2 (2.7%). The remaining 2% of the atmospheric gases are known as trace gases because their concentrations are very small. The most abundant of the trace gases is the noble gas Ar (approximately 1.6%), which does not take part in any chemical transformation within the atmosphere. The other trace gases are O, O_2, CO, H_2O and O_3. The Martian atmosphere also contains dust particles of radius ≤ 3 µm as a tracer (Guzewich et al., 2014; Haider et al., 2015). These particles are composed of a combination of clay, basalt and silicate materials swept up from the surface to soil into atmospheric circulation. Baseline visible opacity due to dust is around 0.2. This is observed in the clear aphelion season. The global dust storms can lift a large amount of dust into the atmosphere and cause opacities in excess of unity (Smith et al., 2013). Stability and composition of Martian atmosphere are controlled by photochemical processes (Krasnopolsky 2006). The SPICAM onboard MEX has provided continuous observations of UV dust opacity and ozone column density from nadir direction. (Montmessin et al., 2017). We have studied the seasonal variation of column ozone at different latitude and compared it with model results in presence and absence of dust storm. In section 2.1.1 we have developed a seasonal dependent energy loss model to calculate the zonally averaged production rates of O_3^+ due to impact of GCR in the dayside troposphere of Mars between Ls ~ 0^o and 360^o at low, mid and high latitudes in MY 28 and MY 29.

5.1.1 SPICAM observations: O_3 column density

Ozone strongly absorbs UV radiation in the wavelength range 200 nm to 315 nm. The ozone is a sensitive tracer of the hydrogen photochemistry that stabilizes the Mars CO_2 atmosphere. It also provides important information on the conditions of habitability on the planet, not only by determining the ultraviolet flux reaching on the surface, but also as an indirect tracer of the oxidizing capacity of the atmosphere by hydrogen oxides. It was detected for the first time by absorptions of Hartley band in UV as well as IR features by the ultraviolet (UV) spectrometer on board Mariner 7 flyby (Barth and Hord, 1971). There are few instruments which explored to observe ozone in the Martian atmosphere. The UV spectrometer onboard Mariner 9 (Barth et al., 1973), SPICAM onboard MEX (Perrier et al., 2006), and MARCI (Mars Color Imager) onboard MRO (Mars Reconnaissance Orbiter) (Clancy et al., 2016) have measured the ozone abundance. The nighttime measurements of O_3 were carried out by SPICAM using stellar occultation method (Montmessin and Lefevre, 2013). This measurement cannot provide profiles of O_3 in the daytime atmosphere at altitude ≤ 60-80 km where star signals are very weak. There have been observed two main layers of O_3 in the atmosphere of Mars, one layer is located near the surface and second layer is observed in the middle atmosphere between 25 km and 60 km (cf. Montmessin et al., 2017). The column density of O_3 varies strongly with latitude and seasons (Haider et al., 2019). This is due to the fact that solar UV radiation is highest in the tropics and the large scale air circulation transports tropical ozone toward the pole.

5.1.2 Observations of dust storm on Mars

Dust is the most important component of Martian meteorology. Dust affects the incoming and outgoing solar radiation by its radiative properties. Martian atmosphere is characterized by global dust storms, regional dust storms, and local dust storms (Sheel and Haider, 2016). Dust optical depth varies with respect to season and also with global and regional storm. Several dust storms have been observed on Mars in MY10, MY13, MY25 and MY28 (Martin, 1984, 1995; Smith et al., 2013; Montabone et al., 2015). The infrared optical depths were increased to ~1.5 to 2.6 during the dust storm period. The Thermal Emission Spectrometer (TES) and Thermal Emission Imaging System (THEMIS) instruments onboard MGS and Mars Odyssey have observed dust optical depths from 1998 to 2004 and 2004 to 2014 respectively. The climatology of eight Martian years of dust loading has revealed that there is always a background aerosol loading optical depth of about 0.1 between Ls = 0^o and 160^o corresponding to a period when dust storm are absent, while the optical depth increases every year to values in the range 0.3-0.5 corresponding to regional dust storms which typically occur at Ls = 220^o (Haider et al., 2015; Sheel and Haider, 2016; Haider et al., 2019). The optical depth increased up to 1.7 at Ls = 210^o in southern tropics during MY 25 global dust storm. In global dust storm of MY 28 the optical depth increased up to 1.2 at Ls = 280^o.Recently, a new major global dust storm has been observed by MASTCAM onboard Mars Science Laboratory (MSL) in MY 34 when the dust optical depths were increased to 8.5 in June 2018 (Guzewich et al., 2019). The SPICAM spectrometer onboard MEX also measured

UV dust opacity during MY 28 in dayside ionosphere of Mars (Montmessin et al., 2017). We represent the seasonal variability of dust optical depth from SPICAM instrument onboard MEX in MY28 and MY 29 at 25ºS-35ºS latitude in figure 5.1.

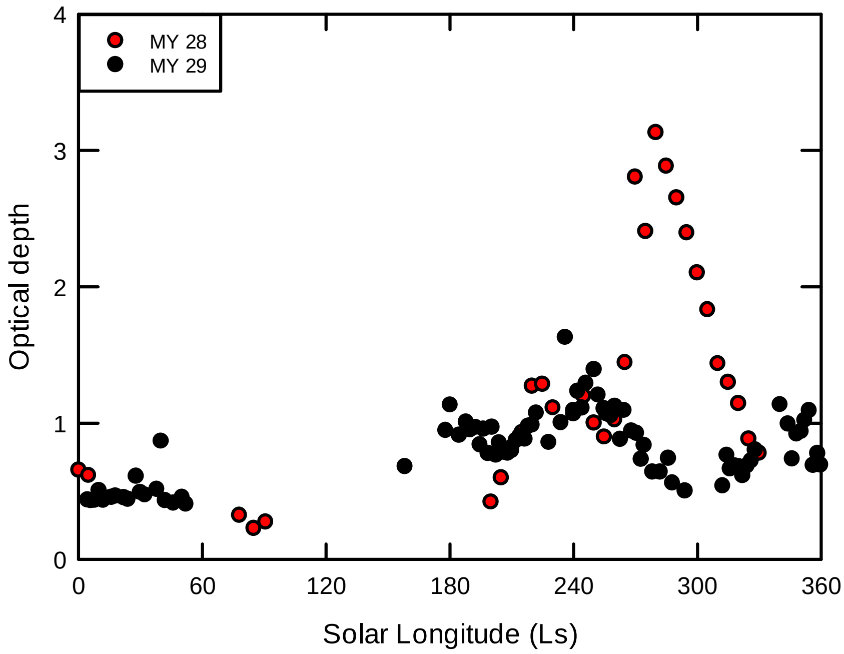

Figure 5.1. The zonally average UV dust optical depths as observed by SPICAM in MY 28 and MY 29 at southern latitude (25ºS-35ºS).

In this figure SPICAM UV dust optical depths are plotted from Ls = 0° to 360° in MY 28 and MY 29. The major dust storm can be seen in MY 28, when optical depth increased up to 3.0 at Ls = 280º. In MY 29 the optical depth is observed to be 0.5 at this solar longitude.

5.1.3 Correlation between Ozone and Dust

. The O_3 molecule is produced mainly due to product of O and O_2 by three body reaction using CO_2 as third body. The O_3 is destroyed by hydrogen radicals (OH), which are obtained from parent water. Therefore an ant-correlation between the abundance of water vapor and ozone is found in the Martian atmosphere (Lefevre et al., 2008). During the dust storm a thick layer of dust is observed above the surface of Mars (Haider et al., 2015). In presence of thick layer of dust, the sunlight cannot penetrate deep into the atmosphere of Mars. This interrupts the dissociation of ozone below the dust layer which is the main loss mechanism of ozone in the dayside atmosphere. On the other hand the production of O_3 is directly related to the production of the oxygen atom, which is produced more above the dust layer from the photolysis of CO_2. Therefore the ozone will be increased during the dust storm period below the dust layers.

Martian dust is known to impact various photochemical reactions in the Mars' atmosphere. In presence of dust storms large scale electrostatic fields are generated by charged dust. The positive and negative charged dusts are impacting with the atmospheric gases O_2 and O and produced O_3^+ and O_3^- respectively. Later O_3 is formed due to dissociative recombination of O_3^+ with electron and photo dissociative attachment of O_3^- respectively. This process is known as tribo-electricity. In presence of tribo-electricity lightning can also occur in the Martian atmosphere (Haider et al., 2010). The typical dust abundances can induce 10-50% increase in O_3 abundances during the lightning on Mars (Lindner et al., 1988).

5.2 DENSITY OF OZONE: MCD MODEL

Ozone is mainly produced in the sunlit latitudes where oxygen atoms are abundant due to dissociation of CO_2 and O and combine with O_2 to produced O_3. During winter season the contribution to ozone comes mainly due to transport of ozone from sunlit latitudes. During summer, polar caps release water vapor and destroyed the ozone. Ozone is maximum during winter and minimum during summer in general for all latitudes (Barth et al., 1973). The seasonal variability of ozone is studied at low, mid and high latitudes using a MCD model (Millour et al., 2014). The MCD included photochemistry, dynamics and other metrological fields of the Martian atmosphere. This model calculates altitude profiles of air density, mixing ratios of CO_2, O_2, O, CO, O_3, H, H_2, N_2, Ar and H_2O, neutral temperature, pressure and winds at different season, latitude and longitude in the dayside and night side atmosphere above the surface of Mars. We have taken ozone densities between 0 to 60 km from the MCD model at low latitudes (2^oN, 2^oS, 25^oN and 25^oS), mid latitudes (45^oN and 45^oS) and high latitudes (70^oN and 70^oS) between Ls ~ 0^o and 360^o in presence and absence of dust storm that occurred in MY 28 and MY 29 respectively.

5.2.1 Seasonal variability of ozone in presence and absence of dust storm

We represent zonal averaged ozone column density obtained from MCD between Ls ~ 250^o and 350^o at latitude 25^oS in MY 28 and MY 29 in figure 5.2. A major dust storm occurred in MY 28 at Ls = 280^o in southern latitudes. When there is a thick layer of dust, sunlight cannot penetrate deep into the atmosphere. This interrupts ozone to dissociate below the dust layer in the lower atmosphere. This is a main loss mechanism of ozone. The major production mechanism of ozone depends on oxygen atom (O), which is produced more from the photolysis of CO_2 above the dust layer. Thus, ozone column density will be more during the dust storm period. We have found that the column density of ozone is increased during dust storm by a factor of ~2.6 at Ls = 280^o in MY 28.

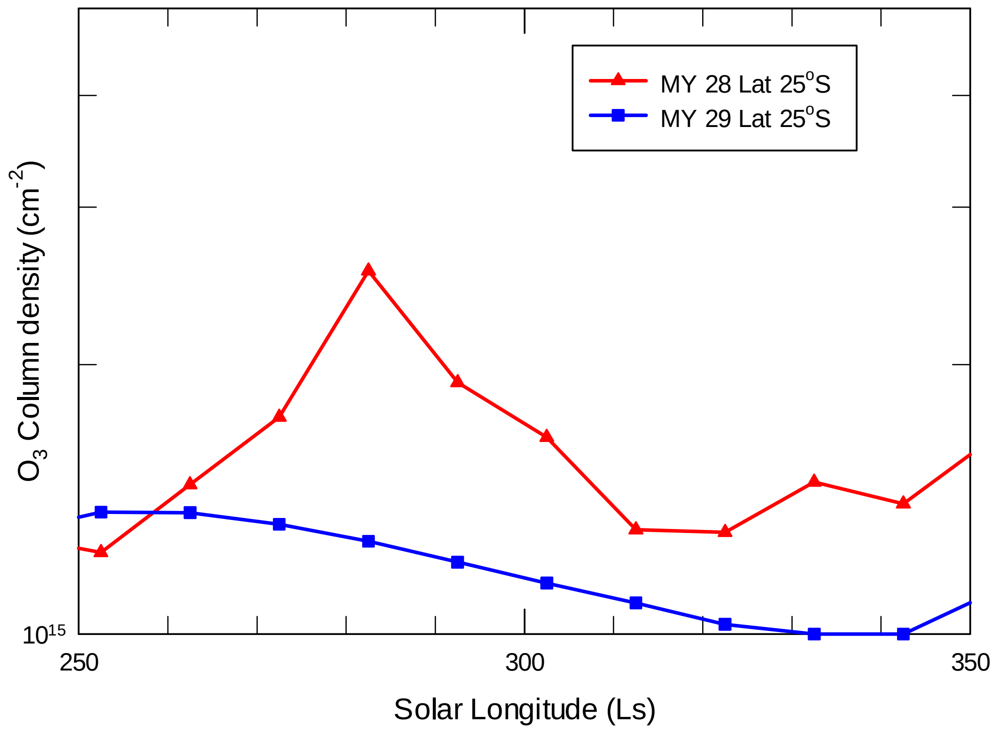

Figure 5.2 Ozone column density from MCD model at 25°S latitude between Ls = 250° to 350° for MY 28 and MY 29.

5.2.2 Estimated column density of ozone in MY28: Comparison with SPICAM observations

In this Section we represent the ozone column density observed by SPICAM in MY 28 during the daytime at low, mid and high latitudes. We have averaged SPICAM observations over longitude for each Ls and latitude. These observations are compared with the zonally averaged ozone column densities obtained from MCD in MY 28 in figures 5.3(a-h). The observed column densities are plotted with 1-σ error bars. The seasonal variability of ozone column density in MY 28 are enhanced at Ls~280° during the dust storm that occurred in southern hemisphere at latitude ~ 25°S. Ozone column density is maximum at high latitude during winter. The total amount of ozone in the atmosphere of Mars undergoes seasonal variation due to formation of the polar caps. The amount of ozone gas increases and decreases due to condensation and sublimation processes respectively. Our results also represent that at high latitude of both hemispheres column density of O_3 are maximum in winter and minimum in summer. At high latitudes estimated values of ozone column densities are in good agreement with the SPICAM observations. The model underestimates the O_3 column density at low and mid latitude. There is about one order of difference in SPICAM observations and MCD model results at low and mid latitudes. The disagreement between observation and model at low latitudes may be associated due to several reasons: (1) The excessive transport of water vapor from Tharsis and Arabia Terrain can reduce column ozone in the model (Steele et al., 2014),(2) Modeling biases in water vapor can also explain the underestimation of total ozone at low latitude region (Holmes et al., 2018), (3) The SPICAM measurements have large error of the order of 1-5 x 10^{15} molecules cm^{-2} (Lebonnois et al., 2006).The estimated column densities of ozone are varying within this error bar at low latitude region and (4) Ozone can also be affected by topography of Mars through the effect of gravity waves. An increase in O_3 column over Hellas basin in SPICAM measurements is attributed to a topographical induced transport of the polar air (Clancy et al., 2016).

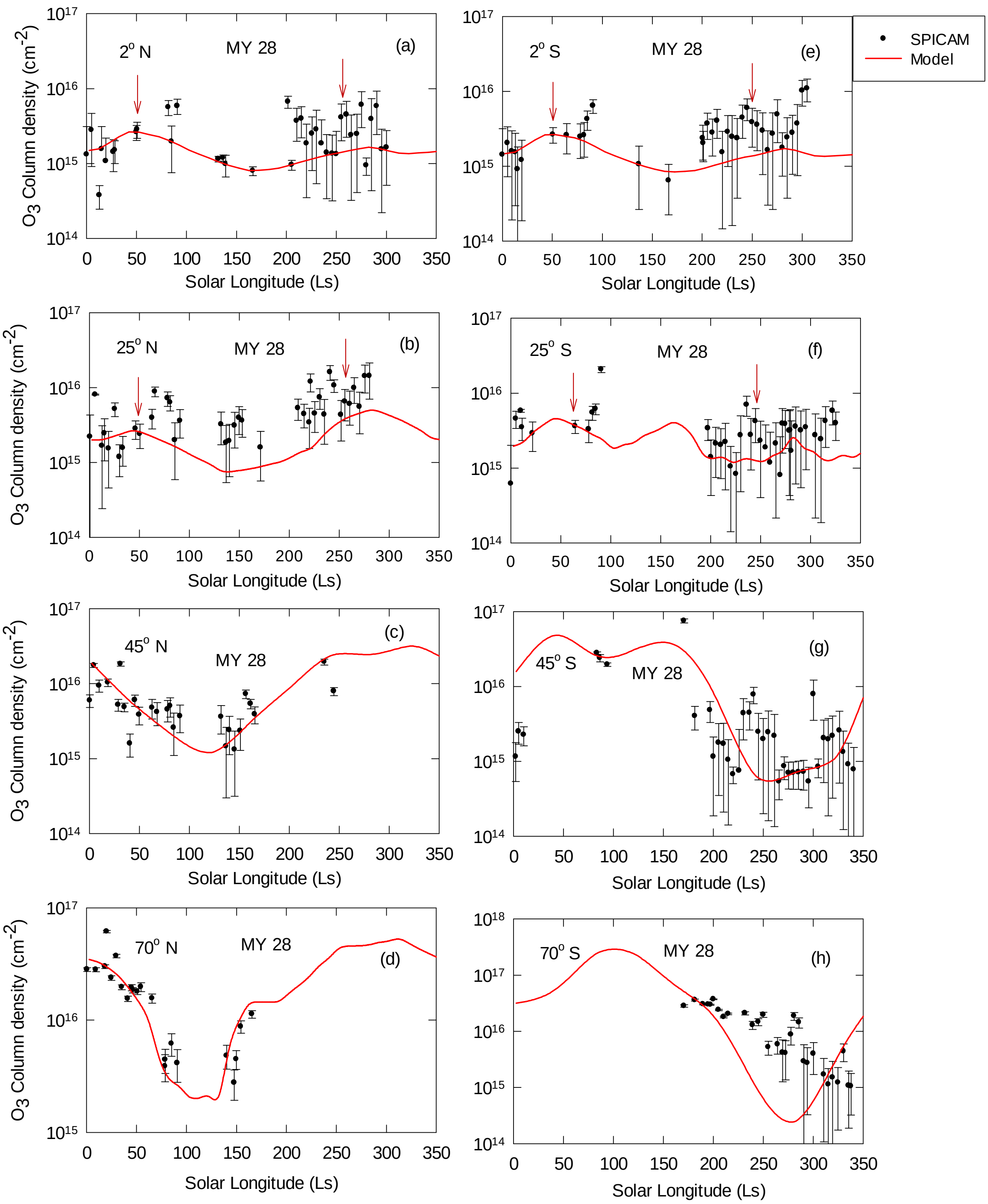

Figure 5.3. Zonally averaged ozone column densities with error bars as observed by SPICAM in MY 28 at low, mid and high latitude. These observations are compared with zonally averaged ozone column densities obtained from MCD model in MY 28 in the daytime ionosphere of Mars.

5.2.3 Estimated column density of ozone in MY29: Comparison with SPICAM observations

This section compares the estimated and measured column densities of ozone in MY29 at low, mid and high latitudes. The observed profiles are obtained from SPICAM observations between Ls = 0^o to 360^o at latitudes 2^oN-S, 25^oN-S, 45^oN-S and 70^oN-S. The model profiles are obtained from MCD model. The comparison of estimated and measured column ozone densities are shown in figure 5.4 (a-h). The observed column densities are plotted with 1-σ error bars. As noted in figure 5.3 (a-h) the column ozone densities are increasing and decreasing due to condensation and sublimation processes respectively. The results shown in figure 5.4 (a-h) are nearly same as shown in figure 5.3 (a-h) except at Ls = 280^o where the column ozone were increased by a factor of ~ 3 during the dust storm of MY28.

The two peaks have been observed in ozone column density at low latitudes i.e. ~5-8 x 10^{15} cm^{-2} and ~ 1.2 x 10^{16} cm^{-2} at Ls ~ 50^o and Ls ~ 250^o. At mid-to high latitudes the ozone column densities are maximum in northern winter and minimum in southern summer. In both hemispheres the column densities of ozone are lower at mid-latitudes by a factor of 2-5 than the column densities of ozone at high latitudes. In northern hemisphere the ozone is not measured between Ls ~ 250^o and 350^o at mid-to high latitudes.

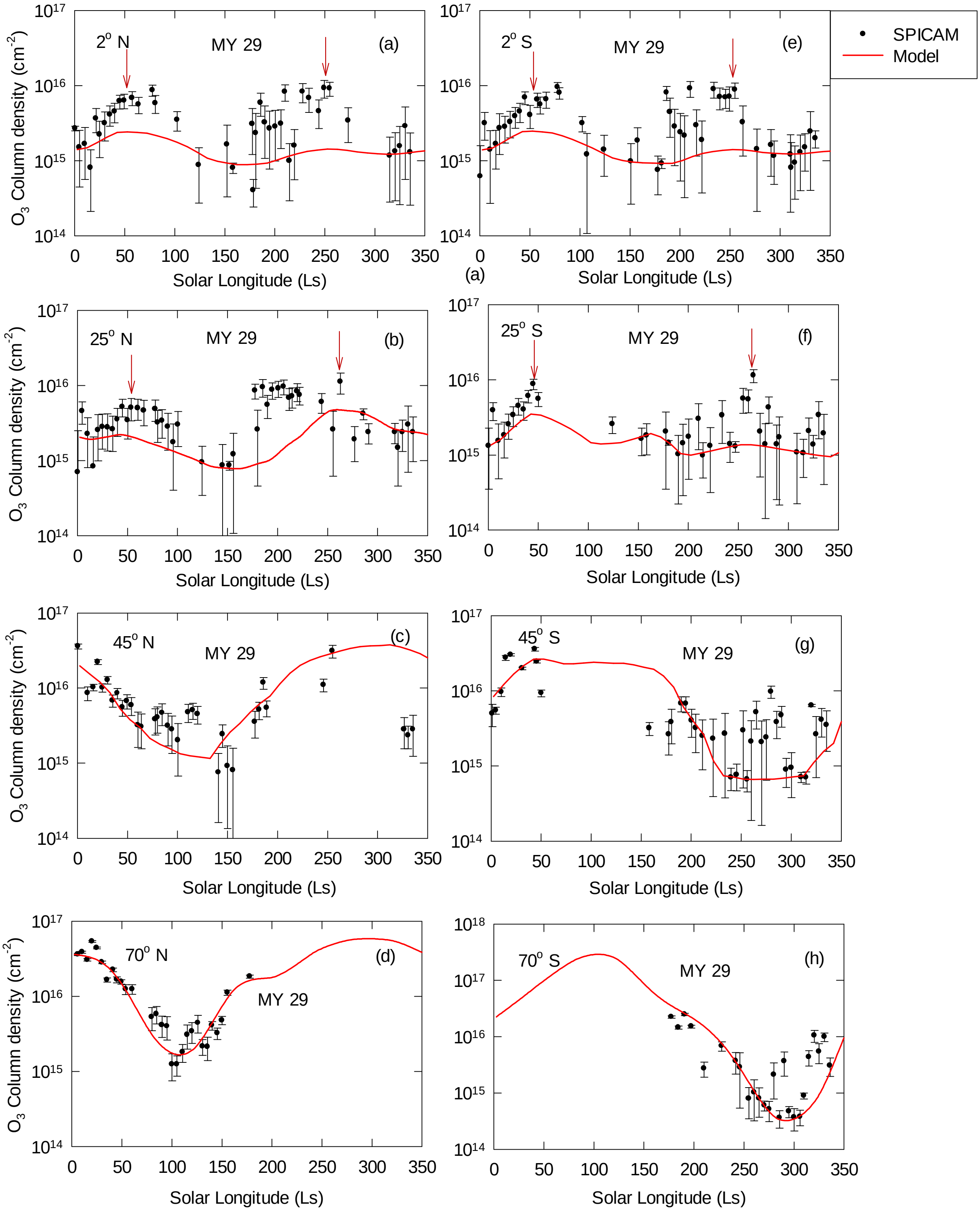

Figure 5.4 Same as in figure 5.3 but for MY 29.

This calculation suggests that the ozone is maximum in winter, when condensation on polar caps suppresses most of the atmospheric water vapor. Ozone is minimum in summer indicating an efficient O_3 destruction by the HO_X radical released from large amount of water vapor and sunlight.

5.3 PRODUCTION RATE OF O_3^+ DUE TO GCR IMPACT

In Chapter 2 the energy loss model has been developed for the calculation of the ion production rates of O_3^+ due to impact of GCR in the lower ionosphere of Mars. We have carried out this calculation at low, mid and high latitudes in MY 28 and MY 29. We do not know how much GCR flux is reaching at the top of the Mars' atmosphere. We have assumed that GCR flux of magnitude from 10^3 to 10^{-5} particles m^{-2} s^{-1} GeV^{-1} $ster^{-1}$arrived at the top of the Mars' atmosphere between energy range 1-1000 GeV (Haider et al., 2009b). In this model calculation we have taken neutral density of ozone from MCD model for observing condition of SPICAM. We have used same GCR flux at all latitude and seasons because the un-attenuated flux does not depend on latitude and season. The production rates of O_3^+ are calculated on the surface of Mars between Ls = 0^o and 360^o.We have also estimated the vertical profiles of the production rates of O_3^+ in the dayside ionosphere of Mars at different Ls and latitude.

5.3.1 Production rate of O_3^+ on the surface

Seasonal variability of ion production rate of O_3^+ at latitude 2^oN-S, 25^oN-S, 45^oN-S and 70^oN-S are shown in figure 5.5 on the surface of Mars between Ls = 0° to 360° in MY 28 and MY 29. We have calculated the production rates of O_3^+ from energy loss model due to impact of GCR in the dayside ionosphere of Mars. This calculation carried out near the surface of Mars. The production rates of O_3^+ were also enhanced by a factor of ~ 3 in MY 28 during dust storm period when optical depth was increased up to 3.3. The maximum production rate occur between 40N° to 70N° near the surface. In southern hemisphere, maximum production occurs at same latitudes. In the southern hemisphere, equatorial region the ozone production rate is qualitatively similar to that of the northern hemisphere. But in the southern hemisphere for MY 28, the mid latitudinal region (25°S) we see that at production rate of ozone is increases in presence of dust storm. The high correlation of O_3 production rate with dust is observed in southern latitudes in MY 28 during dust storm period at Ls ~ 280°. The maximum and minimum ions of O_3^+ are produced in the winter and summer seasons of Mars respectively.

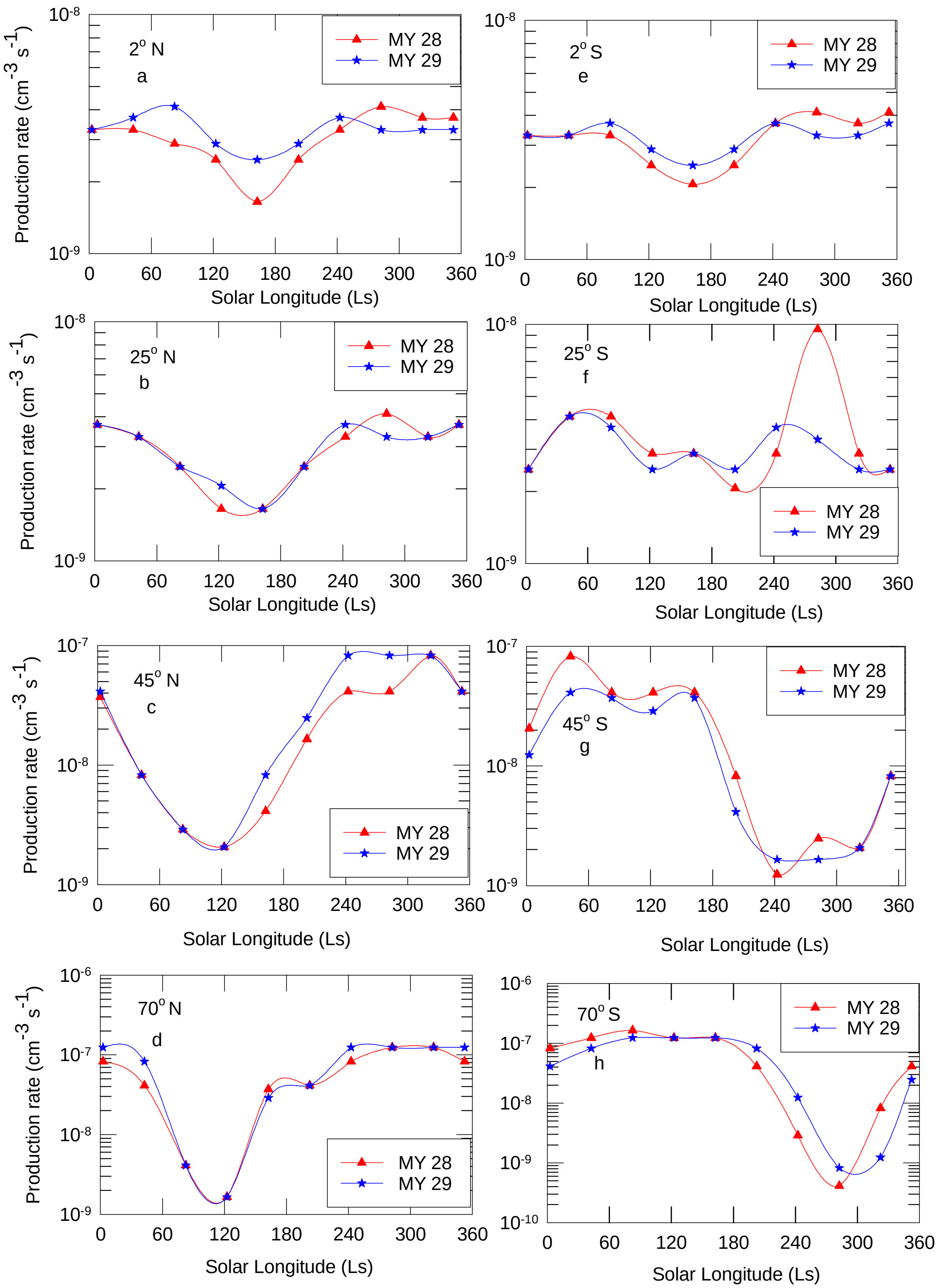

Figure 5.5. The zonal mean production rates of O_3^+ on the surface of Mars at latitudes 2ºN (a), 25ºN (b), 45ºN (c), 70ºN (d), 2ºS (e), 25ºS (f), 45ºS (g) and 70ºS (h) in MY 28 and MY 29.

5.3.2 Altitude profiles of production rate of O_3^+

We have also calculated vertical profiles of production rates of O_3^+ in the dayside ionosphere of Mars. The production rates of O_3^+ are nearly same in MY 28 and MY 29 at same latitudes and same seasons. Therefore we have only shown the vertical profiles of the production rates of O_3^+ in MY 28. We have plotted these profiles in figures 5.6 (a, b, c, d) at latitudes 2°N-S, 25°N-S and in figure 5.7 (a, b, c, d) at latitudes 45°N-S and 70°N-S.

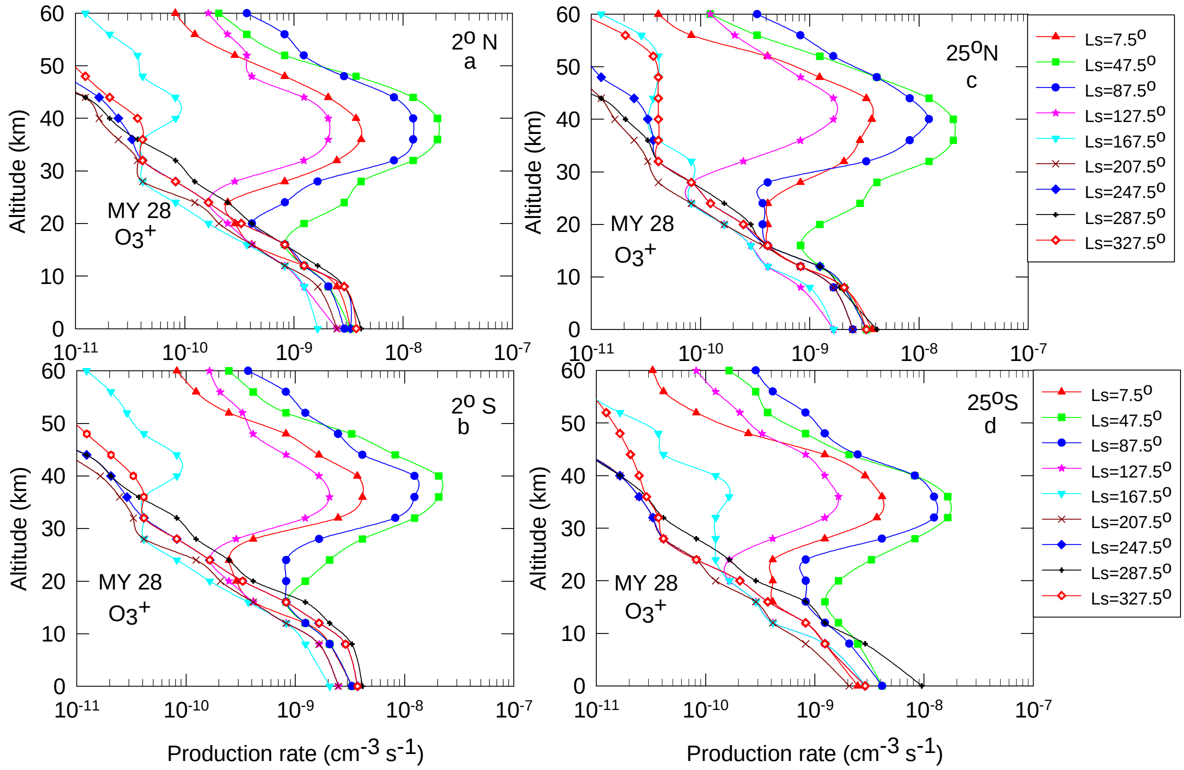

Figure 5.6. The vertical profiles of O_3^+ production rate in MY 28 at latitudes 2°N (a), 2°S (b), 25°N (c) and 25°S (d) for Ls = 7.5°, 47.5°, 87.5°, 127.5°, 167.5°, 207.5°, 247.5°, 287.5° and 327.5°

At latitude 2°N the production rates of O_3^+ represent a broad peak at altitudes 35 km, 40 km, 38 km, 36 km and 42 km with peak values 4 x 10^{-9}, 2.5 x 10^{-8}, 1.3 x 10^{-8}, 2.0

x 10^{-9} and 1.0 x 10^{-10} cm^{-3} s^{-1} at Ls = 7.5°, 47.5°, 87.5°, 127.5° and 167.5° respectively. The production rates of O_3^+ are nearly same at latitudes 2°N and 2°S as far as the peaks and their positions are concerned for Ls 7.5°, 47.5°, 87.5°, 127.5° and 167.5°. At latitude 25°N the peak production rates of O_3^+ occurred at altitudes 42 km, 39 km, 41 km and 45 km with peak values 4.0 x 10^{-9}, 2.0 x 10^{-8}, 1.5 x 10^{-8} and 2 x 10^{-9} cm^{-3} s^{-1} at Ls = 7.5°, 47.5°, 87.5° and 127.5° respectively. There is no clear peak in the production rate at latitude 25°N for Ls = 167.5°. The peak heights and peak production rates of O_3^+ are nearly same at latitudes 25°N and 25°S for Ls = 7.5°, 47.5°, 87.5° and 127.5°. The clear peak is found in the production rate at 25°S for Ls = 167.5°. At low latitudes (2°N-S and 25°N-S) the peak production rates of O_3^+ increased up to Ls ~ 47.5° with maximum value ~ 2 x 10^{-8} cm^{-3} s^{-1}. Later it decreased up to Ls ~ 127.5° and then disappeared at Ls ~ 167.5°, 207.5°, 247.5°, 287.5° and 327.5°.

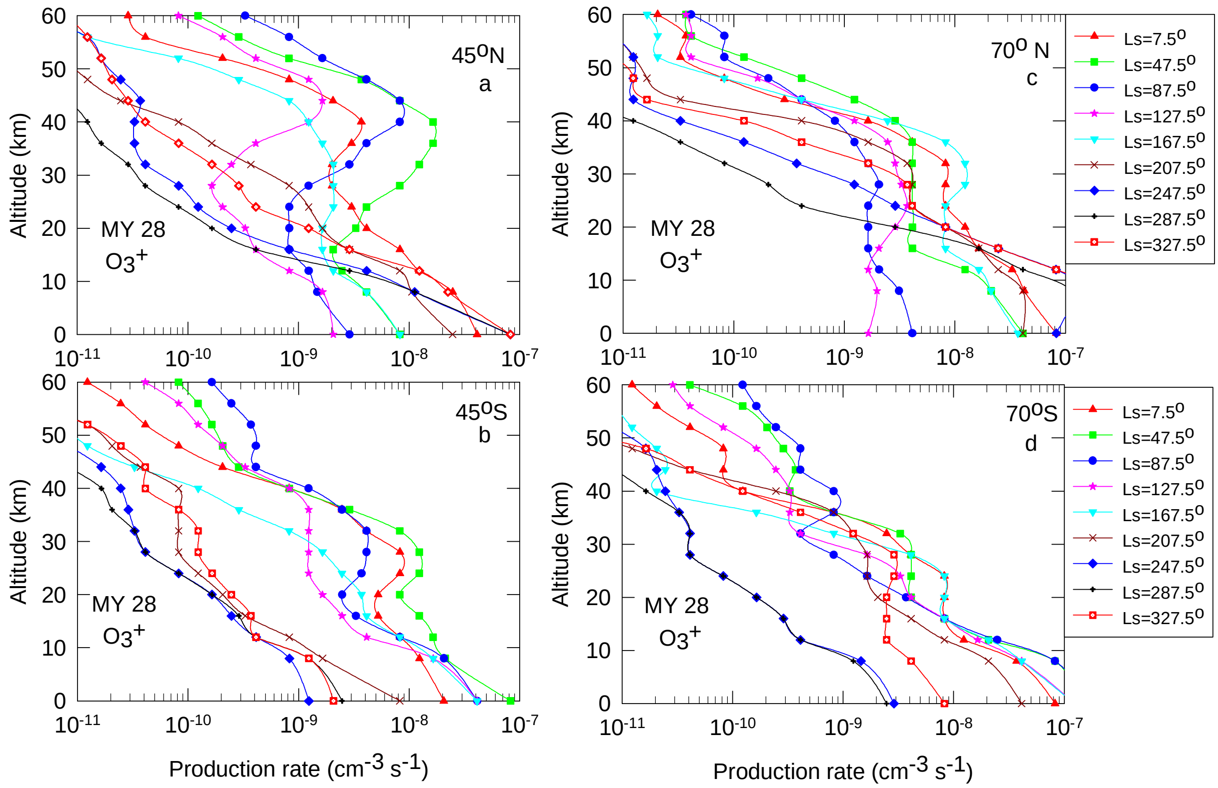

Figure 5.7 same as in figure 5.6 but for latitudes 45ºN (a), 45ºS (b) 70ºN (c) and 70ºS (d)

At latitude 45ºN the peak production rates of O_3^+ are estimated to be ~ 3.5 x 10^{-9}, ~1.5 x 10^{-8}, ~1.0 x 10^{-8} and ~1.8 x 10^{-9} cm^{-3} s^{-1} between altitude range 40 km to 45 km for Ls ~ 7.5º, 47.5º, 87.5º and 127.5º respectively. At latitude 45ºS the peak production rates of O_3^+ are estimated to be ~ 1.0 x10^{-8}, ~ 1.5x10^{-8}, 4.0x10^{-9} and 1.2 x10^{-9} cm^{-3} s^{-1} between altitude range 25 to 35 km for Ls ~ 7.5º, 47.5º, 87.5º and 127.5º respectively. These ionization peaks do not occur in the troposphere of Mars at polar latitudes ~70ºN and 70ºS. The production rates of O_3^+ contains more ozone near the peak than most of the remainder of the atmosphere. It absorbs a lot of UV radiation at low latitudes. The production layer of O_3^+ is higher in altitude at low latitudes and lower in altitude at mid-latitudes, especially in southern region.

At latitudes 45ºN, 45ºS, 70ºN and 70ºS the surface production rates of O_3^+ are increasing by two orders of magnitude in northern winter due to condensation of CO_2 frost. At these latitudes the surface production rates of O_3^+ are decreasing by two orders of magnitude in southern summer due to sublimation of CO_2 frost. During summer, polar caps are releasing water vapor which destroys the ozone (Lefevre et al., 2008). This process does not occur in northern polar winter which is too cool and protected from the formation of odd hydrogen species, which significantly contributes in the destruction of ozone. The ozone concentration peak at low-to mid-latitudes can be obtained between altitudes 25 km and 45 km at Ls ~7.5º, 47.5º, 87.5º and 127.5ºfrom the photolysis of O_2 which combines with O and forms the O_3 layer (Lefevre et al., 2004). This layer is fully destroyed by photo dissociation. These peaks are not clearly found in the production rates of O_3^+ at high latitudes in all seasons of both hemispheres.

Our model results suggest that the vertical profiles of ozone in the daytime consists a broad peak in both hemispheres between altitudes 25 km and 45 km at low to mid latitudes. These peak heights are reduced by about 10-20 km at southern mid latitudes. The peaks are not clearly found in the production rates of O_3^+ at high latitudes. We have not detected any peak in the daytime vertical profiles of the production rates of O_3^+ on the surface. The daytime ozone is produced mainly due to photolysis of CO_2 where oxygen atoms are abundant which combines with molecular oxygen to form the ozone. This confirms that the mechanisms of ozone formation in the dayside and nightside atmosphere of Mars are different at low and mid-to high latitudes. The dust increases the ion production rate by a factor of 3-4 on the surface in MY 28 (figure 5.5f).

The effect of dust on the production rate is nearly absent above ~ 10 km altitude (figure 5.7d). The peak production rate of O_3^+ is directly correlated with the abundance of ozone.

❑❑❑

REFERENCES

Barth, C. A., and Hord, C. W (1971), Mariner ultraviolet spectrometer: Topography and polar cap. Science, **173**, 197-201.

Barth, C. A., Hord, C. W., Stewart, A. I., Lane, A. L., Dick, M. L, et al. (1973), Mariner 9 ultraviolet spectrometer experiment: Seasonal variation of ozone on Mars. Science, **179**, 795-796.

Clancy, R. T., Wolff, M. J., Lefèvre, F., Cantor, B. A., Malin, M. C., and Smith, M. D(2016), Daily global mapping of Mars ozone column abundances with MARCI UV band imaging. Icarus, **266**, 112-133.

Guzewich, S. D., Lemmon, M., Smith, C. L., Martínez, G., de Vicente-Retortillo, Á., Newman, C. E,et al. (2019), Mars Science Laboratory observations of the 2018/Mars year 34 global dust storm. Geophysical Research Letters, **46**, 71– 79.

Guzewich, S. D., Smith, M. D., and Wolff, M. J (2014), The vertical distribution of Martian aerosol particle size. J. Geophys. Res., **119**, 2694-2708.

Haider, S. A., Abdu, M. A., Batista, I. S., Sobral, J. H., Luan, X., Kallio, E, et al. (2009b), D, E, and F layers in the daytime at high-latitude terminator ionosphere of Mars: Comparison with Earth's ionosphere using COSMIC data, J. Geophys. Res., **114**, 1-12,A03311

Haider, S. A., Batista, I. S., Abdu, M. A., Muralikrishna, P., Shah, S. Y., and Kuroda, T (2015), Dust storm and electron density in the equatorial D region ionosphere of Mars: Comparison with Earth's ionosphere from rocket measurements in Brazil. J. Geophys. Res., **120**, 8968-8977.

Haider, S. A., Siddhi, Y. S., Masoom, J.,and Bougher, S. (2019). Effect of dust storm and GCR impact on the production rate of O_3^+ in MY 28 and MY 29: Modeling and SPICAM observation. Journal of Geophysical Research: Space Physics, **124**, 2271–2282.

Haider, S. A., Sheel, V., Smith, M. D., Maguire, W. C., and Molina-Cuberos, G. J. (2010), Effect of dust storm on the D region of the Martian ionosphere: Atmospheric electricity, J. Geophys. Res., **115**, 1-10A12336.

Holmes, J. A., Lewis, S. R., Patel, M. R., and Lefèvre, F.(2018), First ozone reanalysis on Mars using SPICAM data. In: From Mars Express to ExoMars, 27-28 Feb 2018, Madrid.

Krasnopolsky, V. A (2006), Photochemistry of the martian atmosphere: Seasonal, latitudinal, and diurnal variations. Icarus, **185**, 153-170.

Lebonnois, S., Quémerais, E., Montmessin, F., Lefèvre, F., Perrier, S., Bertaux, J. L, et al. (2006), Vertical distribution of ozone on Mars as measured by SPICAM/Mars Express using stellar occultations. J. Geophys. Res., **111,** 1-15, E09S05.

Lefèvre, F., Bertaux, J. L., Clancy, R. T., Encrenaz, T., Fast, K., Forget, F, et al. (2008), Heterogeneous chemistry in the atmosphere of Mars. Nature, **454**, 971–975.

Lefèvre, F., Lebonnois, S., Montmessin, F., and Forget, F (2004), Three-dimensional modeling of ozone on Mars, J. Geophys. Res., **109**, 1-20, E07004,

Lindner B L (1988), Ozone on Mars: The effects of clouds and airborne dust, Planet. Space Sci. **36**, 125–144.

Martin, L.J. (1984), Clearing the Martian air: The troubled history of dust storms, Icarus, **57**, 317-321.

Martin, T.Z. (1995), Mass of dust in the Martian atmosphere, J. Geophys. Res., **100**, 7509–7512.

Millour, E., Forget, F., Spiga, A., Navarro, T., Madeleine, J. B., Pottier, A, et al. (2014), A new Mars climate database v5.1, paper 1301 presented at The Fifth International Workshop on Mars Atmosphere: Modeling and Observations, Oxford, U. K., Jan. 2014.

Montabone, L., Forget, F., Millour, E., Wilson, R. J., Lewis, S. R., Cantor, B, et al. (2015), Eight-year climatology of dust optical depth on Mars, Icarus, **251**, 65–95.

Montmessin, F., and Lefèvre, F (2013), Transport-driven formation of a polar ozone layer on Mars, Nature, **6**, 930-933.

Montmessin, F., Korablev, O., Lefèvre, F., Bertaux, J. L., Fedorova, A., Trokhimovskiy, A, et al. (2017), SPICAM on Mars Express: a 10 year in-depth survey of the Martian atmosphere, Icarus, **297**, 195-216.

Perrier, S., Bertaux, J. L., Lefèvre, F., Lebonnois, S., Korablev, O., Fedorova, A, et al. (2006), Global distribution of total ozone on Mars from SPICAM/MEX UV measurements J. Geophys. Res. Planets, **111**, 1-19, E09S06

Sheel, V., and Haider, S. A (2016), Long-term variability of dust optical depths on Mars during MY24–MY32 and their impact on subtropical lower ionosphere: Climatology, modeling, and observations, J. Geophys. Res., **121**, 8038-8054.

Smith, M. D., Wolff, M. J., Clancy, R. T., Kleinböhl, A., and Murchie, S. L (2013), Vertical distribution of dust and water ice aerosols from CRISM limb-geometry observations. J. Geophys. Res., **118**, 321-334.

Steele, L. J., Lewis, S. R., Patel, M. R., Montmessin, F., Forget, F., and Smith, M. D (2014). The seasonal cycle of water vapour on Mars from assimilation of Thermal Emission Spectrometer data. Icarus, **237**, 97–115.

❒❒❒

CHAPTER - 6

SCHUMANN RESONANCE AND CONDUCTIVITY

CONTENTS

The lightning discharge may be produced within dust storms or devils due to tribo-electricity. It is known that dust devils or storms occur on Mars and it is expected that lightning may be present within the dust devils on Mars. Whenever lightning discharge occurs, it emits low frequency electromagnetic waves, which is reflected from the ionosphere and give rise to SR in the cavity formed by the Martian surface and the ionosphere. To understand the SR modes in the non-homogeneous media within the cavity; we have solved the Maxwellian equations of electromagnetic waves, which oscillate within the cavity formed in the lower ionosphere of Mars between 0 km and 50 km. We have also calculated electrical conductivity and SR frequencies in the lower ionosphere of Mars, in the presence of a major dust storm that occurred in MY 25 at low latitude region (25^o-35^{o}S). The atmospheric conductivity is reduced by one to two orders of magnitude during the dust storm period. We have also found that the SR frequencies peak at ~18 km with values 19.9, 34.5 and 48.8 Hz at the modes N = 1, 2 and 3 respectively in the non-homogeneous medium. Our present results indicate that the practical/measurable values of SR are dependent on the altitudes. From our present work for the Mars cavity, we suggest that the lightning could occur in the accumulated dust layer at ~ 25-30 km altitudes. Our results can be useful to understand the altitude dependence of SR for Mars and also for any practical system to measure the SR in the ionosphere of Mars.

6.1 INTRODUCTION

The SR is characterized by propagation, reflection and resonance of electromagnetic wave in narrow dielectric layer between lithosphere and ionosphere of the planet. This narrow dielectric layer is a weak conducting layer surrounded spherically to form concentric cavity separated by surface and ionosphere. The ionosphere on Mars between 0 km and 200 km is produced by the impact of solar radiation during day time and solar wind proton-electron impact in the night time, meteoroid impact and GCR impact in presence and absence of dust storm (Pandya and Haider 2014, Haider et al 2013, Haider et al 2009b, 2010). The plasma at this altitude on Mars is providing strong conducting upper boundary of the cavity whereas lower conducting boundary is provided on the Martian surface. Martian surface-plate tectonic activity is not confirmed yet. Lithosphere activity may provide lower conducting boundary to reflect electromagnetic waves. Extremely low

Frequency (ELF) and Very Low Frequency (VLF) electromagnetic waves propagating in this concentric cavity are reflected from upper and lower conducting boundaries. The dust storm, interplanetary dust and dust devils have been observed in the lower atmosphere of Mars i.e. below 70 km of altitude. Due to electric discharge of these dust particles ionospheric ELF and VLF electromagnetic waves are produced. Some surface activity is also responsible to produce the static discharge and electromagnetic waves in the Martian cavity. The resonance of these standing normal modes in the cavity was measured and modelled by Schumann in 1952. Observations and modelling of SR have confirmed that the SR frequency is strongly depending upon atmospheric conductivity, ionospheric turbulence and surface activity on Mars (Molina-Cuberos et al 2002).

In this Chapter we have calculated SR frequency and atmospheric conductivity during dust storm of MY25 in the lower atmosphere of Mars at 25º-35ºS latitudes. Our results suggest that lighting could occur in the accumulated dust layer at lower altitudes. In addition, we have developed a prototype of Laboratory Experiment for Mars (LEMA) to measure the possible lightning on Mars from a future Orbiter. Our results can be useful to understand the altitude dependence of SR at Mars and also for any practical system to measure the SR in the ionosphere of Mars. The understanding of conductivity and SR frequency are necessary to describe the global circuit, aerosol-dust cloud interaction and their subsequent effects on the climate.

6.1.1 ELF and VLF radio wave production in the Cavity

The electromagnetic waves of ELF, 3 Hz to 3000 Hz and VLF, 3000 Hz to 30000Hz propagate in the cavity formed by planet surface and its ionosphere. The schematic diagram of ELF and VLF propagation is given in figure 6.1. The source of these ELF and VLF radio waves is classified into two categories (1) Natural source and (2) Artificial source (Alpert 1960; Budari 1999; Barr et al 2000).

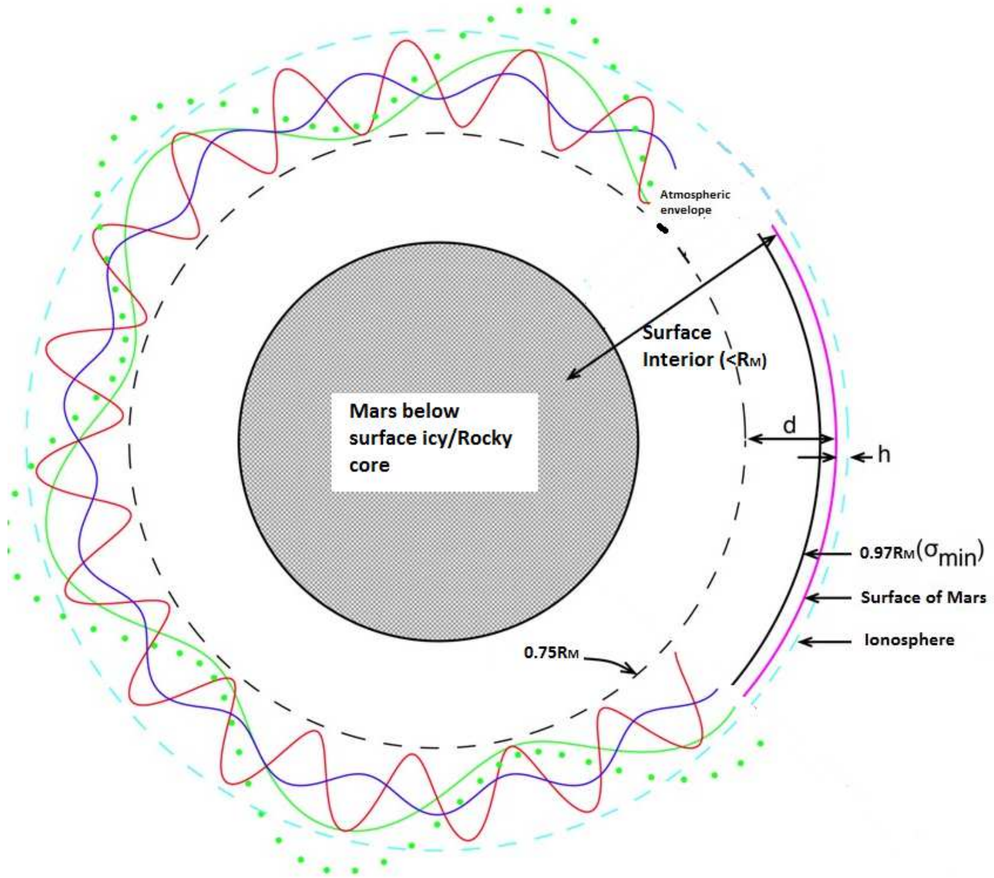

Figure 6.1 Schematic diagram of ELF and VLF propagation and SR in planetary surface-ionosphere cavity (Simoes et al., 2012).

6.1.2 Natural Source of ELF and VLF radio waves

Thunderstorm lightning on planets such as Earth and possibly on Mars produce ion discharge that result in the low frequency radio waves. Positive and negative ion discharge activity between thunder storm clouds and ionosphere produce lightning on these planets. This large scale electric discharge results in the production of low frequency radio waves. Volcanic eruptions and impact of massive meteorite produce upward flow of large dust devil and various gases which produce chemical reactions, ionizations and discharge in the atmosphere. These volcanic events are also responsible for the production of ELF and VLF radio waves. Tornadoes and dust devils are also responsible for production of these radio waves on planets like Mars, Jupiter and Venus. In the polar region of the Earth and at some extent on Mars aurora is observed which produce low frequency radio waves. This activity is known as Sprites. Along with the Sprites some activity of dim glow in the ionosphere is known as Elves that is also responsible for production of ELF and VLF signals. (Lyons et al., 2003; Fullekrog et al 2006).

6.1.3 Artificial source of ELF and VLF radio waves

The challenging issue in the Radio science research is to produce artificially ELF and VLF waves that can be obtained using extremely large antenna. The nuclear explosion produce strong artificial low frequency radio signals VLF with the frequency ~10-15 kHz (Glasstone 1962; Helliwell 1965). VLF and ELF radio waves propagation strongly depends on the ionosphere of the planets. The transient disturbance in the ionosphere due to solar flare impact on Earth and Mars directly affects reflection and attenuation of ELF and VLF wave. In turn this may result to the change in SR frequency (Bailey and Jones 1974; Burgess and Jones 1967). Galactic X-ray disturbance in radio wave propagation has yet to review hence the celestial X-ray sources may affect the long VLF paths (Edward et al., 1969; Bungess and Jones 1969, Svennessan et al., 1972). The strong source of perturbations in ELF and VLF are observed due to meteor showers and meteoric activity at lower altitude on Earth and Mars. On Mars, the absence of liquid water lead ELF waves to penetrate deep in the planetary surface and atmosphere. These perturbed ELF and VLF waves are used to explore the atmospheric conductivity and electricity in the lower atmosphere of Mars (Farrel and Desch 2001; Kozakiewicz et al 2016). The ELF and VLF waves propagate like wave guide in the cavity. The electric conductivity of ionosphere has significant influence on this radio wave propagation. Therefore the quasi stationary source of these radio waves affect cavity to produce resonance in the cavity known as SR (Kozakiewicz et al., 2016). ELF and VLF wave propagation and SR play an important role to calculate production and destruction rates of chemical compounds. Therefore, study of SR is useful to model chemistry of Martian atmosphere, global climate and possibilities of life.

6.2 SR AND PROPAGATION OF EM WAVES: IONOSPHERIC CONDUCTIVITY

The ionosphere of Mars has been understood mainly by the observed results of ion and electron density profiles. A cavity between lower ionosphere and the surface of Mars provide reflection and attenuation of Electro-magnetic (EM) waves of ELF and VLF.

These signals produce resonance in the cavity due to conducting effect of ionosphere and surface. The low frequency EM signals depend strongly on ionospheric conductivity (Greifinger and Greifinge 1978; Nickolaenko and Hayakawa 2002). Numerical models based on Transmission Line method (TLM) are used to study SR (Schuman, 1952; Molina-Cuberos et al 2006; Nickolanenko and Hayawa 2002).The ionospheric conductivity is calculated in the lower ionosphere of Mars (Molina-Cuberos et al., 2006; Haider et al., 2010; Haider and Mahajan, 2014). The conductivity depends on positive and negative ion densities and mobility. The formula for the calculation of the conductivity and SR frequency are described in brief in Section 6.3.1.

6.2.1 Formulation of SR frequency and conductivity

In the previous Sections we have discussed ELF and VLF propagation, the cavity of Mars surface-ionosphere in which resonance phenomena do occur due to wave propagation and reflection. According to Schumann (1952) the lowest resonant frequency of longitudinal EM waves can be written as

$$f_L \approx \frac{c}{2\pi\, R_M} \cdot N \tag{6.1}$$

where, c = velocity of light; R_M = Radius of Mars; N = number of modes ~1, 2, 3, ...

This resonance frequency is known as normal SR frequency. The same can be derived for transverse EM waves as,

$$f_N = \sqrt{N(N+1)} \cdot \frac{c}{2\pi\, R_M} \tag{6.2}$$

Where f_n is the SR frequency in normal mode of propagation, without considering the conductivity attenuation in the cavity (i.e., homogeneous medium). It is known as the normal SR frequency (Schumann, 1952; Nickolaenko and Hayakawa, 2002). The velocity of electromagnetic wave in free space is c (i.e. the velocity of light). This frequency is N-mode resonance frequency obtained in normal mode of propagation without considering conductivity attenuations at boundary. Therefore, it is known as normal Schumann Resonance (Schumann, 1952; Nickolaenko and Hayakawa, 2002; Jackson, 1999; Griffith, 1989). The equation of SR mode is given by Simoes et al. (2012) for the heterogeneous medium as

$$f_N \approx \frac{c}{2\pi \cdot R_M} \sqrt{N(N+1) \frac{\left(1 - {h}/{R_M}\right)}{\epsilon_r + i\left(\frac{\sigma}{\epsilon_0 \, 2\pi \cdot f'_N}\right)}} \tag{6.3}$$

In the present study we have used this equation to calculate normal SR frequency. We have calculated the SR frequencies for the modes N = 1, 2 and 3 from equation (6.3) in presence of high dust in the Martian troposphere. The f' is obtained from equation (6.2) in the vacuum. Radio wave propagation in the cavity and its reflection parameters strongly depend up on finite conductivity. The conductivity on Mars can be calculated using positive metallic and gaseous ions and neutrals which result in to total conductivity σ_{total} in the ionosphere of Mars.

$$\sigma_{total} = e\mu\left(\sum \rho^+ + \sum \rho^-\right) \tag{6.4}$$

where μ is the mean ion mobility, e is elementary charge, ρ^+ and ρ^- are positive and negative ion densities in the lower ionosphere of Mars respectively. Using formula of

Michael et al. (2007) the mean ion mobility is calculated to be ~ 0.02 $m^2\ V^{-1}s^{-1}$. We have taken the positive and negative ion densities from Sheel and Haider (2016) in the presence of high dust. In the above model, we have considered two spherical perfectly conducting layers. The surface forms the lower layer and upper layer is taken as 70 km from where the electromagnetic waves are reflected.

6.2.2 Ionospheric conductivity: Model results

We have calculated the atmospheric conductivities between 0 km and 50 km due to GCR impact ionization in the nighttime ionosphere of Mars, in the presence and absence of dust storm which are presented in figure 6.2. The blue line with square represent the ion conductivity profile calculated by us for MY 25 during dust storm at τ = 1.7 and Ls = 210^o at low latitude range (25-35^{o}S). The ion conductivity profile given by Molina-Cuberos et al. (2006) in absence of dust storm represent by pink line with triangle. The red dotted line with circle, blue line with star and brown dotted line represent the ion conductivities estimated by Cardnell et al. (2016) in the presence of high dust, standard dust and low dust at τ = 1.7, 0.5 and 0.1, respectively at Ls = 244^o. Our calculated conductivity matches within factor of 1.5 - 2 with the estimated profile of Cardnell et al. (2016) during high dust condition. Our conductivity results near the surface level is ~ 1-3 $\times$ 10^{-13} $Ohm^{-1}\ m^{-1}$ and it has a peak value of ~ 3.5 $\times$ 10^{-12} $Ohm^{-1}\ m^{-1}$ in the presence of high dust at ~ 25 km altitude. The values of conductivities are decreasing with increasing dust loading in the atmosphere. The electrical conductivities are reduced by 1-2 orders of magnitude due to the impact of low dust, standard dust and high dust in the troposphere of Mars. Our calculated conductivity at peak altitude is lowered by ~2 orders of magnitude than that estimated by

Molina-Cuberos et al. (2006) in the absence of dust. Molina-Cuberos et al. (2006) and Cardnell et al. (2016) has not found clear peak in their modelled conductivities.

The atmospheric density and the pressure close to the surface of Mars are nearly same as those in the Earth's stratosphere at altitudes from 35 - 40 km. The conductivity in the Earth's stratosphere has been calculated to be ~ 10^{-12}-10^{-10} Ohm^{-1} m^{-1} (Singh et al., 2004), which is similar to that estimated by us and other investigators in the absence of dust or low dust condition (e.g. Molina-Cuberos et al., 2006; Cardnell et al., 2016) near the surface of Mars at an equivalent atmospheric pressure. The ion-neutral collision frequency is very large in the Martian troposphere (Michael et al., 2007).Therefore, convection force will be ineffective and the ions cannot move due to influence of ambient electric field.

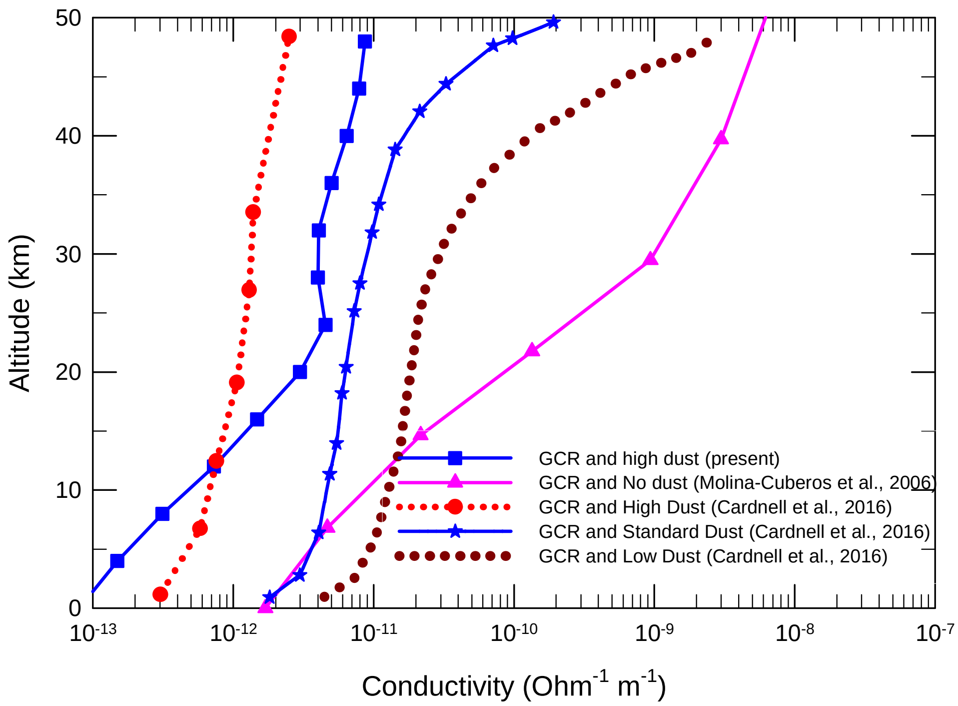

Figure 6.2 Comparison of ionospheric conductivities between present and other model calculations carried by Molina-Cuberos et al., 2006 and Cardnell et al., 2016.

6.2.3 Dust loading on conductivity

The aerosol particles can move in the troposphere due to the influence of gravity field. These aerosol particles can interact with the light ions of atmosphere during their movement. This process produces electric fields several times larger than the electric fields produced by elementary charges during the dust storm period. The production of large electric fields and its associated electric discharges are responsible for the occurrence of lightning during the dust storm period on Mars (Tolendo-Redondo et al., 2017). The heavy loss of ions occurred in presence of high dust. This is evident from figure 6.2 that the conductivity decreases with increasing dust opacity. The conductivity in the presence of high dust is calculated to be ~10^{-13} Ohm^{-1} m^{-1}at the surface of Mars. The conductivity increases with altitude in the troposphere-stratosphere region of Mars. The atmosphere of Mars consists of troposphere and isothermal stratosphere-mesosphere in the lower atmosphere of Mars. Unlike in the Earth's atmosphere, there is no warming in the stratosphere of Mars due to presence of very low ozone. The temperature in the Martian troposphere is ~ 180^{o} K. The main source of ionization in the troposphere-stratosphere of Mars is the GCR.

The global and regional dust storms have been reported on Mars since four decades. Mariner 9 observed first major dust storm on 22 September, 1971 in southern Noachi's Terra region (Martin, 1984). Later Viking observed two major dust storms in Thaumasia Fossae and Valles Marineris on February 22 and June 5, 1977 respectively (Ryan and Sharman, 1981). During these dust storm periods, the optical depths were increased to about 1.5 to 2.6. After 20 Earth years, Mars Global Surveyor and Mars Odyssey provided regular measurements of dust storms. The onset of the storm occurred on 26 June 2001 in southern mid-to low latitudes in Hellas basin (Ogohara and Satomura, 2008). This dust storm spread in all the directions over the entire planet. The temporal changes in the dust opacity are reported by Cantor (2007) and Michael and Tripathi (2008) in presence of this storm. They reported maximum value of $\tau = 5$ in Hellas basin at Ls = 199.5^o. Later this storm reached in Elysium and Claritas where τ were estimated to be 3.7 and 3.8 at Ls = 211.1^o and Ls = 206.6^o respectively. Recently Sheel and Haider (2016) estimated positive and negative ion densities using τ = 1.7, 1.2, 0.5 and 0.1 at Ls = 210^o, 280^o, 220^o and 150^o respectively. Cardnell et al. (2016) calculated atmospheric conductivity for three different cases of τ = 1.7, 0.5 and 0.1 at Ls = 244^o. The SR frequencies were estimated by Molina-Cuberos et al. (2006) and Toledo-Redondo et al. (2017).

6.3 CALCULATION OF SR FREQUENCY

We have plotted altitude profiles of SR frequencies in figure 6.3 for the modes N = 1, 2 and 3 during MY 25 at low southern latitude region (25-35^{o}S) in the presence of dust storm at τ = 1.7 and Ls = 210^o. The SR frequencies vary with altitude due to the change in electrical conductivity profile. The maximum SR frequencies for the modes N = 1, 2 and 3 occur at ~ 18 km with values 19.9, 34.5 and 48.8, respectively. The lightning can occur in the night time atmosphere of Mars at the maximum frequencies during the high dust storm period. Guzewich et al. (2014) and Heavens et al. (2014) observed two distinct layers in the dust profiles at altitude range ~ 20-30 km and ~ 45-65 km from the Compact Reconnaissance Imaging Spectrometer (CRISM) and Mars Climate Sounder (MCS) on board the Mars Reconnaissance Orbiter (MRO) (Wolff et al., 2009). These two layers suggest that the dust is accumulated in the lower atmosphere at low altitude (20-30 km) and high altitude (45-65 km) regions. Between these two dust layers, the lightning can occur due to ion-aerosol attachment processes. In our model, we have considered the upper layer of the cavity at 70 km therefore, the maximum conductivity and maximum SR frequency occur near the low altitude layers of the dust (≤ 30 km) in the D region ionosphere of Mars.

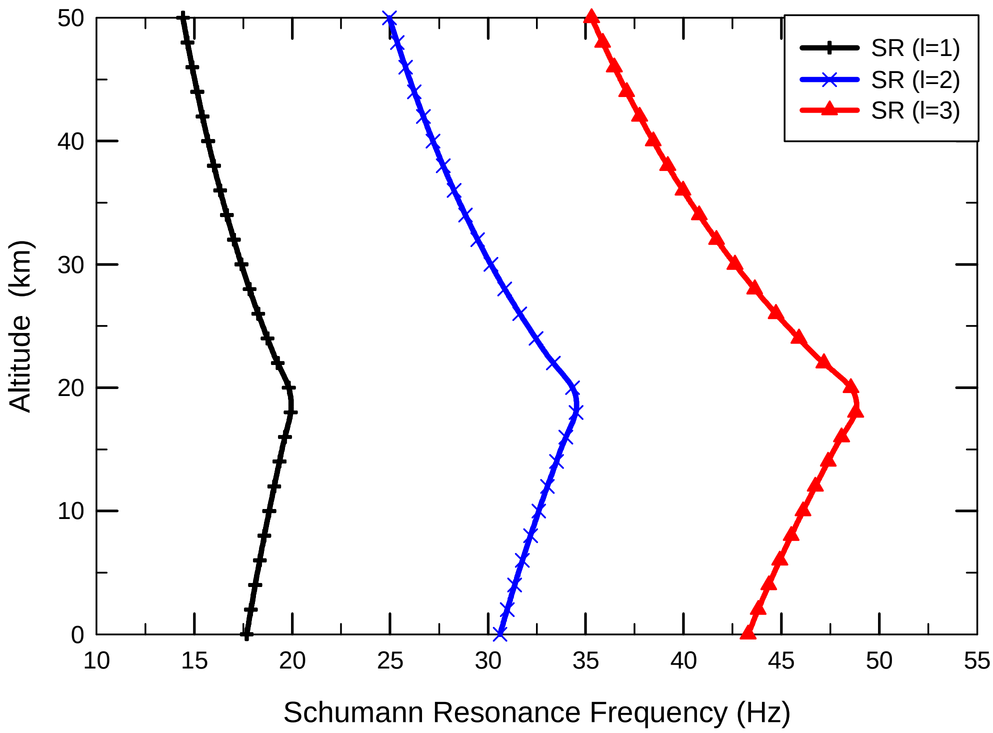

Figure 6.3 Altitude profiles of Schumann Resonance frequency in the night time ionosphere of Mars in MY 25 during high dust storm (τ = 1.7) at low latitude region (25-35°S).

6.3.1 Comparison of estimated SR frequency with other model results

The SR frequency at high altitude layers can be produced due to different physical processes of the ionosphere. The discussion of the upper layer is beyond the scope of this work. Using the TLM method, Molina-Cuberos et al. (2006) and Toledo-Redondo et al. (2017) calculated the SR frequencies for Mars. Molina-Cuberos et al. (2006) estimated SR frequencies 19.6, 33.9 and 48.5 Hz for the modes N = 1, 2 and 3 respectively. Our results are in good agreement with their estimated values. Toledo-Redondo et al. (2017) calculated the SR frequencies to be 11 Hz, 12.5 Hz and 15.5 Hz at low dust, standard dust and high dust conditions respectively for N = 1. For modes N = 2 and N = 3, these frequencies were increased by factors of ~ 2 and ~3 respectively. Our estimated values of SR are higher from Toledo-Redondo et al. (2017) by a factor of 1.6 because of following reasons: (1) it may be due to the use of different boundary layers of cavity between two calculations. We have assumed cavity boundary from 0 to 70 km, while Toledo-Redondo (2017) used cavity boundary from 0 to 130 km, including two additional layers created by meteoric ablation at 80-90 km and solar wind electron-proton impact ionization at 120 km (Haider et al., 2013), (2) Toledo-Redondo et al. (2017) modelled the conductivity using neutral atmosphere for dust storm scenario (τ = 1.7) from MCD (Millour et al., 2014). In our model, the dust density profile is calculated at τ = 1.7 (Haider et al., 2015; Sheel and Haider, 2016) in the chemical model self consistently, and (3) both model calculations are carried out at different locations of Mars. We have run our model in MY 25 at low southern latitude range (25-35^{o}S) during major dust storm period, while Toledo-Redondo et al. (2017) calculated SR frequencies at ExoMars landing site, which is different from that of present work.

6.3.2 Proposed instrument for lightning on Mars

There are no measurements of lightning on Mars from an orbiter around it, though it is expected there due to dust devils present. In our group an instrument, called LEMa is being developed to measure the lightning on Mars from a future Mars mission. The low frequency electromagnetic waves generated by the lightning on Mars can be captured by the LEMa instrument. Figure 6.4 shows a block diagram of LEMa in which the EM waves generated due to lightning is impinging on a 'V' antenna. The out-of-band signals, if any, are removed by a filter and then signal is given to a preamplifier. Since the signal levels would be varying at orbital altitudes, an Automatic Gain Control (AGC) is essential for equalization of the signals of various frequencies. It is then passed to a high speed Analog-to-Digital (ADC) converter, which samples the signal at sufficiently large sampling rates (e.g. 4-5 times the highest frequency component). The raw data is processed in a digital processor and a filter bank spectrometer separates signal levels in various signal bands. Essentially, it provides the lightning spectrum data having information of spectral amplitudes. The payload is interfaced with a satellite sub-system, where the payload data and health parameters are sent or transmitted to Earth at later time. Raw power from the satellite would be converted into a regulated supply using DC-DC converter.

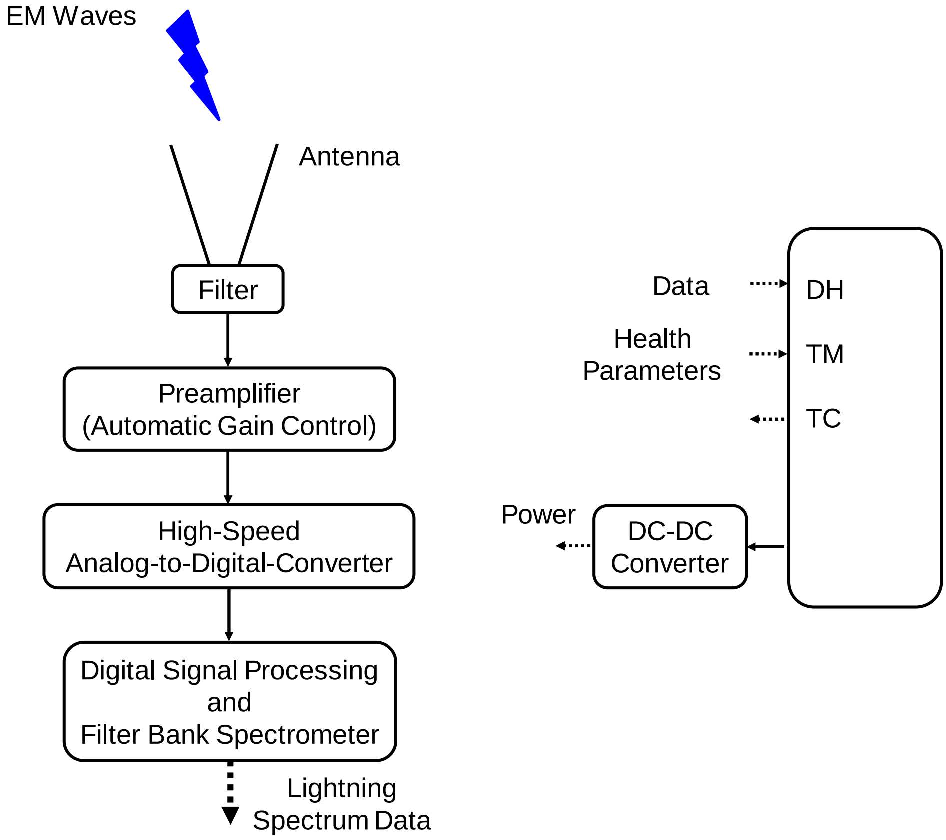

Figure 6.4 Block diagram of LEMa experiment for proposed Mars mission to detect lightning.

The LEMa can provide consistent observations of lightning over the mission life through the study of simultaneous frequency components generated by the lightning. The frequency of occurrence of lightning as well as the electromagnetic properties of dust devils could be studied better using such dedicated instrument on the orbiter.

6.3.3 Proposed instrument for measuring dust on Mars

It is known that dust devils prevail near the Mars surface and cause the erosion of dust layers. The second source of dust in Martian atmosphere is secondary ejecta, caused by the impacts on Martian Moons. The third possible source is the levitation of charged dust particles from the Moons. The escaping dust is expected to form a ring or torus around the Mars. However, no such dust rings have been detected to the present day. To study origin, abundance, distribution and seasonal variation of Martian dust, a Mars Orbit Dust Experiment (MODEX) is proposed for future Mars orbiter (Pabari et al., 2018). In order to measure the Martian dust from a future orbiter, the design of a prototype of an impact ionization dust detector has been initiated. Whenever a dust particle strikes on metal (gold) target of dust detector, plasma cloud is generated, which is separated into electrons and ions using voltage biased collector plates. A third channel is added to distinguish impact signals from noise. Pulse generated by dust particle impact is processed by the electronics to measure its rise time and maximum charge, which are used to find the mass and velocity of incoming particles. Further, particle flux and distribution between Earth and Mars and around Mars can be studied using this detector.

❒❒❒

REFERENCES

Al'pert, Ya. L (1960), Radio Wave Propagation and the Ionosphere, Consultants Bureau, New York.

Bailey, R. C., and Jones, T. B (1974), The accuracy and resolution of model ionospheres derived from VLF propagation parameters, J. Atmos. and Terr. Phys., **36**, 1059-1069.

Barr, R., Jones, D. L., and Rodger, C. J (2000), ELF and VLF radio waves, J. Atmospheric and Solar-Terr. Phys., **62**, 1689-1718

Buderi, R (1999), The Invention that Changed the World. The Story of Radar from War to Peace, Little, Brown and Company, London.

Burgess, B. and Jones, T. B (1967), Solar flare effects and VLF radio wave observations of the lower ionosphere, Radio Science, **2**, 619-626.

Burgess, B. and Jones, T.B (1969), Search for the effect of stellar X-rays on the nighttime lower ionosphere, Nature **224**, 680-681.

Cantor, B. A (2007), MOC observations of the 2001 Mars planet-encircling dust storm, Icarus **186**, 60-96.

Cardnell, S., Witasse, O., Molina-Cuberos, G. J., Michael, M., Tripathi, S. N., Déprez, G, et al. (2016), A photochemical model of the dust loaded ionosphere of Mars. J. Geophys. Res. **121**, 2335-2348.

Edwards, P. J., Burtt, G. J., and Knox, F (1969), Ionospheric effects caused by Celestial X-rays, Nature **222**, 1053-1054.

Farrell, W. M., and Desch, M. D (2001), Is there a Martian atmospheric electric circuit? J. Geophys. Res. **106**, 7591-7595.

Füllekrug, M., Mareev, E. A., and Rycroft, M. J (2006), Sprites, elves and intense lightning discharges, vol. **225**, Springer.

Glasstone, S (1962), The effects of nuclear weapons. In: Glasstone, S. (Ed.), U.S. Department of Defence | U.S. Atomic Energy Commission, Washington, DC

Greifinger, C., and Greifinger, P (1978), Approximate method for determining ELF eigenvalues in the Earth-ionosphere waveguide, Radio Sci., **13**, 831-837.

Griffith, J. D. (1989), Introduction to Electrodynamics, 2nd Edition, Printice-Hall pub.,USA

Guzewich, S.D., Smith, M. D., Wolff, M. J (2014), The vertical distribution of Martian aerosol particle size, J. Geophys. Res., **119**, 2694-2708.

Haider, S. A., Batista, I. S., Abdu, M. A., Muralikrishna, P., Shah, S. Y., and Kuroda, T (2015), Dust storm and electron density in the equatorial D region ionosphere of Mars: Comparison with Earth's ionosphere from rocket measurements in Brazil. J. Geophys. Res., **120**, 8968-8977.

Haider, S. A., Abdu, M. A., Batista, I. S., Sobral, J. H., Luan, X., Kallio, E, et al. (2009b), D, E, and F layers in the daytime at high-latitude terminator ionosphere of Mars: Comparison with Earth’s ionosphere using COSMIC data, J. Geophys. Res., **114**, 1-12,A03311

Haider, S. A.and Mahajan, K. K (2014), Lower and upper ionosphere of Mars, Space Science Reviews, **182**, 19-84.

Haider, S. A., Pandya, B. M., and Molina-Cuberos, G. J (2013), Nighttime ionosphere caused by meteoroid ablation and solar wind electron-proton-hydrogen impact on Mars: MEX observation and modeling, J. Geophys. Res., Space Physics, **118**, 6786-6794.

Haider, S. A., Sheel, V., Smith, M. D., Maguire, W. C., and Molina-Cuberos, G. J. (2010), Effect of dust storm on the D region of the Martian ionosphere: Atmospheric electricity, J. Geophys. Res., **115**, 1-10A12336.

Heavens, N. G., Johnson, M. S., Abdou, W. A., Kass, D. M (2014), Seasonal and diurnal variability of detached dust layers in the tropical Martian atmosphere, J. Geophys. Res., **119**, 1748-1774.

Helliwell, R.A (1965), Whistlers and Related Ionospheric Phenomena. Stanford University Press, Stanford.

Jackson, J. D (1999), Classical Electrodynamics, John Wiley and Sons, Hoboken, pp. 808.

Kozakiewicz, J., Kulak, A., Kubisz, J., and Zietara, K (2016), Extremely Low Frequency Electromagnetic Investigation on Mars, Earth Moon Planets,**118,** 103–115

Lyons, W. A., Nelson, T. E., Armstrong, R. A., Pasko, V. P., and Stanley, M. A (2003), Upward electrical discharges from thunderstorm tops, Article in "American meteorological society,**84**, 445-454

Martin, L. J (1984), Clearing the Martian air: The troubled history of dust storms. Icarus **57**, 317-321.

Michael, M. andTripathi, S. N (2008), Effect of charging of aerosols in the lower atmosphere of Mars during the dust storm of 2001. Planet. Space Sci. **56**, 1696-1702.

Michael, M., Barani, M. and Tripathi, S. N (2007), Numerical predictions of aerosol charging and electrical conductivity of the lower atmosphere of Mars, Geophys. Res. Lett. **34**, 1-5, L04201.

Millour, E., Forget, F., Spiga, A., Navarro, T., Madeleine, J. B., Pottier, A, et al. (2014), A new Mars climate database v5.1, paper 1301 presented at The Fifth International Workshop on Mars Atmosphere: Modeling and Observations, Oxford, U. K., Jan. 2014.

Molina-Cuberos, G. J., Morente, J. A., Besser, B. P., Portí, J., Lichtenegger, H., Schwingenschuh, K, et al. (2006), Schumann resonances as a tool to study the lower ionospheric structure of Mars, Radio Sci., **41**, 1-8, RS1003.

Molina-Cuberos, G. J., Lichtenegger, H., Schwingenschuh, K., López-Moreno, J. J., and Rodrigo, R (2002), Ion neutral chemistry model of the lower ionosphere of Mars. J. Geophys. Res **107**, 3-1 E5.

Nickolaenko, A. P., and Hayakawa, M (2002), Resonances in the Earth-Ionosphere Cavity, Kluwer, Dordrecht, **19**, 380.

Ogohara, K., and Satomura, T (2008), Northward movement of Martian dust localized in the region of Hellas Basin, Geophys. Res. Lett., **35**, 1-6, L13201.

Pabari, J. P., Haider, S. A., Pandya, B. M., Singh, R. K., Kumar, A., Patel, D. K, et al. (2018), Orbital altitude dust at Mars, its implication and a prototype for its detection, Planet. Space Sci., **161**, 68-75.

Pandya, B. M and Haider, S. A (2014), Numerical simulation of the effects of meteoroid ablation and solar EUV/X-ray radiation in the dayside ionosphere of Mars: MGS/MEX observations, J. Geophys. Res. **119**, 9228-9245.

Ryan, J. A and Sharman, R. D (1981), Two major dust storms, one Mars year apart: Comparison from Viking data, J. Geophys. Res. **86,** 3247-3254.

Schumann, W. O (1952), On the radiation free self-oscillations of a conducting sphere which is surrounded by an air layer and an ionospheric shell Z. Naturforschung Teil A. **7**, 149-154.

Sheel, V and Haider, S. A (2016), Long term variability of dust optical depths on Mars during MY24-MY32 and their impact on subtropical lower ionosphere: Climatology, modeling, and observations, J. Geophys. Res,**121**, 8038-8054.

Simões, F., Pfaff, R., Hamelin, M., Klenzing, J., Freudenreich, H., Béghin, C, et al. (2012), Using Schumann resonance measurements for constraining the water abundance on the giant planets-implications for the solar system's formation. Astrophys. J. **750**(1), 85.

Singh, D.K., Singh, R.P. and Kamra, A. K (2004), The electrical environment of the Earth’s atmosphere: A review. Space Sci. Rev. **113**, 375-408.

Svennesson, J., Reder, F., and Crouchley, J (1972), Effects of X-ray stars on VLF signal phase. J. Atmospheric and.-Terr. Phys, **34**(1), 49-72.

Toledo-Redondo, S., Salinas, A., Portí, J., Witasse, O., Cardnell, S., Fornieles, J., et al. (2017), Schumann resonances at Mars: Effects of the day-night asymmetry and dust loaded ionosphere, Geophys. Res. Lett., **44**, 648-656.

Wolff, M. J., Smith, M. D., Clancy, R. T., Arvidson, R., Kahre, M., Seelos, F, et al. (2009), Wavelength dependence of dust aerosol single scattering albedo as observed by the Compact Reconnaissance Imaging Spectrometer. J. Geophys. Res, Planets, **114**, 1-17, E00D04.

❒❒❒

CHAPTER - 7

SUMMARY AND CONCLUSION

In Chapter 1 we have described lower and upper ionosphere, chemistry, ion-dust reactions and chemical models used in the present thesis. The chemistry of the lower and upper ionosphere of Mars is different. Three body reactions are very important in the lower ionosphere of Mars. In the upper ionosphere two body reactions are important only. We have also described the chemistry of the lower and upper ionosphere of Mars. We have also described altitude profiles of the neutral densities of various gases in the lower and upper atmosphere of Mars. The dust aerosols are contributing very much in the chemistry of the lower ionosphere.

In Chapter 2 we have described methodology used in present thesis. We have used energy loss method, continuity equation, and AYS model to study the electron energy degradation processes in the Martian ionosphere. By using AYS we have calculated photoionization rates, photoelectron impact ionization rates of atmospheric gases, and photoelectron flux in the upper ionosphere of Mars. We have also used energy loss model to calculate production rates of atmospheric ions in the lower ionosphere of Mars. Using these production rates densities of ions and electrons are calculated at different altitudes in the lower and upper ionosphere of Mars.

In Chapter 3 we have described the effects of solar X-ray flares in D region ionosphere of Mars on 6 April, 2001 and on 17 March, 2003. The responses of these flares were also observed in the Earth's ionosphere by a Digisonde at College AK (64.9^{o}N, 212^{o}E). The plasma frequencies f_{min} observed by a Digisonde in the D region of Earth's ionosphere are compared with that obtained from the IEC of D region of Mars' ionosphere on 6 April, 2001 and 17 March, 2003 at nearly same location. In comparing these results at flare time we found that the f_{min} of D region of Earth's ionosphere increased by factors of ~ 2-5 while IEC of D region of Mars' ionosphere increased by factors of ~7.We have estimated the non-flare and flare electron density, positive and negative ion density profiles on both days. In non-flare and flare electron density profiles of Mars' ionosphere, the D region peaks are produced at altitude range of 25-30 km due to impact of hard X-rays (0.5-3 Å). The D peak is also produced at 25 km due to impact of GCR in the Martian ionosphere. The D peak density produced by GCR is lower by one and two orders of magnitude than that produced by the hard X-rays in the non-flare and flare electron density profiles respectively.

In Chapter 4 we have studied 32 electron density profiles affected by solar flares that were observed by MGS in E region ionosphere of Mars. We have estimated % increases in IEC in the E region ionosphere of Mars. The E-peak electron production rates are calculated for each flare day. The variations of E-peak electron production rates with season are fitted by a sinusoidal function. We have also studied the implications of solar X-ray flares on the habitability of all kinds of human to micro-organisms. Among all 32 flares, 15 April, 2001(X14.4) is a strong flare that gives highest dose ~ 0.1 Gy, which is lethal to human risk in Mars' space. The ion and electron densities of flare events were also estimated. It is found that our theoretical model results of electron densities are larger by a factor of ~ 2-3 than the MGS measurements. However, our calculated electron densities are matching well with other model results.

In Chapter 5 we have developed a seasonal dependent energy loss model due to impact of GCR for the calculation of ion production rate of O_3^+ at different altitudes and latitudes between Ls = 0^o-360^o in MY 28 and MY 29. At low latitude the production rate of O_3^+ shows a broad peak between altitudes 30 km and 40 km. The peak production rates are increasing up to Ls = 47.5^o and then stabilized at about 2 x 10^{-8} cm^{-3} s^{-1}. At Ls ≥ 47.5^o the peak production rate of O_3^+ starts decreasing until it disappeared after Ls = 127.5^o. We also represent the seasonal variability of ozone column density obtained from SPICAM observation during the daytime. These observation are compared with the daytime MCD model (Millour et al., 2014). At mid-to high latitudes ozone column density is maximum in northern winter and minimum in southern summer. A major dust storm occurred in MY 28 at Ls ~ 280^o in southern latitudes (~25^o-35^{o}S). During the dust storm period, dust opacity, ozone column density and O_3^+ production rate on the surface of Mars were increased by a factor of ~3.

In Chapter 6 we have calculated SR frequency and conductivity in the nighttime ionosphere of Mars during dust storm of MY 25 at low latitude region (25-35^{o}S). Our results suggest that the atmospheric conductivity is reduced by one to two orders of magnitude in the presence of dust storm period. It represents a small dust layer at about 25-30 km altitudes. We estimated SR frequencies peak at ~18 km with values 19.9, 34.5 and 48.8 Hz at the modes N = 1, 2 and 3 in the non-homogeneous medium. We have also found that the lightning could occur in the accumulated dust layer at ~ 20-30 km altitudes.

❒❒❒

CHAPTER - 8

FUTURE WORK

The ion neutral chemistry of lower Martian ionosphere is more complex than any other ionospheric regions. The water cluster ions are important in the lower ionosphere of Mars. Since water vapor changes with latitude and season, we want to study the variation of water vapor in lower ionosphere of Mars. We will also study the effect of dust on water vapor in Martian ionosphere.

Sulfur dioxide (SO_2) in the atmosphere is trace spices of current volcanic activity. It has become especially interesting due to the long-standing controversy of methane on Mars. If volcanoes have been active in recent Martian history, it would be expected to find SO_2 together with methane in the current Martian atmosphere (Krasnopolsky., 2012). No SO_2 has been detected, however, NASA Goddard Space Flight Center reported detection of SO_2 in Rocknest soil samples analyzed by the Curiosity rover in March 2013 (McAdam et al., 2013). NASA's Curiosity rover has also measured the highest level of methane (CH_4) gas ever found in the atmosphere at Mars's surface. Curiosity has measured methane many times since it landed in Gale Crater in 2012. The level is typically low, often in the parts per trillion range, and seems to rise and fall as Martian seasons change. Despite observations of methane and sulfur in the Martian atmosphere, our knowledge of the distribution of this trace species in the atmosphere has still not reached a mature stage. This can filled by theoretical modeling of methane and sulfur chemistry and compare it with observations. Therefore we will develop a model to by using the sulfur and methane photochemistry to understand its distribution and seasonal variability in Martian ionosphere. The knowledge of the complete ionosphere of Mars is very important for the future Mars mission.

MARSIS aboard the Mars Express spacecraft observes the reflections from normal ionosphere in nadir direction and those from the ionization bulges in oblique directions. It observed few events on orbits 4425, 4447, 4469, and 4513 on 15 June, 21 June, 28 June and 10 July 2007 of extremely strong electron densities at low altitudes in the dayside lower ionosphere of Mars (Venkateswara Rao et al., 2019). Observation of such strong densities at such low altitudes is unusual and demands a source mechanism. We can assume that a solar flare along with the Solar Energetic Particle (SEP) can account together for such strong ionization. For this purpose, we will modelled the electron density profiles using coupled continuity and yield spectrum methods. We will also calculate the ionization rates due to impact of photon, photoelectron and SEP in the dayside atmosphere of Mars.

❒❒❒

REFERENCES

Krasnopolsky, V. A (2012), Search for methane and upper limits to ethane and SO2 on Mars. Icarus, **217**, 144-152.

McAdam, A., Franz, H., Archer Jr, P., Freissinet, C., Sutter, B., Glavin, D, et al. (2013), Insights into the Sulfur Mineralogy of Martian Soil at Rocknest, Gale Crater, Enabled by Evolved Gas Analyses.

Venkateswara Rao, N., Leelavathi, V., Mohanamanasa, P., Haider, S. A., and Rao, S. V. B (2019), Enhanced ionization in magnetic anomaly regions of the Martian lower ionosphere associated with dust storms. J. Geophys. Res., Space Physics, **124**, 3007-3020.

❒❒❒

PUBLICATIONS

Effect of Dust Storm and GCR Impact on the Production Rate of O_3^+ in MY 28 and MY 29: Modeling and SPICAM Observation

S. A. Haider[1], Y. S. Siddhi[1,2], J. Masoom[1,2], S. Bougher[3]

[1]Planetary Sciences Division, Physical research Laboratory, Ahmedabad, India

[2]Research Scholar, Faculty of Science, Pacific Academy of Higher Education of ResearchUniversity, Udaipur, India

[3]Climate and Space Sciences and Engineering, University of Michigan, Ann Arbor, USA

ABSTRACT

We have developed a seasonally dependent energy loss model to calculate the zonally averaged production rates of O_3^+ due to impact of galactic cosmic rays in the dayside troposphere of Mars between solar longitudes (Ls) ~0° and 360° at low latitudes (2°N, 2°S, 25°N, and 25°S), mid-latitudes (45°N and 45°S), and high latitudes (70°N and 70°S) in the Martian Year (MY) 28 and MY 29. We also represent the seasonal variability of zonally averaged ozone column density obtained from Mars Climate Database (MCD; Millour et al., 2014, https://hal.archives-ouvertes.fr/hal-01139592) during the daytime. These results are compared with the daytime observations of column ozone made by Spectroscopy for the Investigation of the Characteristics of the Atmosphere of Mars onboard Mars Express (MEX). At mid-to-high latitudes ozone column density is maximum in northern winter and minimum in southern summer. At low-to-middle latitudes (2°N–S, 25°N–S, and 45°N–S), the production rates of O_3^+ represent a broad peak between altitudes 26 and 45 km in both hemispheres. The peak production rates are increasing up to Ls = 47.5° and then stabilized at about 2.5×10^{-8} cm^{-3}/s. At Ls ≥ 47.5° the peak production rate of O_3^+ starts decreasing until it disappeared after Ls = 127.5°. A major dust storm occurred in MY 28 at Ls~280° in southern latitudes (~25°–35°S). During the dust storm period, dust opacity, ozone column density, and O_3^+ production rate on the surface of Mars were increased by a factor of ~3.

Published in: Journal of Geophysical Research: Space Physics, **124**, 2271–2282(2019), ISSN: 2169-9402

Schumann resonance frequency and conductivity in the nighttime ionosphere of Mars: A source for lightning

S. A. Haider[1], Jayesh P. Pabari[1], J. Masoom[1,2] and Siddhi Y. Shah[1,2]

[1]Planetary Science Division, Physical Research Laboratory, Ahmedabad, India

[2]Research Scholar, Faculty of Science, Pacific Academy of Higher Education and Research

University, Udaipur, India

ABSTRACT

We have solved the Maxwellian equations of electromagnetic waves which oscillate within the cavity formed in the lower ionosphere of Mars between 0 and 70 km. The electrical conductivity and Schumann Resonance (SR) frequencies are calculated in the lower ionosphere of Mars, in the presence of a major dust storm that occurred in Martian Year (MY) 25 at low latitude region (25^{o}–35^{o}S). It is found that the atmospheric conductivity reduced by one to two orders of magnitude in the presence of a dust storm. It represents a small dust layer at about 25–30 km altitudes where lightning can occur. We also found that the SR frequencies peak at ~18 km with values 19.9, 34.5 and 48.8 Hz for the modes l = 1, 2 and 3, respectively, in the non-homogeneous medium. Our results indicate that practical or measurable values of SR are dependent on the altitudes.

Published in: Advances in Space Research, **63**, 2260-2266 (2019),
ISSN: 0273-1177

Characteristics of solar X-ray flares and their effects on the ionosphere and human exploration to Mars: MGS radio science observations

P. Thirupathaiah[a,1], Siddhi Y. Shah[a,b], S.A. Haider[a,*]

[a]Planetary Sciences Division, Physical Research Laboratory, Ahmedabad, India

[b]Faculty of Science, Pacific Academy of Higher Education and Research University, Udaipur, India

ABSTRACT

Responses of solar X-ray flares were observed in a layer of the Martian ionosphere at altitudes of ~110 km from 32 electron density profiles obtained by radio science experiment onboard Mars Global Surveyor (MGS) during solar cycle 23. Of the 32 profiles recorded during flare periods, 10 were associated with X-class flares, 12 with M class and 10 with C class flares. The flare E-peak densities vary with solar X-ray flux, Solar Zenith Angle (SZA), Solar Longitude (Ls) and latitudes. Ionospheric Electron Content (IEC) and E-peak electron production rates of these flare profiles are estimated in the E region ionosphere. We found a maximum increase of ~200%, ~140% and ~90% in the time series of IEC for X, M and C class flares respectively. The dependence of flare E-peak electron production rate with Ls is fitted by a sinusoidal function. We have also calculated biological doses ~0.1-1.0×10^{-1}, 1-8×10^{-3} and 1-6×10^{-4}Gy for X, M, C class flares respectively to study the human risk for exploration to Mars. Among 10 X-class flares X1 is a strong solar flare that gives highest dose, which is potentially lethal for human risk in Mars' space.

Published in: Icarus, **330**, 60-74 (2019),
ISSN: 0019-1035

Presentations in Conference/Symposium

1 Model calculation of production rate of H_2O and O_3 on lower atmosphere of Mars: Seasonal Variability

Siddhi Y. Shah, S. A. Haider

Date: 9-12 February, 2016

Organizer: 19th National Space Science Symposium held at Space Physics Laboratory, Vikram Sarabhai Space Center, Thiruvananthapuram.

2 Effect of Solar flares on ionosphere of Mars

Siddhi Y. Shah, S. A. Haider

Date: 8-10 November, 2017

Organizer: Brain Storming Session on Vision and Explorations for Planetary Sciences in Decades 2020-2060, Physical Research Laboratory, Ahmedabad.

3 Calculated electron density due to impact of hard X-rays in D region ionosphere of Mars: First model result

Siddhi Y. Shah, S. A. Haider

Date: 29-31 January, 2019

Organizer: 20th National Space Science Symposium to be held at Savitribai Phule Pune University, Pune.

List of Publications

Haider, S. A., Batista, I. S., Abdu, M. A., Muralikrishna, P., **Shah, S. Y**., and Kuroda, T (2015), Dust storm and electron density in the equatorial D region ionosphere of Mars: Comparison with Earth's ionosphere from rocket measurements in Brazil. J. Geophys. Res., **120**, 8968-8977.

Haider, S. A., Batista, I. S., Abdu, M. A., Santos, A. M., **Shah, S. Y**, et al. (2016), Flare X-ray photochemistry of the E region ionosphere of Mars. J. Geophys. Res., Space Physics, **121**, 6870-6888.

Siddhi Y. S, Haider,S.A., Molina-Cuberos, G. J,Abdu, M.A., Batista, I (2019), A coupled model of the D and E regions of Mars' ionosphere for flare and non-flare electron density profiles: Comparison with Earth's ionosphere, Icarus. (Under review).

Haider, S. A., **Siddhi Y. S**, Masoom, J., Sheel, V., and Kuroda, T (2019), Dust loading on ozone, winds and heating rates in the tropics of southern atmosphere of Mars: Seasonal variability, climatology and SPICAM observations. Q J R MeteorolSoc, (Under review).